MILLIMETER-WAVELENGTH REMOTE SENSING OF THE ATMOSPHERIC STRUCTURE AND COMPOSITION OF VENUS

A Dissertation
Presented to
The Academic Faculty

By

Alex B. Akins

In Partial Fulfillment
of the Requirements for the Degree
Doctor of Philosophy in the
School of School of Electrical and Computer Engineering

Georgia Institute of Technology

May 2020

MILLIMETER-WAVELENGTH REMOTE SENSING OF THE ATMOSPHERIC STRUCTURE AND COMPOSITION OF VENUS

Approved by:

Dr. Paul Steffes, Advisor
School of Electrical and Computer Engineering
Georgia Institute of Technology

Dr. Morris Cohen
School of Electrical and Computer Engineering
Georgia Institute of Technology

Dr. Gregory Durgin
School of Electrical and Computer Engineering
Georgia Institute of Technology

Dr. Waymond Scott
School of Electrical and Computer Engineering
Georgia Institute of Technology

Dr. Britney Schmidt
School of Earth and Atmospheric Sciences
Georgia Institute of Technology

Date Approved: March 23, 2020

"Before I had studied, I saw mountains as mountains, and rivers as rivers. When I arrived at a more intimate knowledge, I saw that mountains are not mountains, and rivers are not rivers. But now that I have got its very substance, I am at rest. I see mountains once again as mountains, and rivers once again as rivers."

-attributed to Qingyuan Weixin

To my parents,

for their limitless love and support.

ACKNOWLEDGEMENTS

I'd like to first acknowledge Dr. Paul Steffes for providing an excellent topic for this dissertation and for the guidance, patience, and support throughout the process of its completion. He has been an excellent mentor with relentless optimism that was highly motivating during periods of uncertainty and unexpected setbacks. I'd also like to thank the members of my committee, Drs. Cohen, Durgin, Scott, and Schmidt for their time and attention in reviewing this work. This dissertation also relies heavily on the methods and techniques developed by prior members of the Georgia Tech Planetary Atmospheres lab over the years, particularly Marc Kolodner, Jim Hoffman, Tom Hanley, Kiruthika Devaraj, and Amadeo Bellotti. I'd also like to thank those who were involved in the fabrication of the resonator system described in this dissertation. The staff of the Montgomery Machining Mall, specifically Louis Boulanger, Nate Maudlin, and Scott Elliot, went above and beyond in their capacity as machinists, and they were invaluable instructors in the use of the machine shop equipment. Doug and Gia from the Estes-Simmons Plating Company and Nick from Revel-Capewell deserve thanks for ensuring that the quality of gold-plating on the resonator mirrors was sufficient for use in a corrosive environment. I owe many thanks to the members of the Van Leer building fifth floor community, particularly Josh Mendez-Harper, Amoree Hodges, Parker Singletary, Marc Higginson-Rollins, Nate Opalinski, Ted Slevin, Mohammed Alhassoun, and Jackson McCormick for their friendship inside and outside of the lab. During my 8 years as a member of the Georgia Tech community, I've crossed paths with many people who have affected my life in some way. Although I dare not attempt to list everyone here, thank you all. Finally, I'd like to thank my family. My mother and father have been the most supportive parents and role models in every aspect of my life, and I am truly grateful to be their son. I am also forever grateful for my wife Michaela, who has supported me through every moment of frustration and triumph. I couldn't ask for a better partner, and I'm excited to start the next chapter in our lives together.

TABLE OF CONTENTS

LIST OF TABLES

xvii

SUMMARY

Microwave and millimeter-wavelength radiometric observations and radio occultations are capable of providing insight into the structure and bulk composition of the Venus atmosphere within and below layers of clouds which cover the entire planet. To interpret such observations, accurate models for the absorption of the atmospheric constituents of Venus are necessary. The objective of this research has been to further understanding of the millimeter-wavelength spectrum of Venus. To this end, over 400 laboratory measurements have been made of the opacity of H_2SO_4 vapor in mixtures containing up to 3 bars of CO_2 at temperatures ranging from 535-585 K, simulating the conditions of the lower atmosphere of Venus. The results of these measurements and prior laboratory studies have been combined to derive a model for H_2SO_4 vapor opacity valid at frequencies below 150 GHz. This model is incorporated into a microwave radiative transfer model of the Venus atmosphere, which has been used to predict the penetration depth of a radio occultation signal. Low-noise images of Venus have also been developed from observations made using the CARMA and ALMA radio telescopes and compared against the emission spectrum produced by the model.

CHAPTER 1

INTRODUCTION

1.1 Background

Of the terrestrial planets in our solar system, Venus is the most similar to Earth at first glance. Table 1.1 gives a comparison of physical and orbital characteristics of both the Earth and Venus.

Table 1.1: Physical and orbital parameters for the Earth and Venus [1]

	Earth	Venus
Mean Solar Distance (AU)	1.0	0.7233
Orbital Period (days)	365.256	224.701
Eccentricity	0.0167	0.0067
Ellipticity	0.0034	0.0000
Inclination to Ecliptic (degrees)	0	3.39
Mass (kg)	5.976×10^{24}	4.871×10^{24}
Mean Radius (km)	6378	6051.3

For early observers, these physical similarities created an optimism that Venus may be inhabited by lifeforms not unlike from those found on Earth. Ground-based observations, however, revealed a planet with a surface and atmosphere far more alien than was previously imagined [1]. While infrared emission measurements suggested Earth-like temperatures, passive microwave measurements revealed a surface temperature in excess of 700 K. Further spectroscopic and polarimetric observations revealed a 96% CO_2 atmosphere with rich sulfur chemistry and a global cloud layer consisting predominately of concentrated H_2SO_4 aerosols. Estimations of the planet's rotational characteristics through observation of ultraviolet cloud features were overturned by Arecibo radar measurements, which suggested that the rotation period of Venus was far slower than that of Earth. These insights made Venus an important target for early satellite missions by both the United States and

the Soviet Union. On orbit and in situ observations by Pioneer Venus and the Venera missions provided a wealth of information about Venus, including characterization of the magnetic field (or lack thereof), observations of a high D/H ratio (through H_2O and HDO), investigation of persistent ultraviolet features at the cloud level, study of the above cloud super-rotating winds, and the first radar images and direct measurements of the surface of the planet [1]. Further observations by Magellan in 1989 provided high resolution radar mapping of geological features [2]. Satellite exploration of Venus resumed in 2006 with the arrival of the ESA Venus Express mission, and has continued with the still-active JAXA Akatsuki Orbiter [3, 4]. The development and execution of subsequent mission concepts will be crucial to form a more complete picture of Venus, which in turn will benefit our understanding of the origin and evolution of the solar system.

The priorities for Venus exploration are captured in the Planetary Science Decadal Survey and the guiding documents for the Venus Exploration and Analysis Group (VEXAG) [5, 6]. The Decadal Survey establishes three goals for terrestrial planet exploration: Understanding the origin and diversity of terrestrial planets, understanding how the evolution of terrestrial planets enables and limits the origin and evolution of life, and understanding the processes that control climate on Earth-like planets. The VEXAG community has established goals for Venus exploration within this framework: Understanding atmospheric formation, evolution, and climate history on Venus, and understanding the nature of interior-surface-atmosphere interactions over time, including whether liquid water was ever present. To these ends, several missions have been proposed to return to Venus. Of interest at the time of writing are the ESA M5-class Envision mission proposal, the joint NASA-Roscosmos Venera-D mission concept, and several NASA Discovery Class proposals. The work presented in this dissertation has applications to the radio science experiments for these and other future missions to Venus.

Within the VEXAG goals, there are several open questions regarding the structure, composition, and dynamics of the Venus atmosphere at all levels. Since many of these goals

relate to the evolution of Venus over time, they can only be addressed via sophisticated models of atmospheric circulation and chemistry. Measurements of the current state of the Venus atmosphere, therefore, are important to distinguish between realistic and unrealistic model scenarios. If Venus lost an ocean's worth of water, what would its atmosphere look like today, and can we build a physically consistent model of water loss that arrives at the current conditions? These and other questions drive the urgency of in situ and remote sensing of atmospheric properties. Of particular interest is the importance of the atmospheric conditions near the lower cloud. Contemporary thermochemical and photochemical models of Venus atmospheric chemistry assume an upper and lower boundary region near the lower cloud region [7, 8, 9]. Recent attempts to develop chemical models for the entire atmosphere are highly dependent on the starting state of the atmosphere near the lower cloud [10]. Within this region, the thermal structure transitions from strong to weak static stability with confined convective regions, the abundance of SO_2 (the fourth most abundant gas at Venus) changes by an order of magnitude, the lower cloud aerosols vaporize to form sulfuric acid vapor, and significant vertical winds have been observed [11]. Study of the atmosphere within and below the clouds and how it varies over latitude and time can provide important constraints to chemical models which allow us to understand the origins and evolution of Venus.

1.2 Microwave Remote Sensing of the Venus Atmosphere

At centimeter and millimeter-wavelengths, the atmosphere of Venus has been largely studied using two techniques: passive radiometry and the radio occultation. Microwave radiometric studies of Venus have taken place both from the ground and from space. A history of early ground-based observations of the disk-averaged microwave emission from Venus prior to spacecraft exploration is given by Barrett and Staelin [12]. Mariner 2 was the first spacecraft sent to Venus to measure the microwave emission from Venus at multiple angles. Pollack and Sagan concluded that the observed emission at 13.5 mm and 19 mm could not

3

be explained by CO_2-N_2 and water vapor opacity alone, implying that an additional microwave absorber must be present [13].

Subsequent missions to Venus have employed the radio occultation technique, measuring the attenuation of a coherent downlink signal from the satellite to measure the atmospheric temperature, pressure and density profiles down to the critical refraction altitude near 33 kilometers above the mean surface [14]. Results from the Mariner 5 and Mariner 10 radio occultation experiments, in addition to the cloud composition results from the Pioneer-Venus cloud particle-size spectrometer, led Steffes and Eshleman to test the idea that the additional source of microwave opacity detected was H_2SO_4 vapor forming below the lower cloud [15]. Following a series of laboratory measurements, Steffes and Eshleman confirmed that H_2SO_4 vapor and gaseous SO_2 were the trace species that greatly affected microwave absorption at Venus [16, 17]. Since this confirmation, the radio occultation experiment for the Magellan mission measured H_2SO_4 vapor profiles at higher latitudes [14, 18], and Venus Express has carried out over 600 radio occultations, resulting in nearly complete latitudinal coverage and observations of the variation of H_2SO_4 vapor abundance over time [19]. Resolution of the retrieved temperature and pressure profiles from the Venus Express and Akatuski radio occultation experiments has also been improved via the use of the Full Spectrum Inversion technique [20].

The development of sensitive ground-based radio interferometers enabled the first spatially-resolved measurements of microwave and millimeter-wavelength emission from Venus [21]. More recent microwave observations of lower atmosphere and surface have been made using the Very Large Array (VLA) and the Giant Metrewave Radio Telescope (GMRT) [22, 23, 24, 25]. The VLA observations yielded low noise maps of the Venus disk emission with spatial brightness temperature variations that could be predicted based on emission angle and latitude-dependent thermal structure, and retrievals of temperature and H_2SO_4 vapor abundances were reported. Prior to 2010, 3 millimeter-wavelength observations were carried out using the Hat Creek Interferometer and the Nobeyama Millimeter Ar-

ray [26, 27]. These observations showed day to night variations in brightness temperature ranging 30-80 K, which cannot be ascribed to variations in the thermal structure alone. If these observed variations are not the result of noise in the observations, a physical explanation would require significant variations in the composition of the cloud-level atmosphere. In addition to the observations of thermal continuum emission, many observers in recent years have studied lines in the rotational spectra of molecules in the Venus atmosphere to determine the composition and wind speeds in the mesosphere [28, 29, 30, 31, 32, 33, 34, 35].

Interpretation of the results of both radio occultation and passive radiometric observations require models of the absorptivity of the gases present in the Venus atmosphere. The significant microwave absorbers in the Venus atmosphere are the bulk CO_2/N_2 atmosphere, H_2SO_4 vapor, SO_2, and H_2SO_4 aerosols. The microwave absorptivity of CO_2 and N_2 was measured under Venus conditions by Ho, Kaufman, and Thaddeus and Steffes et al. [36, 37]. The early results of Steffes and Eshleman [38, 15, 17] have been improved upon at microwave frequencies for both SO_2 [39, 40, 37] and H_2SO_4 vapor [41]. Additionally, Fahd and Steffes conducted laboratory measurements of the millimeter-wavelength opacity of liquid H_2SO_4 [42]. More recently, the measurements of SO_2 absorptivity have been extended higher in frequency, temperature, and pressure, which has confirmed the validity of the Fahd and Steffes model [43, 37]. Measurements have also been made of the opacity of HCl under Venus conditions [44]. Prior to this work, there exists no published model for the opacity of H_2SO_4 vapor at frequencies greater than 22 GHz.

1.3 Motivation

The objective of this research has been to further the understanding of the millimeter-wavelength spectrum of the Venus atmosphere. This has been accomplished through measurement of the 2-4 millimeter (W and F Band) and 7-10 millimeter (K_a Band) absorptivity of H_2SO_4 vapor in the laboratory under temperature and pressure conditions rele-

5

vant to the Venus atmosphere. Using these measurements and the centimeter-wavelength measurements of Kolodner and Steffes [41], a model for absorptivity has been developed that is valid over wavelengths from 30 centimeters to 2 millimeters. To leverage these results, a radiative transfer model of the Venus atmosphere has been developed incorporating atmospheric and surface parameters derived from spacecraft measurements and chemical models. Additionally, spatially-resolved 2-3 millimeter brightness temperature maps have been developed from recent observations using the Combined Array for Research in Millimeter-wave Astronomy (CARMA) and the Atacama Large Millimeter/submillimeter Array (ALMA) and compared to the radiative transfer model results. The radiative transfer model has also been used to study how the absorption associated with the Venus atmosphere will affect K_a (32 GHz) Band radio occultation experiments proposed for future Venus missions, which will inform planning for these missions.

1.4   Organization

This dissertation will discuss the topics mentioned in the prior section in order. Chapter 2 describes the laboratory measurements at W, F, and K_a Band, detailing the measurement theory, the design and fabrication of the microwave open resonators used for this work, and measurement uncertainty analysis. This section also discusses the hardware used to transmit and receive millimeter-wavelength signals and the pressure vessel and temperature chamber used to achieve the necessary conditions. Chapter 3 describes the results of the measurements, gives background information on the calculation of absorptivity from spectral line catalogs, and describes the development of the model for H_2SO_4 vapor absorptivity. Chapter 4 details a radiative transfer model of the Venus atmosphere, including discussion of the model inputs and description of analytical and iterative ray-tracing procedures for a refractive, spherically symmetric atmosphere. This radiative transfer model is then used to generate a brightness temperature spectrum of Venus, which is compared to prior observations, and to predict the attenuation that will be experienced for future K_a

Band radio occultations of the Venus atmosphere. Chapter 5 describes the CARMA and ALMA observations, details the procedure used to generate images from the data, presents the final derived images, and compares the results to radiative transfer model predictions. Finally, Chapter 6 provides conclusions and suggestions for future work.

<div align="center">

CHAPTER 2

LABORATORY MEASUREMENTS OF SULFURIC ACID VAPOR

ABSORPTIVITY AT W, F, AND K$_A$ BAND

</div>

Accurate determination of the millimeter-wavelength absorptivity of atmospheric gases requires the construction of sensitive measurement systems. For the measurement of H_2SO_4 vapor under Venus conditions, careful design and accurate characterization of the measurement system is particularly important. This chapter describes the measurement theory and design methodology employed to enable millimeter-wavelength measurements of H_2SO_4 vapor absorptivity in the W, F, and K$_a$ Bands. Also included are descriptions of the temperature and pressure systems, hardware specifications, description of the measurement procedure, and analysis of uncertainty in the measurement process.

2.1   Measurement Theory

The amplitude and phase of the constituent electric and magnetic field components of a monochromatic electromagnetic wave traveling in a homogeneous medium away from its source in the +z direction can be expressed in the phasor form of Equations 2.1 and 2.2 with units of V/m and A/m respectively. For subsequent discussion, the time-varying portion of the phasor will be excluded.

$$E = E_o e^{-jkz} e^{j\omega t} \tag{2.1}$$

$$H = H_o e^{-jkz} e^{j\omega t} \tag{2.2}$$

The spatial wavenumber in m^{-1} can be expressed with a variety of useful equivalencies

(Equation 2.3).

$$k = \frac{2\pi}{\lambda} = \frac{\omega}{c} = \omega\sqrt{\mu\epsilon} \tag{2.3}$$

From the final relation, it is evident that the propagation characteristics of the electromagnetic wave are related to the dielectric properties of the medium through which it travels. For gas mixtures, the magnetic permeability μ can be considered equivalent to the free space permeability of $4\pi \times 10^{-7}$ H/m. The permittivity ϵ, however, is complex (Equation 2.4).

$$\epsilon = \epsilon' - j\epsilon'' \tag{2.4}$$

The complex nature of the permittivity expression leads to attenuation and phase shift of this signal in the medium. Equations 2.5 - 2.7 give the relationship between the complex permittivity and the attenuation and phase constants, respectively [45].

$$jk = \alpha + j\beta = j\omega\sqrt{\mu\epsilon'\left[1 - j\frac{\epsilon''}{\epsilon'}\right]} \tag{2.5}$$

$$\alpha = \omega\sqrt{\left(\frac{\mu\epsilon'}{2}\right)\left[\sqrt{1 + \left(\frac{\epsilon''}{\epsilon'}\right)^2} - 1\right]} \tag{2.6}$$

$$\beta = \omega\sqrt{\left(\frac{\mu\epsilon'}{2}\right)\left[\sqrt{1 + \left(\frac{\epsilon''}{\epsilon'}\right)^2} + 1\right]} \tag{2.7}$$

The ratio of the complex permittivity components gives the loss tangent of the gas, also known as the dissipation factor, which is the inverse of the quality factor of said gas.

$$\frac{\epsilon''}{\epsilon'} = \tan\delta = \frac{1}{Q_{\text{gas}}} \tag{2.8}$$

Calculation of the frequency-dependent attenuation constant can be simplified due to

the relatively low value of the loss tangent associated with the gases. Since the loss tangent, and thereby the ratio of the complex permittivity components, is low, the quantity $\sqrt{1 + \left(\frac{\epsilon''}{\epsilon'}\right)^2}$ can be replaced by the first two terms of its Maclaurin series, yielding $1 + \left(\frac{\epsilon''}{\epsilon'}\right)^2 / 2$. By implementing this replacement, the simplified expression for the attenuation in nepers per meter given in Equation 2.9 results. The assumption of small loss tangent is known as the imperfect dielectric assumption [46].

$$\alpha \approx \frac{k\epsilon''}{2\epsilon'} = \frac{\pi}{\lambda}\frac{\epsilon''}{\epsilon'} = \frac{\pi}{\lambda}\frac{1}{Q_{gas}} \tag{2.9}$$

The quality factor of a resonant system is a relationship between the stored energy U and the average power loss W_L as energy traverses the path of the system [47]. It can also be expressed as a relationship between the frequency f of maximum power transmission and the -3 dB bandwidth Δf of this transmission. The final equivalency shown in Equation 2.10 gives the effective path length l_p of electromagnetic energy within the resonator [48].

$$Q = \frac{\omega U}{W_L} = \frac{f}{\Delta f} = \frac{2\pi l_p}{\lambda} \tag{2.10}$$

By measuring the quality factor of a gas, the attenuation constant can be determined for a frequency of interest. Cavity resonators are excellent tools for differential measurement of gas quality factor in the microwave region. With careful design, resonant cavities can support frequency-selective, high-Q standing wave resonances between conducting boundaries. The power loss in the cavity resonator system is a function of the dimensions of the cavity and the resistive losses due to reflections from imperfectly conducting boundaries. Proper design results in resonances with quality factors ranging from the thousands to hundreds of thousands. By introducing a lossy test gas mixture into a resonant system, the Q of the pre-existing resonances will be reduced. Measurement of this reduction gives a precise value for the quality factor of the gas, and through the imperfect dielectric assumption, a value for the attenuation constant. Closed cavity resonators are best utilized for measure-

ment of absorption in the centimeter wavelength range. By removing the conductive walls of a closed resonator system, resonances at higher order modes are suppressed. The resulting open resonator is the design of choice for absorption measurements at millimeter wavelengths.

When energy enters a resonant system loaded with a gas mixture, frequency-selective standing wave resonances result, each with its own quality factor. The quality factor of any one of the resonant frequencies can be expressed using the relationship in Equation 2.11.

$$\frac{1}{Q_{\text{loaded}}} = \frac{1}{Q_{\text{gas}}} + \frac{1}{Q_r} + \frac{1}{Q_{\text{ext,1}}} + \frac{1}{Q_{\text{ext,2}}} \tag{2.11}$$

The quality factor of the gas, Q_{gas} is the desired result of the measurement. The quality factor Q_r is the quality factor of the unloaded resonator, and Q_{ext} is the quality factor associated with the additional path losses due to resonator coupling and energy transmission. Since there are two separate transmission paths and coupling apertures for open resonator systems, there are two external quality factors, which are generally considered to be symmetric. These contributions to the **Q** can be isolated through a vacuum measurement of the quality factor.

$$\frac{1}{Q_{\text{vac}}} = \frac{1}{Q_r} + \frac{1}{Q_{\text{ext,1}}} + \frac{1}{Q_{\text{ext,2}}} \tag{2.12}$$

Due to the complex nature of the losses that contribute to Q_{ext}, the external quality factor can only be expressed in relationship to the measured **Q** of the resonator through the transmissivity, t. The resonance-dependent transmissivity is a measurement of the insertion loss S of the resonator in decibels, and can be expressed as a ratio of the measured quality factor Q_m and the external loss quality factor Q_{ext} [47].

$$t = 10^{-S/10} = \left(2\frac{Q_m}{Q_{\text{ext}}}\right)^2 \tag{2.13}$$

Measurement of the resonator transmissivity, the quality factor of the resonances under

vacuum conditions, and the quality factor under gas-loaded conditions provides enough information to solve for the gas quality factor, and hence absorption. The resulting equation for the quality factor of the gas is given in Equation 2.14.

$$\frac{1}{Q_{gas}} = \frac{1 - \sqrt{t_{loaded}}}{Q_{loaded}} - \frac{1 - \sqrt{t_{vac}}}{Q_{vac}} \tag{2.14}$$

Equation 2.14, however, is not the final expression for the quality factor of the gas that should be used to obtain the most accurate determination of the absorption. When the resonator system is loaded with a test gas such as H_2SO_4, a refractive shift in the center frequency of the resonance occurs. Equation 2.15 gives the relationship between the gas-loaded shift in the center frequency of the resonance and the refractivity, N, of the gas. The relationship between refractive index n_r and refractivity is included below as well.

$$N = 10^6 * \frac{f_{vac} - f_{gas}}{f_{gas}} \tag{2.15}$$

$$N = 10^6 * (n_r - 1)$$

A convenient measure of the refractivity of gas is the number-density normalized refractivity in units of (cm^3/molecule). For mixtures of gases, the normalized refractivity can be obtained by accounting for the density of the gas within the mixture, and this relationship is given in Equation 2.16 where T is the temperature in Kelvins, R is the ideal gas constant, and P is the partial pressure of the gas in the mixture.

$$N' = \frac{NRT}{P} \tag{2.16}$$

Due to the nonlinear relationship between the resonator and external quality factors, variations in the measured quality factor of the gas-loaded resonator could actually be due to this refractive shift. This variation effect is known as dielectric loading, although true

dielectric loading would refer only to energy loss caused by the gas loading while excluding the effects of the frequency shift on the external quality factor [49]. For this discussion, dielectric loading will be used in reference to all shift-related resonator quality factor effects. There are a few ways to deal with this problem, depending on the design of the resonant system. The semi-confocal resonator design of Valkenburg and Derr provides one example of mechanical correction [48]. One of the mirrors used is connected to a threaded rod, allowing for the separation of the mirrors to be changed. To correct for the refractive shift, the mechanical position of the mirror is varied until the frequency of the resonance measured matches that of the shifted resonance under gas loading. Another way to adjust for dielectric loading, and the method employed for the measurements described here, is dielectric matching with a transparent gas. A refractive gas can be added to the resonator system to shift the resonances to match the gas-loaded shift. Thus, equation 2.14 can be modified to include measurements from the dielectrically matched conditions to give the final expression for the measured quality factor of the gas.

$$\frac{1}{Q_{gas}} = \frac{1 - \sqrt{t_{loaded}}}{Q_{loaded}} - \frac{1 - \sqrt{t_{matched}}}{Q_{matched}} \qquad (2.17)$$

2.2 Open Resonator Design

Frequency selective resonances at millimeter wavelengths can formed by coupling electromagnetic energy into a system of two precisely aligned conducting plates. This open resonator structure behaves as the microwave analogue of the optical Fabry-Perot interferometer. While earlier designs made use of parallel grating reflectors [50], researchers found that they could lower diffraction losses by using concave conductor plates, or mirrors, that focused the resonant energy along the axis of alignment [51]. Clarke and Rosenberg provide a survey of open resonators, including discussion of different designs and the governing equations [52]. The sensitivity of an open resonator increases with a higher resonance quality factor. The quality factor can be defined in the terms of Equation 2.10, but for open

Physical Semi-confocal Configuration

Equivalent Confocal Configuration
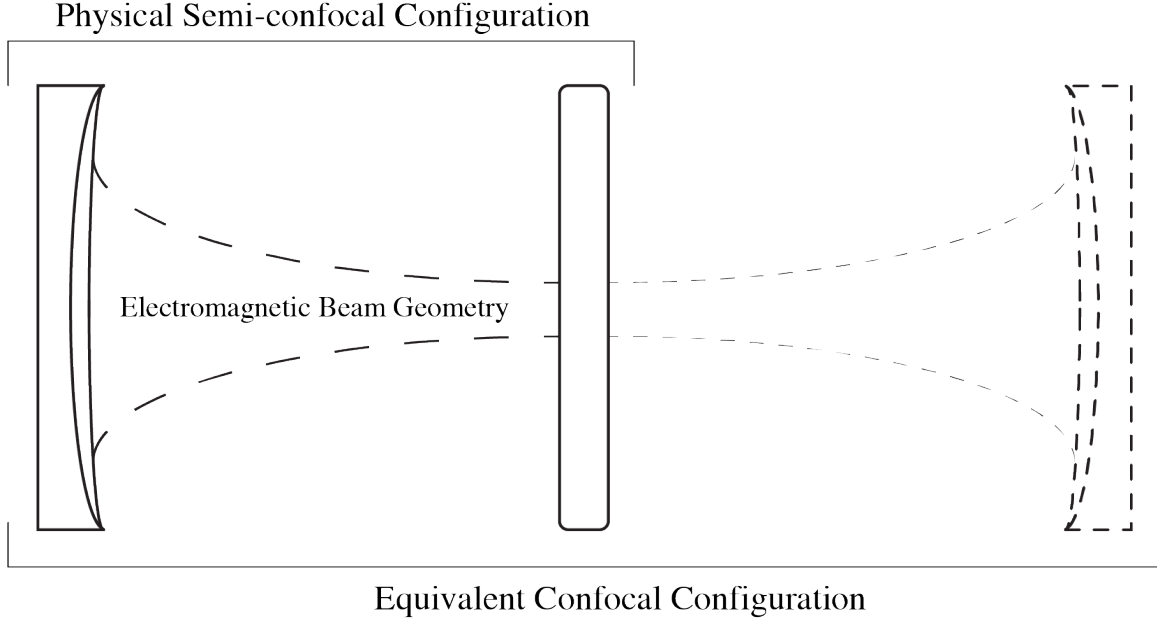
Figure 2.1: A semi-confocal resonator geometry as an analogue for a confocal arrangement

resonators, another relationship exists between the quality factor and the wavenumber k, the mirror spacing D, and the mirror reflectivity R.

$$Q = kD \frac{\sqrt{R}}{1 - R} \qquad (2.18)$$

Confocal open resonators consisting of identical concave mirrors separated by a distance close to their radius of curvature can yield the highest Q measurements both in theory and in the laboratory application [51, 53]. Semi-confocal systems, consisting of a curved mirror and a flat mirror, can also be used to achieve high Q with lower sensitivity to mirror misalignment. As seen in Figure 2.1, a semi-confocal configuration can emulate a fully confocal alignment with a mirror separation of only half the radius of curvature of the curved mirror.

Semi-confocal open resonators have been employed frequently for microwave opacity measurements of gases [48, 54, 55, 56, 57]. Microwave energy extinction is measured by monitoring variations in the Q of the standing wave resonances.

To increase the conductivity of the mirror surfaces used in this experiment, both mirrors

are plated with a thin layer of nickel, gold flashed, and polished. The depth of penetration, or δ_p for gold is given as a function of the frequency f of the incident wave, the conductivity σ, and the permeability μ of gold.

$$\delta_p = \frac{1}{\sqrt{\pi f \mu \sigma}} \tag{2.19}$$

For an incident electromagnetic wave with a frequency of 75 GHz, the skin depth of gold is approximately 287 nm. Since the gold plating is substantially thicker than the skin depth, the incident wave can be treated as if it reflects from a pure gold surface. Despite the high conductivity of gold and the polishing of the mirror surfaces, resistive losses will result at each reflective boundary. Energy loss can also occur via diffraction near the edges of the mirrors. Increasing the diameter, and subsequently the Fresnel number N_F, of the mirrors reduces diffraction loss [58]. For a semi-confocal system, changing the diffractive loss of the system via the diameter of the flat mirror can be used as a form of mode selection, since higher order modes will be suppressed while retaining the TEM_{00q} modes [48]. The Fresnel number N_F of the resonator system can be calculated using the diameter of the mirrors a, the mirror spacing b, and the wavelength λ.

$$N_F = \frac{a^2}{b\lambda} \tag{2.20}$$

Losses can also result from misalignment of the resonator mirrors. To ensure a high Q, the axial displacement of the curved mirror is adjusted using a stainless steel threaded rod. Fine angular adjustments of the flat mirror and curved mirror can be made with a series of stainless steel tuning screws.

The semi-confocal open resonator design used for H_2SO_4 vapor opacity measurements is shown in Figure 2.2 within a pressure vessel housing, and the constructed assembly is shown in Figure 2.3. A stainless steel spherical mirror with a diameter of 3.5 inches and a radius of curvature of 40 centimeters is positioned 20 centimeters from the center axis
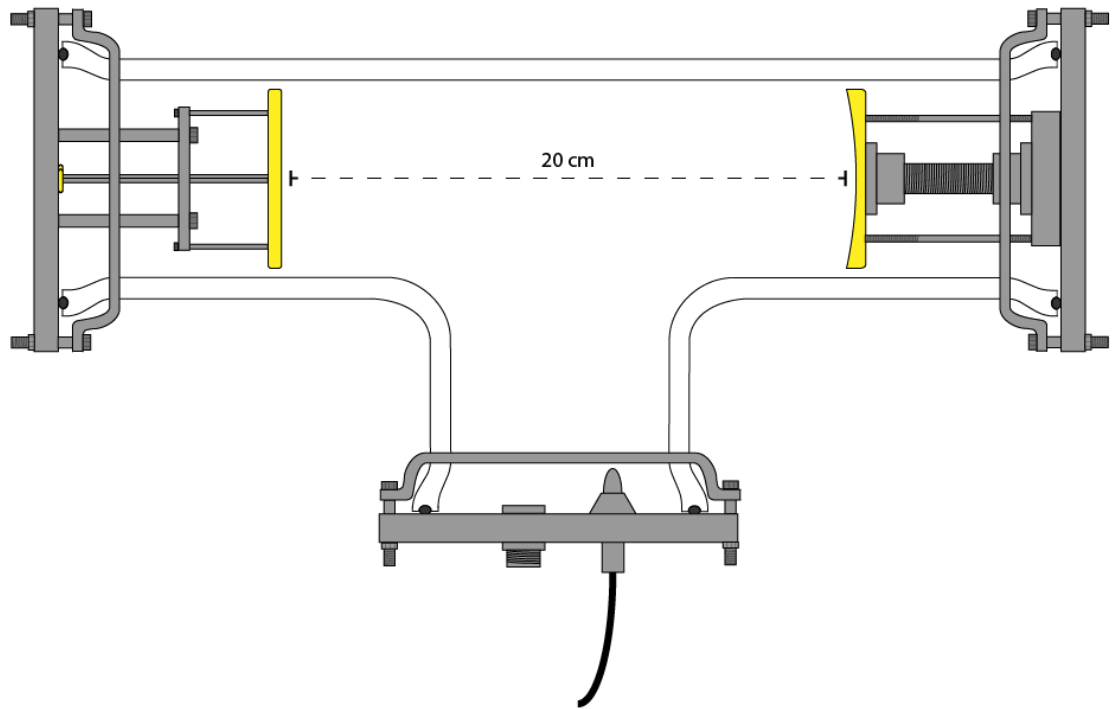
Figure 2.2: Design of the semi-confocal resonator used for millimeter wavelength measurements

of a stainless steel flat mirror. Co-polarized electromagnetic energy is coupled into and out of the resonator through two iris apertures in the flat mirror offset uniformly from the center. Coupling losses result from these irises, and the iris size must be chosen carefully. Small irises reduce overall power transmission from the feeding waveguide and reduces the amount of energy that can transfer out of the system into the receiver. Conversely, large irises cause significant distortions in the reflective surface of the flat mirror, further reducing the quality factor of the resonator. Moran investigated this iris problem for a confocal resonator system, finding that sensitivity to the iris size increases with Fresnel number [59]. Additionally, the thickness of the iris apertures can be treated as a circular waveguide operating below the cutoff frequency [60]. However, the thickness of the apertures used in the described semi-confocal system result in a negligible amount of attenuation. The specifications for the flat mirror vary for each measurement band, and details are given in Section 2.5

16
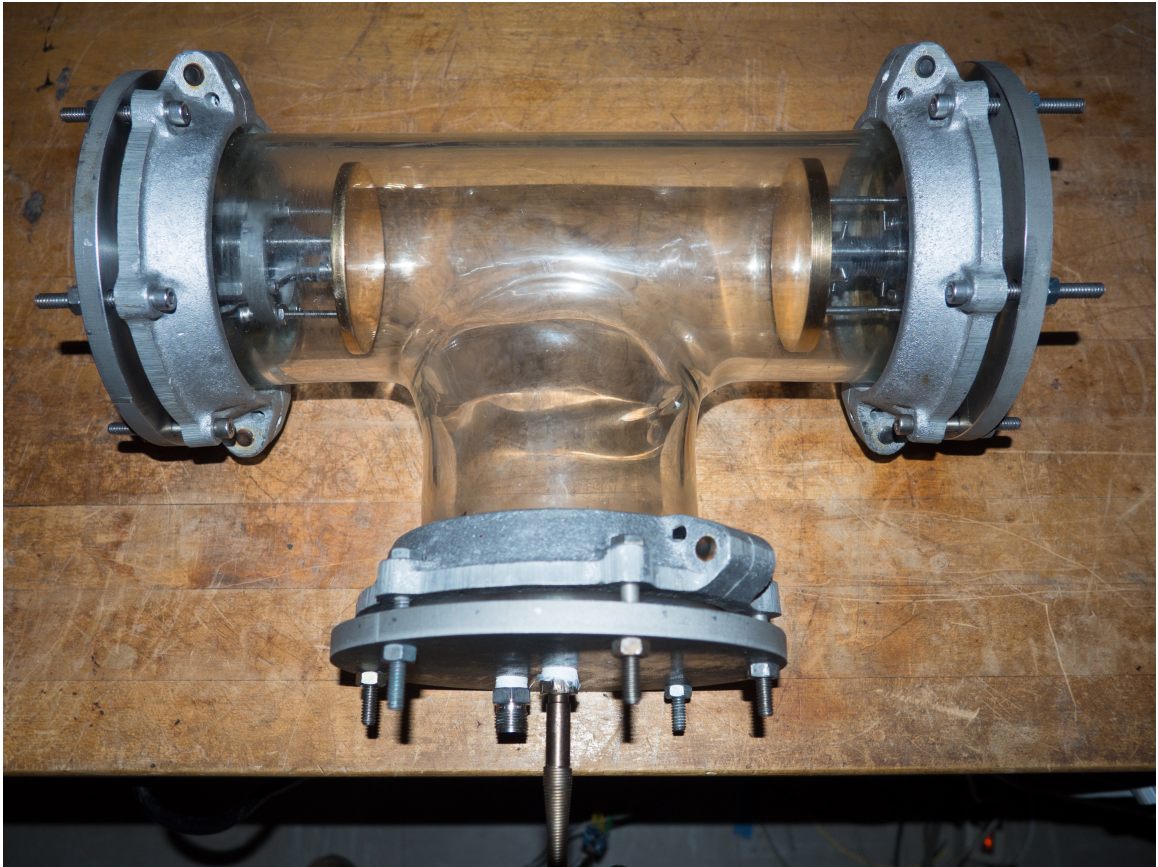
Figure 2.3: W and F Band semi-confocal resonator assembled and housed within the pressure vessel

2.3 Temperature and Pressure Systems

A T-shaped pressure vessel made of borosilicate glass is used to house the H_2SO_4/CO_2 gas mixture and the resonator mirrors. All hardware components inside of the pressure vessel are made of materials that resist corrosion. While waveguide flanges feeding the flat mirror are made from brass, the exterior of the flange is gold-plated to minimize corrosive effects. In addition to corrosion resistance, all materials must have a useful operating temperature for the duration of an experiment which is above the maximum measurement temperature. The endplates of the pressure vessel are machined from stainless steel, and seals are established using perfluoroelastomer Viton O-rings. The O-rings and the end of the glass chamber are coated in Krytox LVP vacuum grease to facilitate a seal. The gas mixture enters the pressure vessel through a threaded insert in one of the stainless steel endplates, and the temperature within the vessel is monitored using a Type T thermocouple connected to an Omega HH91 thermocouple thermometer. The pressure vessel is housed in an insulated temperature chamber, shown in Figure 2.4. A borosilicate glass H_2SO_4 reservoir remains in this temperature chamber during the measurement process, and is connected to the pressure vessel via 3/8 inch diameter stainless steel piping fastened with Swagelok fittings and wrapped with PTFE thread-sealing tape. This piping configuration also connects the pressure vessel to an Airgas carbon dioxide tank, a Welch DuoSeal vacuum pump, and an exhaust vent, each with its own controlling valve (valves within the temperature chamber are rated for higher temperatures). An Omega DPG700 vacuum and pressure gauge is connected to the piping to monitor the integrity of the pressure seal during operation. Metal waveguides are used to transmit energy in and out of the resonator system. As a result of the high thermal conductivity of the waveguides, heat may transfer quickly to the electronics. Due to the operating temperature limits of the microwave electronics for W and F Band, the WR-10 copper waveguides are partially immersed in a cooling chamber. Metal contacts within the cooling chamber result in an effective heat sink. For the K_a Band

18

system, the mixing electronics are insulated via a long flexible WR-28 waveguide.

The volume of the pressure vessel assembly was determined empirically using a tank of nitrogen gas and an MKS Instruments Type 1159B Mass Flow Controller (controlled electronically). The assembled pressure vessel is connected via 3/8 inch diameter stainless steel Swagelok piping to a Druck DPI 104 pressure gauge and the mass flow controller, which is connected to the nitrogen tank. The pressure chamber is initially maintained at ambient temperature, and the initial pressure is recorded. The mass flow controller valve is then opened to allow gas to flow at a nominal rate of 20 standard cubic centimeters per minute. This unit system allows for accurate determination of the number of moles of gas passing through the system over time. The rate of gas flow is recorded by the mass flow controller as a function of seconds elapsed since the valve has been opened. When the pressure measured by the pressure gauge approaches 1 bar above ambient pressure, the valve is closed, and the final pressure is recorded. The gas within the pressure chamber is vented down to ambient pressure, and the same process is repeated four more times. Using the difference between the starting and final pressures in the chamber, the integrated volume of gas added to the chamber at standard temperature and pressure, and the ideal gas law, the volume of the pressure vessel is determined to be 3.5098 L $\pm$ 0.0069. This value reflects only the volume of the pressure vessel, since the volume of the piping connecting the vessel to the mass flow controller was determined using the same method and subtracted to yield the proper result. Note also that the volume of piping exposed to the pressure vessel during experiments was determined to be 40.17 mL using physical measurements and CAD files procured from Swagelok for all valves and joints.

2.4 Transmission Lines

As a signal travels towards the semi-confocal resonator system, it incurs losses in the waveguides. Knowledge of the losses in the waveguides is important in order to accurately determine the transmission loss attributable to the gas mixtures under test. This waveguide

Figure 2.4: Pressure vessel and piping within the temperature chamber

loss must be subtracted from the total measured loss so as to determine the remaining loss due to the gases. Since the waveguides are not filled with a material that could incur substantial dielectric losses, the primary loss through the waveguides occurs at the conducting walls. Equations 2.21 and 2.22 gives the attenuation in decibels per meter as a function of frequency f for a conducting waveguide [61]. The long and short dimensions of the waveguide are given by a and b, respectively.

$$\alpha = 8.686 \frac{R_s}{\eta} \frac{1}{b} \frac{1 + \frac{2b}{a}\left(\frac{f_c}{f}\right)^2}{\sqrt{1 - \left(\frac{f_c}{f}\right)^2}} \quad dB/m \tag{2.21}$$

$$\frac{R_s}{\eta} = \sqrt{\frac{\omega \epsilon_0}{2\sigma}} \tag{2.22}$$

The sheet resistance term R_s/η is a function of the inverse of the resistivity of the waveguide walls, which varies with temperature. Empirical expressions for the change in electrical resistivity with temperature for copper and stainless steel are employed to determine the theoretical loss experienced in the waveguides.

2.4.1 Stainless Steel Waveguides

Hust and Lankford give a polynomial expression for the electrical resistivity of stainless steel in the form of Matthiessen's Rule, which is reproduced in Equation 2.23 [62]. The residual resistivity ρ_0 is the resistivity of the material at close to 0 K, and ρ_c accounts for residuals in the measured data used to form this expression. The appropriate coefficients employed for stainless steel are also reproduced in Table 2.1.

$$\rho_{ss} = \rho_0 + \rho_i \quad \Omega/m, \quad \rho_i = \frac{P_1 T^{P_2}}{1 + P_1 P_3 T^{(P_2 + P_4)} e^{-(P_5/T)^{P_6}}} + \rho_c \tag{2.23}$$

For CO_2-H_2SO_4 measurements, the entire length of stainless steel waveguides are at the same temperature, which is the opacity measurement temperature inside the pressure

Table 2.1: Coefficients for Equation 2.23

Coefficient	Value
P_1	1.217×10^{-10}
P_2	1.315
P_3	6.836×10^6
P_4	0.3
P_5	450
P_6	3.031

vessel. For a temperature of 533 K and a frequency of 75 GHz, the theoretical loss inside both stainless steel waveguides is 2.9 dB. This is in agreement with empirical measurements of loss inside these waveguides prior to assembly and to other stainless steel waveguide measurements [63]. Errors for these losses can safely be given as $\pm$ 0.1 dB.

2.4.2 Copper Waveguides

Matula gives an empirical expression for the variation of copper conductivity with temperature also in the form of Matthiessen's rule. In this case, the ρ_i term is an empirical variation of the Bloch-Grunheisen formula [64]. The complete expression has been reproduced below in Equation 2.24 and 2.25, and the coefficients for the second half of the equation are given in Table 2.2

$$\rho_{copper} = \rho_0 + \rho_i \quad \Omega/m, \quad \rho_i = A \left[1 + \frac{BT}{\theta - CT} + D \left(\frac{\theta - CT}{T} \right)^p \right] \Phi \left(\frac{\theta - CT}{T} \right) \tag{2.24}$$

$$\Phi(x) = \frac{4}{x^5} \int_0^x \frac{z^5 e^x}{(e^z - 1)^2} dz \tag{2.25}$$

Unlike the stainless steel waveguides, the copper waveguides external to the pressure vessel are kept at cooler temperatures for the W and F Band experiements. Portions of the waveguides closer to the pressure vessel are at temperatures closer to that of the oven housing the semi-confocal resonator. By contrast, the portions of the copper waveguides

Table 2.2: Coefficients for Equation 2.24

Coefficient	Value
A	1.8089×10^{-8}
B	-5.9991×10^{-3}
C	0.04563
D	-6.4760×10^{-4}
θ	310.8
p	1.84

farther from the oven are kept in an ice bath at close to 0 C to prevent overheating of the amplifiers and mixers. The remaining portions of the waveguides are at temperatures between these two points. To account for these variations in temperature, the losses in the waveguide were calculated assuming both waveguides were kept at room temperature, and an error figure is incorporated taking into account the difference in resistivities between room temperature, freezer temperature, and oven temperature copper. While calculations of loss through the copper waveguides at 533K and 75 GHz yields a theoretical loss of 3.62 dB, close to this much loss was measured for just one waveguide. For the final calculations, a loss of 4 dB per waveguide was used with an error term given by the resistivity variations with temperature.

2.4.3   Windows and Apertures

The remaining sources of loss in the signal transmission are the apertures cut into the endplate of the pressure vessel closest to the flat mirror and the PTFE (Teflon) disc windows, which are inserted to ensure that no gases within the pressure vessel escape through these apertures. FEM simulations of PTFE at 12 GHz suggest losses less than 1 dB for pieces thinner than 30 millimeters [65]. The PTFE windows used are less than 5 millimeters thick, and are considered to be negligible sources of attenuation. This can also be said for the waveguide apertures in the endplate. To ensure this, the attenuation through both window/waveguide assemblies was measured, and the signal loss at all frequencies measured

was found to average 0.1 dB ± 0.1 dB.

2.5 Band-dependent Specifications

2.5.1 W Band (75-110 GHz)

The flat mirror for the W Band system is of equivalent diameter to the curved mirror (3.5 inches) with iris diameters of 1 millimeter. The signal source for all measurements is an HP 83650B sweep signal generator that can generate signals at frequencies from 10 MHz to 50 GHz. The output of the signal generator is amplified and frequency-multiplied by a factor of six using a Millitech AMC-10-RFH00 active multiplier chain (AMC). Copper WR-10 waveguide transfers the output of the AMC to the pressure vessel within the temperature chamber. The waveguide apertures transfer the signal from the external copper waveguide to stainless steel WR-10 waveguides inside the vessel, which couples the energy to the resonator. Energy exits the resonator through a similar path where it is down-converted using a Quinstar 922WHP/387 harmonic mixer and a Pacific Millimeter MD1A diplexer. Conversion loss in the harmonic mixer attenuates the signals by 40 dB. The frequency-swept signal is then measured using a HP 8564E spectrum analyzer. A block diagram of the measurement system is shown in Figure 2.5.

2.5.2 F Band (90-140 GHz)

For initial testing, the W Band system flat mirror was also used for measurements in the F Band. Due to the shorter wavelength of operation, higher-order resonant mode degeneracy became apparent in the form of split-peak resonances. Reducing the diameter of the flat mirror to 2 inches eliminated this problem. The sweep generator is operated closer to its limit of 50 GHz, and the output of the sweep generator connects to a Spacek Labs SG4413-15-16W Q Band Amplifier. The amplifier output is then tripled in frequency using a Pacific Millimeter F3WO Frequency Tripler. On the receiving end, a Pacific Millimeter DM harmonic mixer and MD2A diplexer demodulate the signal. The LO signal for down-
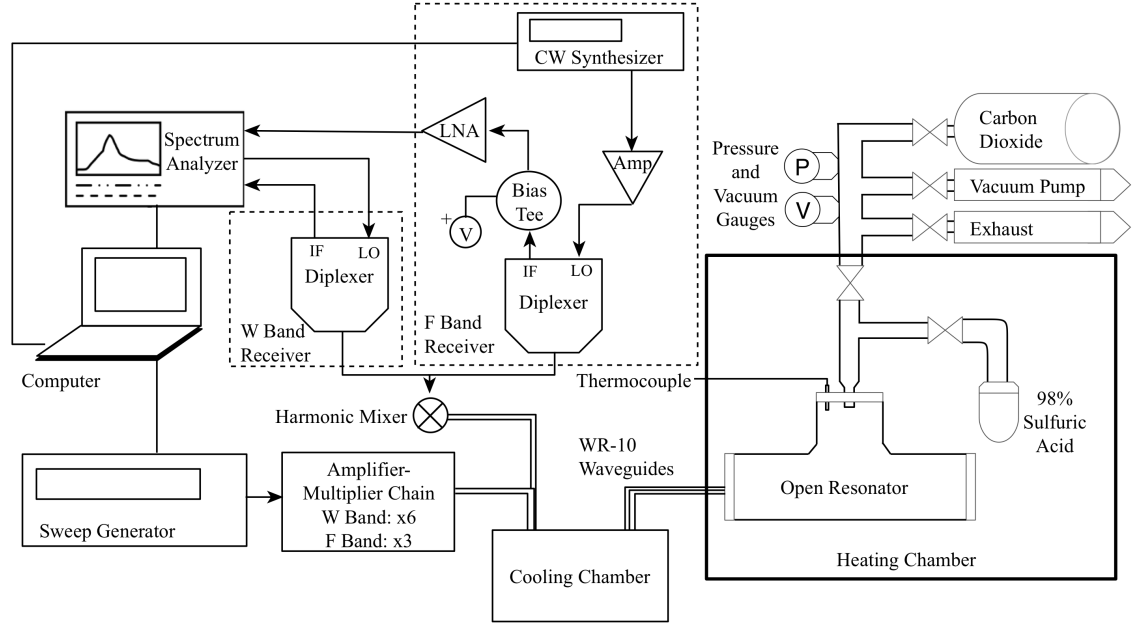
Figure 2.5: High temperature H_2SO_4 vapor measurement system for W and F Band

conversion is driven by an HP 83712B continuous wave synthesizer that is amplified by a JCA 1920-612 amplifier. For proper operation of the harmonic mixer, a bias tee is connected to the IF output to properly bias the receiver diode in the harmonic mixer. The bias voltage supplied by the bias tee can affect the sensitivity of the receiver. A bias voltage of 5.3 V applied to the bias tee in series with a 1 kΩ resistor was found to maximize the system sensitivity. The IF signal is amplified by a MITEQ AMF-3F-012017 Low Noise Amplifier before transfer to the spectrum analyzer. The center frequency of the MITEQ LNA is 1 GHz, so the LO signal must be varied to ensure that the frequency of each measured resonance is converted down to this range. The LO frequency is given by Equation 2.26, where f_{LO} is the generated LO frequency, f_{RF} is the output frequency from the resonator, and f_{IF} is the desired output frequency to the spectrum analyzer. The value of N_H is the lowest integer such that the LO frequency is below 18 GHz.

$$f_{LO} = \frac{f_{RF} - f_{IF}}{N_H} \tag{2.26}$$

More details on the hardware components of the W and F band measurement systems

25

are given in the Ph.D. thesis of Devaraj [53].

2.5.3 K$_a$ Band (27-40 GHz)

For the K$_a$ Band system, the flat mirror is chosen to have the same diameter as the curved mirror. Due to the longer wavelength of operation, the coupling iris diameters were widened to 2.5 millimeters. Stainless steel WR-28 waveguides were used as transmission lines inside the pressure vessel. A slight modification was also made to the waveguide aperture and window configuration on the inside of the pressure vessel. During initial tests of the K$_a$ Band system, it was found that significant cross-coupling occured between the waveguide aperture and PTFE window assemblies on the inside of the pressure vessel. This did not occur for the W and F Band systems due to the shorter operating wavelength, increased distance between the bases of the WR-10 stainless steel waveguides, and the presence of a metal extrusion that is part of the manufacturing standard for the waveguide flanges. To mitigate the coupling for the K$_a$ Band system, thin stainless steel disks with WR-28 waveguide apertures were machined and placed between the PTFE disks and the WR-28 waveguides. Since K$_a$ Band frequencies are within the generation range of the sweep signal generator, the transmission chain is considerable simpler than for the shorter wavelength systems. The sweep signal generator output is transmitted to the input port of the resonator using a Times Microwave SiO$_2$ dielectric cable to a WR-28 waveguide via coaxial-to-waveguide adaptor. The output port couples to a similar waveguide, which is itself connected to a longer flexible waveguide to provide heat insulation to the receiving electronics. The output signal is amplified using the Spacek Q Band amplifier prior to down-mixing using a Tektronix WM490A mixer and the Pacific Millimeter MD1A diplexer. A 3 dB attenuator was placed at to the LO diplexer input port to ensure that the LO signal was below the maximum specification of the diplexer. The output signal is measured using an HP8562B spectrum analyzer. The spectrum analyzer provides a bias voltage to the Tektronix mixer through the IF path of the diplexer, and this bias voltage is empirically determined for each resonance
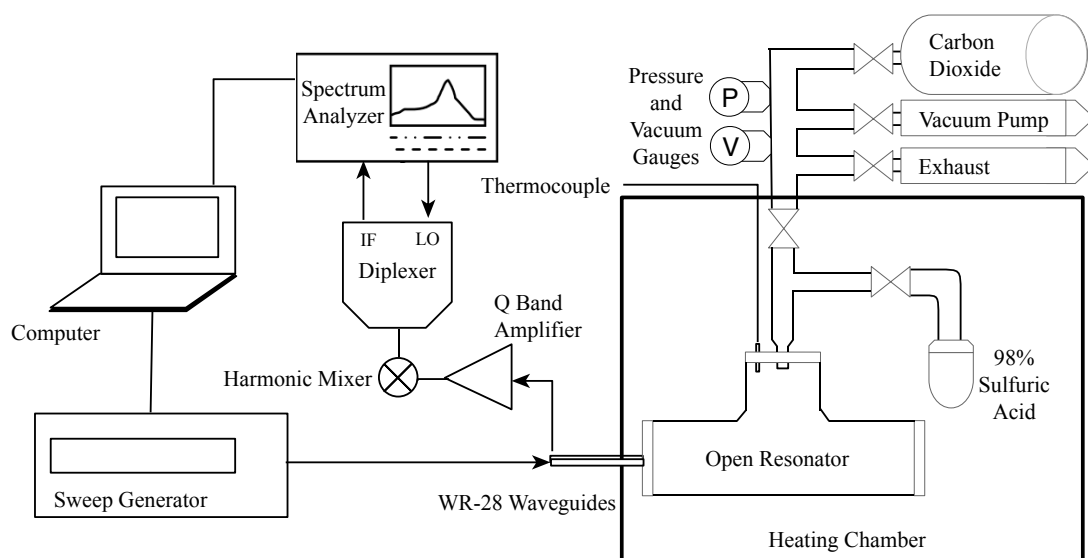
Figure 2.6: High temperature H_2SO_4 vapor measurement system for K_a Band

to maximize the signal to noise ratio. A block diagram of the measurement system is shown in Figure 2.6.

2.6 Measurement Procedure

The first step in the measurement procedure is the sealing of the pressure vessel. Viton O-rings are sandwiched between the pressure vessel and the endplates, and the endplates are tightened down under vacuum to ensure maximum seal. The system is tested at vacuum and three bars of pressure for twelve hours to ensure seal integrity, and the initial measurements of resonances are made to characterize the quality factor, peak frequency, and resonance asymmetry. After the assembly has passed these initial tests, a precise amount of 98.07% H_2SO_4 solution (by mass) is added via a one milliliter syringe with a graduation of 0.05 milliliters and a 0.2 milliliter needle to a borosilicate glass reservoir, which is connected to the 3/8" Swagelok stainless steel piping configuration. Once the H_2SO_4 reservoir is connected, a vacuum is drawn in the pressure vessel, the temperature chamber and waveguide cooling chamber are connected to power, and the system gradually rises to

27

measurement temperature. The heating coils within the oven are driven by a 220 V line providing 16 amps of current. The temperature within the oven is monitored with a thermocouple connected to a Micromega CN77000 controller, which drives a mechanical relay between the coils and the power line. Stabilization of temperature within the chamber is a process that takes at least eight hours, and the resonances are monitored during heating to observe any notable shifts. The heating processes causes expansion in the PTFE windows and the Viton O-rings, enhancing their seal. After temperature stabilization, as determined via measurements of the Type T pipe plug thermocouple connected to a pressure vessel endplate, initial measurements are made of all resonances under vacuum conditions. Temperature and pressure are recorded once per measurement cycle. After the first vacuum measurement, the valve connecting the H_2SO_4 reservoir is opened for 5 minutes, allowing vapor to boil off and the vapor pressure of the system to stabilize. Due to the small size of the reservoir, the saturation vapor pressure of H_2SO_4 will not be fully reached. The valve is closed once again, and more time is taken to allow the thermal conditions within the oven to stabilize.

Following stabilization, the center frequency and quality factor of the shifted resonances are measured. After the measurements of the effects of the H_2SO_4 vapor, one, two, and three bars of carbon dioxide are added to pressure broaden the absorption spectrum of H_2SO_4 vapor, and resonances are measured following each addition of gas. The carbon dioxide gas is added to the system at a near-adiabatic rate so as to prevent the condensation of any H_2SO_4 vapor within the chamber. After measurements at the higher pressure are taken, the system is vented back down to the lower pressures while maintaining the same mole fraction. Thus, additional measurements are obtained at 1 and 2 bars with consistent mole fractions of H_2SO_4. After the final measurement, the gas is drawn out of the system and flushed three times with carbon dioxide over the course of fifteen minutes. A vacuum is then drawn in the pressure vessel, and another measurement cycle is performed to monitor any shift in the center frequency of resonances under vacuum. Finally, the resonator

system is loaded with carbon dioxide from 1 to 3 bars of pressure for dielectric matching measurements, during which the quality factors and center frequencies of the resonances are measured.

Following the completion of a successful measurement sequence, the temperature chamber and waveguide cooling chamber are shut down, and the system is allowed to cool down to room temperature. The H_2SO_4 solution reservoir is disconnected from the piping system, and the volume of the remaining contents is measured using a syringe and graduated cylinders with .01 milliliter accuracy. This will enable the determination of the amount of H_2SO_4 in vapor phase during the experiments, using the method outlined in Appendix A. The signal path electronics and transmission lines are disconnected from the pressure vessel, reconnected in series, and transmissivity measurements are made. At least three trials of transmissivity measurements are made, and between each measurement, the coaxial cables connecting the signal path electronics are disconnected and reconnected to incorporate the variable lossy effects of cables. Between each measurement, all O-rings and PTFE windows are replaced, as repeated use increases the likelihood of seal failure. The condition of the resonator mirror gold plating is also monitored for signs of corrosion. Gloves are worn at all times while handling the contents of the pressure vessel to present the deposition of finger oils onto any surfaces.

As discussed in Appendix A, the mole fraction of H_2SO_4 vapor is inferred from measurements of the remaining volume of the H_2SO_4 liquid solution and calculations of the H_2SO_4 evaporate dissociation balance. However, it is possible that H_2SO_4 vapor could exit vapor phase once introduced into the chamber. For the initial exposures of the pressure vessel to the H_2SO_4 evaporates, a thin opaque film formed on the interior of the borosilicate glass, likely due to the presence of iron impurities that were doped into the glass to increase its strength. A thin buildup was also apparent on the stainless steel endplates. Following the first few exposures and re-exposure to oxygen at room temperature, the surfaces were effectively passivated, limiting future buildup. It is unlikely that H_2SO_4 will adsorb

onto the surfaces of the pressure vessel due to the high temperature of the experiment. It was also discovered in early experiments that H_2SO_4 was exiting vapor phase due to an increase buildup on the endplate holding the flat mirror. This endplate was the closest to the feedthrough area for the waveguides, and by recessing the pressure vessel further into the oven, it was possible to mitigate this effect. Operation within a temperature chamber that is free of substantial thermal gradients is necessary for the successful execution of this experiment. For some experiments, corrosion scars were observed on the gold-plated mirrors. Since gold cannot be plated directly onto stainless steel, the steel must first be activated with a nickel layer prior to gold flashing. In regions of weaker plating, or following multiple exposures, the H_2SO_4 vapor can react with the nickel layer. This can be mitigated by making the gold plating thick, on the order of several microns. The addition of CO_2 gas was undertaken at a rate of close to 1 psi/minute, to limit the change in temperature to the chamber and prevent further condensation. With the exception of the CO_2 addition, any loss of H_2SO_4 mole fraction with the pressure vessel occurs on the order of seconds. This was verified by monitoring resonance Q for a period of 2 hours following the addition of H_2SO_4 vapor. The data from these experiments can still be useful for model fitting by comparing the measured refractivity to that of other measurements.

2.7   Data Acquisition and Conditioning

The measurements are carried out using Matlab software procedures initially developed by Hanley and modified by various users [57]. The sweep times for the signal generator and spectrum analyzer are coordinate using an HP 33120A function generator, and a stable 10 MHz reference frequency is provided from an Agilent E5071C vector network analyzer with an ultra-stable oscillator. Data is transferred to and from these devices using a GPIB bus which interfaces with the governing computer through a Prologix GPIB-USB converter. Resonances are located using one second synchronized sweeps of the signal generator and spectrum analyzer, but the final measurements of the resonance that are used to determine

the absorptivity are made by changing the sweep time to 75 milliseconds for the signal generator and 40 seconds for the spectrum analyzer. The resolution bandwidth for these measurements is on the order of 100 kHz for the W and F Band measurements and 30 kHz for the K_a Band measurements. Three to five long sweeps of the spectrum analyzer are taken, and the resulting measured resonances include sweep-on-scan nulls due to periodic misalignment of the sweep times. These nulls are corrected through the application of averaging filters to the measured sweeps. The peak frequency, half power bandwidth, peak amplitude, and resonance asymmetry are then determined from the corrected resonance measurement. These values are then used to determine the change in Q and shift in center frequency for each measurement condition from which measurements of the absorptivity and refractivity of the gas can be derived.

To isolate the effects of H_2SO_4 vapor on the measured absorption, the contribution due to CO_2 and H_2O vapor must be removed. Based on its lack of a dipole moment and its centimeter-wavelength transparency, it is assumed that SO_3 is effectively transparent at millimeter wavelengths [38]. Use of CO_2 as the dielectric matching gas permits the separation of the absorption from pressure-broadened H_2SO_4 vapor from the intrinsic opacity CO_2, since the equivalent density of CO_2 must be used to match the resonant frequency of the H_2SO_4/CO_2 mixture-loaded resonance. Due to dissociation, H_2O vapor is also present in the pressure vessel during all experiments. Most models for H_2O absorption at microwave and millimeter-wavelengths consist of a spectral line contribution and a continuum contribution [66]. For the spectral line contribution, the JPL spectral line catalog is used [67], and the linewidths and temperature coefficients for CO_2 broadening of H_2O spectral lines use the values calculated by [68], where $\Delta\nu$ = 6.24 MHz/torr and the corresponding temperature coefficient is 0.57 for the 183 GHz line. Absorption due to the 183 GHz line is the dominant line contribution for the conditions relevant to this work. For the continuum absorption contribution (α_c), the continuum model of [69] for absorption of H_2O and CO_2

31

mixtures at 239 GHz as a function of temperature is extrapolated to lower frequencies (ν).

$$\alpha_c = \nu^2 p_{H_2O} \left(a(T) p_{CO_2} + b(T) p_{H_2O} \right) \quad \text{cm}^{-1}/\text{Torr} \qquad (2.27)$$

$$a(T) = 8.21 \times 10^{-14} \left(\frac{296}{T} \right)^{5.07}, \quad b(T) = 6.022 \times 10^{-13} \left(\frac{296}{T} \right)^{7.84} \qquad (2.28)$$

The resulting continuum and spectral line opacity due to the presence of H_2O is subtracted from the measured absorption, and the remaining value is assumed to be solely resulting from H_2SO_4 vapor.

2.8 Measurement Uncertainty

Several features of the procedure outlined previously can give rise to errors in the measured absorption of H_2SO_4 vapor. This section constrains the most important of these errors, representing 2σ uncertainties. There are two major types of error that are accounted for in this measurement procedure. The first kind are statistical measurement errors related directly to the measurement procedure for millimeter-wavelength opacity that can be accounted for via propagation of errors. The second kind of errors relates to the uncertainties in knowledge of the environmental conditions under which the experiments are made (pressure, temperature, and constituent mole fraction), and do not directly affect the uncertainties in measured opacity.

2.8.1 Statistical Measurement Errors

Statistical measurement errors include errors due to dielectric matching, resonance asymmetry, instrumental variations, and errors in measurement of the system transmissivity [57]. Due to the statistical nature of these errors, they can be combined into a total error term

Err_{tot} as given by Equation 2.29.

$$Err_{tot} = \sqrt{Err_{inst}^2 + Err_{diel}^2 + Err_{asym}^2 + Err_{trans}^2} \qquad (2.29)$$

Instrumental Errors

The instrumental measurement error represents the combination of errors resulting from electrical noise and the limited sensitivity of the measurement equipment. Electrical noise results from thermal, shot, and flicker noise from the signal generators, the spectrum analyzer, and the other mixers and amplifiers in the signal chain. The probability distribution of this noise is assumed to be Gaussian, and the error due to the noise can be calculated using Equation 2.30, where S_N is the sample standard deviation of the quality factor measurements, n is the number of measurements, and B is the confidence coefficient [57].

$$Err_N = \frac{BS_N}{\sqrt{n}} \qquad (2.30)$$

The measurements of center frequency and quality factor for given resonance are derived from five spectrum analyzer sweeps over a narrow bandwidth containing the peak and -3 dB points for each resonance. Due to the resolution and video bandwidth of the spectrum analyzer, the statistically optimum duration for these sweeps is 40 seconds. While the peak frequency is determined by finding the maximum value of each raw sweep, the quality factor of the resonances are estimated by iteratively applying ten and four point moving average filters to the resonance sweeps. The standard deviation of the quality factors can be calculated from these sweeps and Err_N is calculated using Equation 2.30 with a confidence coefficient of 2.776 [57].

Two components of the instrumental error result from the limited sensitivity of the spectrum analyzer: Err_0 representing the center frequency uncertainty and Err_Δ representing the uncertainty in half-power bandwidth. Expressions for these error terms are found in the reference manual for the Hewlett-Packard 8564E spectrum analyzer, and they are re-

produced here. RBW is the resolution bandwidth setting, N is the mixer integer, and LSD is the least significant digit of the measured value. For the W-Band measurements, N = 18, and for the F-Band measurements, N = 1. For the least significant digit, $LSD = 10^x$ for the smallest positive integer value of x where $SPAN < 10^{x+4}$. In the equation for $f_{reference}$, t_{cal} is the time in seconds since the spectrum analyzer was last calibrated, which was December 5th, 2005.

$$Err_0 < \pm \left(f_{reference} \times f_{measured} + 0.15 \times RBW + 0.01 \times SPAN + 10 \right) \qquad (2.31)$$

$$Err_\Delta < \pm \left(f_{reference} \times BW_{measured} + 4 \times N + 2 \times LSD \right) \qquad (2.32)$$

$$f_{reference} = 10^{-7} \times t_{cal} + 3.2 \times 10^{-8} \qquad (2.33)$$

For resonance measurements where $SPAN > 2MHz \times N$, the SPAN coefficient in Equation 2.31 is changed to 0.05. It should also be noted that these equations give 3σ uncertainty values, and they are multiplied by 2/3 to give the corresponding 2σ values.

Analysis of the propagation of the aforementioned errors to 2σ uncertainties in the measured absorption is given by DeBoer and Steffes and summarized in the following equations [70].

$$Err_{inst} = \frac{20 log_{10}(e)\pi}{\lambda} Err_\psi \quad (dB/km) \qquad (2.34)$$

$$Err_\psi = \sqrt{\Gamma_l^2 + \Gamma_m^2 - 2\Gamma_l\Gamma_m} \qquad (2.35)$$

34

$$\Gamma_i^2 = \frac{\gamma_i^2}{f_{0i}^2} \left[\frac{Err_0^2}{Q_i^2} + Err_\Delta^2 + Err_{Ni} + \frac{2Err_0Err_\Delta}{Q_i} \right], \text{ i=l,m} \qquad (2.36)$$

$$\Gamma_l\Gamma_m = -\frac{\gamma_l\gamma_m}{f_{0l}f_{0m}} \left[\frac{Err_0^2}{Q_lQ_m} + Err_\Delta^2 + \frac{Err_0Err_\Delta}{Ql} + \frac{Err_0Err_\Delta}{Qm} \right] \qquad (2.37)$$

$$\gamma_i = 1 - \sqrt{t_i}, \text{ i = l,m} \qquad (2.38)$$

For these equations, the subscripts l and m represent the gas-loaded and dielectrically matched measurement cases, respectively. λ is the wavelength in kilometers, t is the transmissivity, f_0 is the resonance center frequency, and Q is the resonance quality factor.

Dielectric Matching Errors

As discussed previously, the center frequency of a resonance shifts when a gas is introduced into the path of the resonant system. The effect of this refractive shift on the quality factor of the resonance is not easily determined. To reduce uncertainty in the measured absorption, the gas-loaded resonance must be compared to the corresponding resonance with the same resonance frequency. This is accomplished by adding a non-absorptive gas (CO_2 for this work) to the chamber until the resonance center frequency shifts to that of the gas-loaded resonance. However, this dielectric matching procedure is not perfect, i.e. there still exists a small discrepancy between the gas-loaded resonance center frequency and the matched resonance center frequency. The 2σ error due to this discrepancy is estimated by linearizing the change in quality factor with frequency and propagating the expected change in quality factor as a result of the introduction of the gas into the expression for absorption. This operation is summarized in the equations below.

$$\frac{dQ}{df} = \left| \frac{Q_{vac} - Q_{matched}}{f_{vac} - f_{matched}} \right| \qquad (2.39)$$

35

$$dQ = \frac{dQ}{df} \times |f_{loaded} - f_{matched}| \tag{2.40}$$

$$Err_{diel} = \frac{20log_{10}(e)\pi}{\lambda} \times$$
$$\left| \left(\frac{1 - \sqrt{t_{loaded}}}{Q_{loaded}} - \frac{1 - \sqrt{t_{matched}}}{Q_{matched} + dQ} \right) - \left(\frac{1 - \sqrt{t_{loaded}}}{Q_{loaded}} - \frac{1 - \sqrt{t_{matched}}}{Q_{matched} - dQ} \right) \right| \text{(dB/km)} \tag{2.41}$$

Asymmetry Errors

Asymmetries in the measured resonances introduce an uncertainty into the resulting absorption value. To account for this error, a maximum and minimum resonance bandwidth are calculated using the upper and lower -3dB points of the resonance curve. These bandwidths are used to calculate maximum and minimum values of the resonance quality factor, which are then propagated to the absorption expression to estimate the 2σ uncertainty as shown in Equation 2.42.

$$Err_{asym} = \frac{20log_{10}(e)\pi}{\lambda} \times$$
$$\left| \left(\frac{1 - \sqrt{t_{loaded}}}{Q_{loaded,high}} - \frac{1 - \sqrt{t_{matched}}}{Q_{matched,high}} \right) - \left(\frac{1 - \sqrt{t_{loaded}}}{Q_{loaded,low}} - \frac{1 - \sqrt{t_{matched}}}{Q_{matched,low}} \right) \right| \text{(dB/km)} \tag{2.42}$$

Equation 2.42 contributes a higher degree of uncertainty if the resonance asymmetry changes between the gas-loaded and the reference measurement.

Transmissivity Errors

Uncertainty in the transmissivity results from temperature dependent changes in waveguide/window conductivities and the sensitivity of certain components. The W559 20dB coupler used for transmissivity measurements has a specified $\pm$ 1 dB coupling accuracy in

the W Band. For F Band measurements, this is increased to $\pm$ 1.5 dB. The transmission errors due to temperature variations of the waveguide and aperture window components adds an additional degree of uncertainty. Information on the error ranges for these components was stated previously. Finally, noise-dependent errors in the measurement of the transmissivity also add to the uncertainty of the measurements. The sample standard deviation for n transmissivity measurements is derived from the following equation.

$$Err_{msl} = \frac{BS_N}{\sqrt{n}} \tag{2.43}$$

The L$_1$ norm of these terms forms the Err_{ins_loss} term, which is also a 2 σ error term. An L$_1$ norm is used here as opposed to the L$_2$ norm due to the fixed nature of these uncertainties. The values of the insertion loss are assumed to not change over the lifetime of the components.

$$Err_{ins\_loss} = Err_{msl} + Err_{coupler} + 2Err_{Cu\_waveguide} + 2Err_{Steel\_waveguide} + 2Err_{window} \tag{2.44}$$

The insertion loss error is then used to compute the associated transmissivity error

$$Err_{t,i} = \frac{1}{2}\left(10^{-(S_i - Err_{ins\_loss})} - 10^{-(S_i + Err_{ins\_loss})}\right) \tag{2.45}$$

This transmissivity error can then be propagated to the 2 σ error in the opacity resulting from uncertainty in transmissivity using the following equation [57].

$$Err_{trans} = \frac{20log_{10}(e)\pi}{2\lambda} \times$$
$$\left(\frac{\sqrt{t_l + Err_{t,l}} - \sqrt{t_l - Err_{t,l}}}{Q_l} - \frac{\sqrt{t_m - Err_{t,m}} - \sqrt{t_m + Err_{t,m}}}{Q_m}\right) \text{(dB/km)} \tag{2.46}$$

2.8.2 Errors in Knowledge of Measurement Conditions

The errors in knowledge of environmental conditions inside the pressure vessel are maintained separately from the statistical measurement errors, which represent uncertainty in measured absorption. Environmental condition errors result from limitations in the sensitivity of the temperature and pressure gauges as well as the uncertainty in the volume mole fraction of H_2SO_4 evaporates within the pressure vessel. The resulting effect on these uncertainties on absorption is estimated by using the maximum and minimum values of temperature, pressure, and mole fraction as inputs to a model for calculating the absorption. Since this error is model dependent, the modeled errors are re-calculated as the absorption model is fit to the data. For the Omega HH91 thermocouple thermometer, the uncertainty in temperature is 0.5% of the measured temperature + 0.5^{o}C. For the Omega DPG7000 pressure gauge, the uncertainty is 0.05% of the full scale pressure reading of 3.08 bar. Since the Omega DPG7000 is a relative pressure gauge, a Druck DPI 104 absolute gauge is used as a reference, and the error for this gauge is also 0.05% of the full scale value of 2 bar. The uncertainty in mole fraction is limited by the precision of the measurement of the final volume of the H_2SO_4 solution with a graduated cylinder, which is $\pm$ 0.02 mL. This uncertainty in measured volume is propagated to uncertainty of H_2SO_4 mole fraction by using the maximum and minimum values of the measured volumes as inputs to the method described in Appendix A. The values of mole fraction are then input into the modeled absorption expression to yield the associated absorption uncertainty. The resulting 2σ modeled absorption uncertainty is calculated from the temperature, pressure, and mole fraction dependent absorption uncertainties.

$$Err_{model} = \sqrt{Err_{temp}^2 + Err_{pres}^2 + Err_{mr}^2} \qquad (2.47)$$

38

CHAPTER 3

RESULTS AND MODEL OF SULFURIC ACID VAPOR OPACITY

The laboratory systems and procedures described in the previous chapter were used to carry out measurements of the millimeter-wavelength opacity of H_2SO_4 vapor under Venus conditions. The results of these laboratory experiments are now presented, and a model for the opacity of H_2SO_4 vapor from 1-150 GHz is determined from this dataset. The determined model is based the H_2SO_4 rotational spectrum as recorded in the JPL Submillimeter, Millimeter, and Microwave Spectral Line Catalog at the time of writing [67]. To account for the enhanced opacity of H_2SO_4 vapor at lower frequencies, scaling factors were applied to the spectral lines associated with elastic collisions. Several strategies for line scaling are discussed, and uncertainties are determined for the parameters of the final model.

3.1   Spectral Line Absorption

At certain wavelengths, atmospheric gases absorb electromagnetic radiation and undergo transitions in rotational, vibrational, or electronic energy states [71]. At low pressures, these state transitions occur over a narrow wavelength range, and an absorption feature within this narrow range is referred to as a spectral line. However, as the pressure of the gas increases, molecular collisions broaden the width of these spectral lines. For gas systems totaling a few bars of pressure, the pressure broadening of the spectral lines dominates any other broadening process. Pressure broadening of discrete spectral lines is determined through application of a spectral lineshape. The equation of molecular absorption by a gas is given below for a line center absorption A_j, a linewidth $\Delta\nu_j$, a lineshape F_j, and a scale

constant D.

$$\alpha = \sum_j DA_j \pi \Delta \nu_j F_j \left(\nu, \nu_{0,j}, \Delta \nu_j \right) \quad \text{cm}^{-1} \tag{3.1}$$

Conversion from cm^{-1} to dB/km units, which are more common for radio science, is obtained by multiplication of Equation 3.1 by $10^6 \log_{10}(e)$. The line center absorption A_j is calculated from the center frequencies $\nu_{o,j}$, intensities $I_{o,j}$, and the lower energy states E_o of the spectral lines for each constituent obtained from the JPL Submillimeter, Millimeter, and Microwave Spectral Line Catalog [67].

$$A_j = 102.458 \frac{T_o}{T} I_j \frac{p}{\Delta \nu} \quad \text{cm}^{-1} \tag{3.2}$$

$$I_j = I_{o,j} \left(\frac{T_o}{T} \right)^{(n_j+1)} e^{-\left(\frac{hc}{k} E_o \left(\frac{1}{T} - \frac{1}{T_o} \right) \right)} \quad \text{nm}^2 \text{MHz} \tag{3.3}$$

There are several theoretical lineshape treatments that have been developed, each with its own corresponding assumptions about the nature of the molecular collision that gives rise to the pressure broadening [71]. Lorentz postulated a lineshape based on the assumption of arbitrary phase of oscillation following a strong collision, and Debye developed a separate lineshape under the assumption that the molecular dipole would be oriented with respect to the electric field following a collision. Van Vleck and Weisskopf synthesized these approaches, developing the Van Vleck-Weisskopf lineshape, which is commonly employed at centimeter and millimeter-wavelengths. In the equation below, ν is the frequency of interest, $\nu_{0,j}$ is the spectral line frequency at low pressures from a catalog, and $\Delta \nu$ is the linewidth.

$$F_{j,VVW} \left(\nu, \nu_{0,j}, \Delta \nu_j \right) = \frac{1}{\pi} \left(\frac{\nu}{\nu_{0,j}} \right)^2 \left(\frac{\Delta \nu_j}{(\nu_{0,j} - \nu)^2 + \Delta \nu_j^2} + \frac{\Delta \nu_j}{(\nu + \nu_{0,j})^2 + \Delta \nu_j^2} \right) \quad \text{MHz}^{-1} \tag{3.4}$$

The width of a given spectral line can be roughly described as dependent on the gas number density, the molecular velocity, and the collisional diameter of the gas.

$$\Delta \nu = \frac{N v \sigma}{2\pi} \tag{3.5}$$

Experiment observations of the linewidths associated with different broadening gases have determined that a collisional diameter predicted by kinetic theory does not align well with observed line broadening. This is largely due to the interaction of the dipole and quadrupole moments of the gases involved. Gas molecules with a large dipole moment will contribute substantially to pressure broadening, whereas non-polar gases will contribute less. Therefore, the linewidth must be empirically determined. The linewidth $\Delta \nu$ can be further decomposed into a pressure-dependent expression based on self broadening and foreign gas broadening of the spectral line. γ is the pressure-dependent linewidth parameter in MHz/torr, p is the gas pressure in torr, T is the temperature of the gas, T_o is a reference temperature of 300 K, and m is the temperature dependence of the line broadening. The temperature dependence of the linewidth parameter ranges between -0.5 and -1 [71].

$$\Delta \nu = \sum_i \gamma_i p_i \left(\frac{T_o}{T}\right)^{m_i} \tag{3.6}$$

3.1.1 Rotational Spectrum of H_2SO_4

Due to its molecular structure, H_2SO_4 is known as an asymmetric rotor, and the rotational spectral lines in the JPL catalog are described using the J, K_-, and K_+ quantum numbers (which are always integers) [71]. The J number gives total angular momentum L of the molecule,

$$L^2 = \frac{J(J+1)h^2}{4\pi^2} \tag{3.7}$$

For symmetric top molecules, such as NH_3, the K quantum number gives the compo-

nent of angular momentum about the symmetry axis of the molecule

$$L^2_{sym} = \frac{K^2 h^2}{4\pi^2} \tag{3.8}$$

The K quantum number can take 2J+1 values ranging between -J and +J. For asymmetric rotors, which do not have a single axis of molecular symmetry, the rotational transitions are described by splitting the K number into K_- and K_+ which describe the component of angular momentum about the limiting oblate and prolate spheroidal top symmetry axes for the molecule, respectively[1]. Each spectral line for asymmetric rotors in the JPL catalog is provided with the values of J, K_-, and K_+ for the upper and lower states of the transition associated with photon emission or absorption. For state transitions where J changes, the total angular momentum of the molecule is modified, and transitions are therefore referred to as inelastic transitions. State transitions where the total angular momentum remains the same but changes occur in the K quantum numbers are referred to as elastic transitions. Figure 3.1 shows a subset of the rotational spectrum of H_2SO_4 from 1-150 GHz from the JPL catalog. The full catalog lists 44,221 lines at frequencies ranging from 10 MHz to 1 THz.

The rotational spectral lines for H_2SO_4 associated with inelastic transitions are clustered in groups which are spaced apart by roughly 10 GHz. Several of these lines have been observed in the laboratory, and they have been used to calculate structural parameters of the H_2SO_4 molecule as well as the dipole moment [73, 74, 72]. The derived structural parameters are used to estimate the intensity of the lines associated with elastic transitions, but these lines have not been studied in the laboratory.

---

[1]This convention for the K quantum numbers is used for the JPL Catalog, but often, the opposite convention is used in the literature.
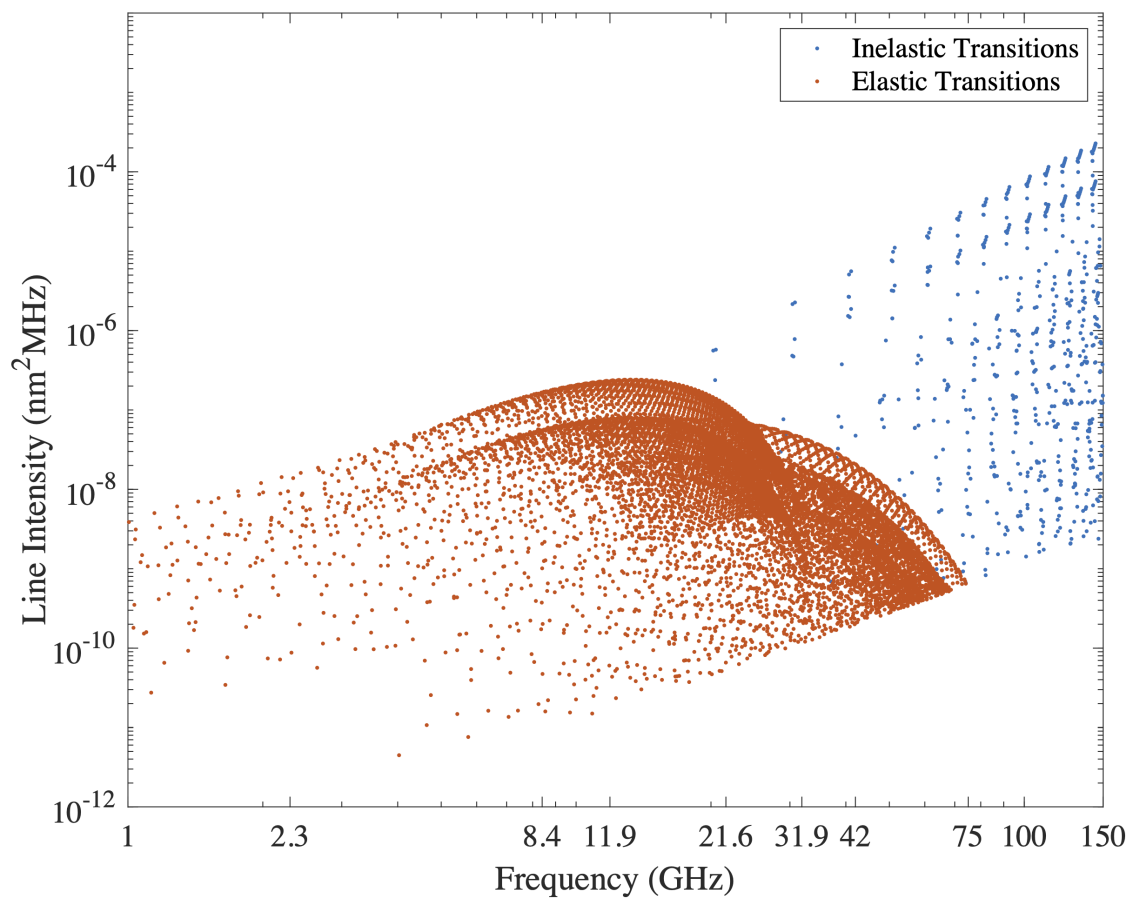
Figure 3.1: Inelastic and elastic collisional transitions for H_2SO_4 from 1-150 GHz [67, 72].

3.2 Band-specific Models of H_2SO_4 Vapor Absorption

For the microwave measurements of H_2SO_4 vapor opacity under Venus conditions conducted by Kolodner and Steffes, continuum models were developed to describe the absorption of H_2SO_4 vapor both at specific measurement frequencies and over the 2-21 GHz band [41]. Due to the revised calculations of H_2SO_4 vapor mole fraction present during experiments presented in Appendix A, these expressions have be updated. New expressions are determined by minimizing the cost function described by Kolodner and Steffes,

$$\min\left(\chi^2\right), \chi^2 = \sum_n \frac{\left(\alpha_{measured}/q - \alpha_{model}/q\right)^2}{\left(Err_{tot}\right)^2}, \tag{3.9}$$

where q is the revised mole fraction of H_2SO_4 vapor. Local minimization of Equation 3.9 is performed using a limited-memory Broyden-Fletcher-Goldfarb-Shanno algorithm with box bounds (L-BFGS-B) [75] as implemented in the SciPy package within the Python programming language.

The following models are derived using this procedure:

$$(\alpha/q)_{2.26 \text{ GHz}} = 138.73 p^{1.182} \left(553/T\right)^{3.2} \tag{3.10}$$

$$(\alpha/q)_{8.39 \text{ GHz}} = 600.92 p^{1.097} \left(553/T\right)^3 \tag{3.11}$$

$$(\alpha/q)_{11.89 \text{ GHz}} = 972.22 p^{1.185} \left(553/T\right)^{2.9} \tag{3.12}$$

$$(\alpha/q)_{21.61 \text{ GHz}} = 2746.51 p^{0.914} \left(553/T\right)^3 \tag{3.13}$$

$$(\alpha/q)_{2\text{-}21 \text{ GHz}} = 60.44 p^{1.088} f^{1.165} \left(553/T\right)^3. \tag{3.14}$$

For these expressions, α is given in dB/km, pressure p is in bars, the temperature T is in Kelvins, and the frequency f is in GHz. The expressions given for the absorption of H_2SO_4 vapor near 2 and 8 GHz are particularly relevant due to their applicability to radio occultation experiments conducted using Deep Space Network (DSN) ground stations. As the DSN also enables radio occultation experiments at 32 GHz, a single-frequency model has been developed for the new laboratory data nearest 32 GHz using the same fitting procedure.

$$(\alpha/q)_{32\,\text{GHz}} = 3456.361 p^{0.949} \left(553/T\right)^3 \tag{3.15}$$

As shown in Equation 3.14, the Kolodner and Steffes model for the opacity of H_2SO_4 vapor increases monotonically with frequency. The results of the new laboratory experiments demonstrate that this is not the case, and they provide motivation for the development of a new model for the microwave and millimeter-wavelength opacity of H_2SO_4 vapor.

In the process of making these measurements, a model was fit to the obtained 75-150 GHz laboratory data using the JPL Spectral Line Catalog. This model (referred to hereafter as the millimeter-only model) was fit through weighted and regularized cost function minimization, shown in Equation 3.16. C_r represents a regularization term, and $Err_{2\sigma}$ is the measurement 2σ uncertainty. Absorption measurements for which the 2σ uncertainty is greater than the measured absorption value are not included in the fitting procedure.

$$\min\left(\chi^2\right), \chi^2 = \sum_n W_n \frac{\left(\alpha_{measured} - \alpha_{model}\right)^2}{Err_{2\sigma}^2} + C_r \tag{3.16}$$

The term W_n represents the data weight assigned to each measurement point based on the following expression.

$$W_n = \frac{1}{f_{count}} + \frac{1}{T_{count}} + \frac{1}{p_{count}} + \frac{1}{C_{count}} \tag{3.17}$$

Equation 3.17 is calculated by dividing each data point into a frequency f, temperature

T, pressure p, and H_2SO_4 vapor concentration C bin and counting the amount of data within each bin. This weight represents a form of regularization, prohibiting the model fit process from being too reliant on a particular region of the measurement space that is over-represented. Tables 3.1 and 3.2 describe the laboratory data used for the millimeter-only model fitting grouped by frequency, temperature, pressure, and H_2SO_4 vapor concentration.

Table 3.1: H_2SO_4 vapor absorption measurement count by frequency and temperature

Frequency range (GHz)	f_{count}	Temperature Range (K)	T_{count}
$70 \leq f < 100$	171	$T < 545$	61
$100 \leq f < 120$	34	≥ 545	179
$120 \leq f$	35		

Table 3.2: H_2SO_4 vapor absorption measurement count by mixture pressure and H_2SO_4 vapor concentration

Pressure range (bars)	P_{count}	Concentration range (%)	C_{count}
$p < 0.5$	50	$C < 1$	124
$0.5 \leq p < 1.5$	57	$1 \leq C < 10$	68
$1.5 \leq p < 2.5$	79	$C \geq 10$	48
$2.5 \leq p$	54		

H_2SO_4 vapor partially dissociates into SO_3 and H_2O vapor in a ratio specified by the equilibrium coefficient of dissociation. The equilibrium mixture of these constituents can be referred to collectively as the H_2SO_4 evaporates. To derive line-broadening parameters for the H_2SO_4 evaporates, regularization is employed using physically realistic assumptions. This regularization is applied as the constant C_r in Equation 3.16. Molecular collisions that populate or depopulate microwave and millimeter-wavelength spectral line transitions depend on the polarizability of the molecules involved. This implies that the predominant interactions are dipole-dipole interactions for collisions between polar molecules or dipole-quadrupole interactions for collisions between a polar and a non-polar molecule. The stronger the dipole, the more substantial the pressure broadening of the spec-

tral lines. Taking NH_3 as an example, the linewidth due to self-broadening is almost four times greater than that due to CO_2 broadening [71]. It is therefore reasonable to assume the polar molecules (H_2SO_4 and H_2O) will broaden the lines to a greater degree than the non-polar SO_3 during collisions. Additionally, H_2SO_4 self-broadening should be greater than that of H_2O, due to its larger dipole moment. According to microwave collisional theory, the line width parameter is proportional to the product of the dipole moments between colliding molecules [71]. The dipole moment of water μ_{H_2O} is 1.855 Debye, and the dipole moment of sulfuric acid $\mu_{H_2SO_4}$ is 2.964 Debye [76, 74]. A regularization term was introduced in the fit to enforce this dipole moment relationship. In the absence of any quantitative information on the effective collisional cross section or quadrupole moment of SO_3, the SO_3 broadening parameter has been assumed to be equal to or slightly greater than the CO_2 broadening parameter, due to the larger size of the molecule. These relationships, and an additional term limiting the broadening ascribed to H_2O and H_2SO_4 vapor, are then incorporated into the regularization constant C_r with λ weight terms. The weight terms were set by choosing the maximum value such that the regularization parameters were not exactly enforced.

$$C_r = \lambda_1 \left| \frac{\gamma_{H_2SO_4}}{\gamma_{H_2O}} - \frac{\mu_{H_2SO_4}}{\mu_{H_2O}} \right| + \lambda_2 \left| \gamma_{CO_2} - \gamma_{SO_3} \right| \tag{3.18}$$

Table 3.3 summarizes the resulting parameters of the derived model.

Table 3.3: Derived parameters for millimeter-only model

$\gamma_{H_2SO_4}$	101 ± 6 MHz/torr
γ_{H_2O}	79 ± 9 MHz/torr
γ_{SO_3}	6 ± 2 MHz/torr
γ_{CO_2}	4.32 ± 0.14 MHz/torr
m	0.50 ± 0.01
D	1.09 ± 0.02

3.3 Laboratory Results and Full Model

The frequency-dependent centimeter and millimeter-wavelength models described in the previous section are not consistent with each other or the results of the 7-10 millimeter laboratory experiments when extrapolated. To reconcile these models, a new model has been developed based on the JPL Catalog. The intensities of spectral lines associated with inelastic transitions (see Figure 3.1), are sufficient to describe the 2-4 millimeter-wavelength absorption of H_2SO_4 vapor, but the elastic collision line intensities are too low to permit a match with the data of Kolodner and Steffes and the new 7-10 millimeter-wavelength results [41]. Following the approach of Hoffman et al. [77], the intensities of the elastic collisional lines can be scaled to match the centimeter-wavelength H_2SO_4 vapor measurements. The free parameter categories used to fit the full model of H_2SO_4 vapor absorption to the laboratory data are given in Table 3.4.

Table 3.4: Free parameters used for model fitting

Parameter	Notation
$\gamma_{H_2SO_4}$	H_2SO_4 self-broadening linewidth
γ_{H_2O}	H_2SO_4-H_2O pressure-broadening linewidth
γ_{SO_3}	H_2SO_4-SO_3 pressure-broadening linewidth
γ_{CO_2}	H_2SO_4-CO_2 pressure-broadening linewidth
m	Linewidth temperature dependence
D_j	Line intensity scale factor
s_e	Selection parameter for elastic lines

With the exception of the s_e selection parameter, all of the parameters in Table 3.4 likely vary for each spectral line. To make the determination of these free parameters more computationally tractable, seven sets of free parameters were investigated, as shown in Table 3.5. The indices i and e represent inelastic and elastic collisional lines, respectively.

These cases essentially divide the lines in the H_2SO_4 spectrum into groups and assume equal scaling and line-broadening parameters values within these groups. Nine selection criteria for spectral line modification are considered, as described in Table 3.7. The selec-

Table 3.5: Investigated free parameter combinations

Case	Total Free Parameters	Description
1	8	$\gamma_{H_2SO_4}, \gamma_{CO_2}, \gamma_{H_2O}, \gamma_{SO_3}, m, D_i, D_e$
2	12	$\gamma^i_{H_2SO_4}, \gamma^i_{CO_2}, \gamma^i_{H_2O}, \gamma^i_{SO_3}, m_i, \gamma^e_{H_2SO_4}, \gamma^e_{CO_2}, \gamma^e_{H_2O}, \gamma^e_{SO_3}, m_e, D_i, D_e$
3	14	$\gamma^i_{H_2SO_4}, \gamma^i_{CO_2}, \gamma^i_{H_2O}, \gamma^i_{SO_3}, m_i, \gamma^e_{H_2SO_4}, \gamma^e_{CO_2}, \gamma^e_{H_2O}, \gamma^e_{SO_3}, m_e, D_i, D_{e,1}, D_{e,2}, s_{e,1}$
4	16	$\gamma^i_{H_2SO_4}, \gamma^i_{CO_2}, \gamma^i_{H_2O}, \gamma^i_{SO_3}, m_i, \gamma^e_{H_2SO_4}, \gamma^e_{CO_2}, \gamma^e_{H_2O}, \gamma^e_{SO_3}, m_e, D_i, D_{e,1}, D_{e,2}, D_{e,3}, s_{e,1}, s_{e,2}$
5	18	$\gamma^i_{H_2SO_4}, \gamma^i_{CO_2}, \gamma^i_{H_2O}, \gamma^i_{SO_3}, m_i, \gamma^e_{H_2SO_4}, \gamma^e_{CO_2}, \gamma^e_{H_2O}, \gamma^e_{SO_3}, \gamma^{e,1}_{H_2SO_4}, \gamma^{e,1}_{CO_2}, \gamma^{e,1}_{H_2O}, \gamma^{e,1}_{SO_3}, m_e, D_i, D_e, D_{e,1}, s_{e,1}$
6	24	$\gamma^i_{H_2SO_4}, \gamma^i_{CO_2}, \gamma^i_{H_2O}, \gamma^i_{SO_3}, m_i, \gamma^e_{H_2SO_4}, \gamma^e_{CO_2}, \gamma^e_{H_2O}, \gamma^e_{SO_3}, \gamma^{e,1}_{H_2SO_4}, \gamma^{e,1}_{CO_2}, \gamma^{e,1}_{H_2O}, \gamma^{e,1}_{SO_3}, \gamma^{e,2}_{H_2SO_4}, \gamma^{e,2}_{CO_2}, \gamma^{e,2}_{H_2O}, \gamma^{e,2}_{SO_3}, m_e, D_i, D_e, D_{e,1}, D_{e,2}, s_{e,1}, s_{e,2}$
7	30	$\gamma^i_{H_2SO_4}, \gamma^i_{CO_2}, \gamma^i_{H_2O}, \gamma^i_{SO_3}, m_i, \gamma^e_{H_2SO_4}, \gamma^e_{CO_2}, \gamma^e_{H_2O}, \gamma^e_{SO_3}, \gamma^{e,1}_{H_2SO_4}, \gamma^{e,1}_{CO_2}, \gamma^{e,1}_{H_2O}, \gamma^{e,1}_{SO_3}, \gamma^{e,2}_{H_2SO_4}, \gamma^{e,2}_{CO_2}, \gamma^{e,2}_{H_2O}, \gamma^{e,2}_{SO_3}, \gamma^{e,3}_{H_2SO_4}, \gamma^{e,3}_{CO_2}, \gamma^{e,3}_{H_2O}, \gamma^{e,3}_{SO_3}, m_e, D_i, D_e, D_{e,1}, D_{e,2}, D_{e,3}, s_{e,1}, s_{e,2}, s_{e,3}$

tion parameters s_e govern the selection of a subset of the elastic lines based on the selection criteria. The classes of elastic collisional lines defined by the selection criteria then receive separate treatment depending on the free parameter cases shown in Table 3.5. The division of spectral lines into groups for case seven is shown in Table 3.6 as an example.

Table 3.6: Division of elastic line spectrum into groups for Case 7. The parameter x depends on the choice of selection criteria

Group Number	Line Selection
I	$x < s_{e,1}$
II	$x > s_{e,2}$
III	$s_{e,3} < x < s_{e,2}$
IV	All other elastic lines

The free parameter values are determined by minimizing a weighted and regularized cost function in the form of Equation 3.16. The regularization term C_r is the same as that used to fit the 2-4 millimeter-wavelength data, and the weighting term is determined using

Table 3.7: Investigated elastic transition selection criteria

Number	Selection Criteria (SC)
1	Frequency $\nu_{0,j}$
2	Line intensity I_o
3	Quantum number J
4	Upper state quantum number K_-
5	Upper state quantum number K_-
6	Lower state quantum number K_+
7	Lower state quantum number K_+
8	Transition magnitude $|K_+^1 - K_-^2|$
9	Transition magnitude $|K_-^1 - K_+^2|$

Equation 3.17. The frequency, temperature, pressure, and concentration bins used for the weighting are shown in Tables 3.8 and 3.9.

Table 3.8: H_2SO_4 vapor absorption measurement count by frequency and temperature

Frequency range (GHz)	f_{count}	Temperature Range (K)	T_{count}
$1 \leq f < 10$	13	$T < 540$	49
$10 \leq f < 25$	10	$540 \leq T < 560$	205
$25 \leq f < 34$	12	$560 \leq T < 575$	138
$34 \leq f < 45$	160	$T \geq 575$	33
$70 \leq f < 85$	64		
$85 \leq f < 95$	56		
$95 \leq f < 105$	58		
$105 \leq f < 115$	19		
$115 \leq f < 135$	24		
$f \geq 135$	9		

Given the number of free parameters considered, the results of cost function minimization using quasi-Newton methods such as the L-BFGS-B algorithm are highly dependent on the initial guess provided to the algorithm. To determine the global minimum for the cost function, the Differential Evolution (DE) algorithm was used as implemented in the Scipy package [78]. This algorithm doesn't rely on gradient evaluations, but instead it iteratively generates new guesses based on mutating an initial population, discarding solutions

Table 3.9: H_2SO_4 vapor absorption measurement count by mixure pressure and H_2SO_4 vapor concentration

Pressure range (bars)	P_{count}	Concentration range (%)	C_{count}
$p < 0.5$	83	$C < 1$	220
$0.5 \leq p < 1.5$	117	$1 \leq C < 10$	144
$1.5 \leq p < 2.5$	135	$C \geq 10$	61
$2.5 \leq p$	90		

that perform poorly. The initial population is generated to span the full parameter space specified by the free parameter bounds. After a minimum solution is determined using the DE method, an L-BFGS-B step is performed to refine the result. For each evaluation of the cost function, the value of the function and the corresponding free parameters are recorded to estimate free parameter uncertainties. To reduce the computational burden of fitting a model using the full 44,221-line H_2SO_4 catalog with up to 30 free parameters to the 425 laboratory measurements, population updates were computed in parallel using the PACE cluster at Georgia Tech.

From the models determined for all cases and selection criteria, the final model selected uses Case 7 free parameters and selects groups of elastic transition lines by frequency (Selection Criteria 1). Figures 3.2-3.9 show comparisons of the models considered for all free parameter cases and selection criteria for the microwave and millimeter-wavelength datasets, respectively. For these plots, the measured absorption from the laboratory data is normalized by the mole fraction of H_2SO_4 vapor present during the measurement. A temperature correction scaling is also applied to normalize the results to a measurement temperature of 550 K. To select the final model from all of the cases and selection criteria considered, the models were assessed based on their ability to minimize the cost function overall. Figure 3.10 shows the obtained value of the cost function for Cases 3-7, demonstrating that the selected model was able to achieve the best fit.
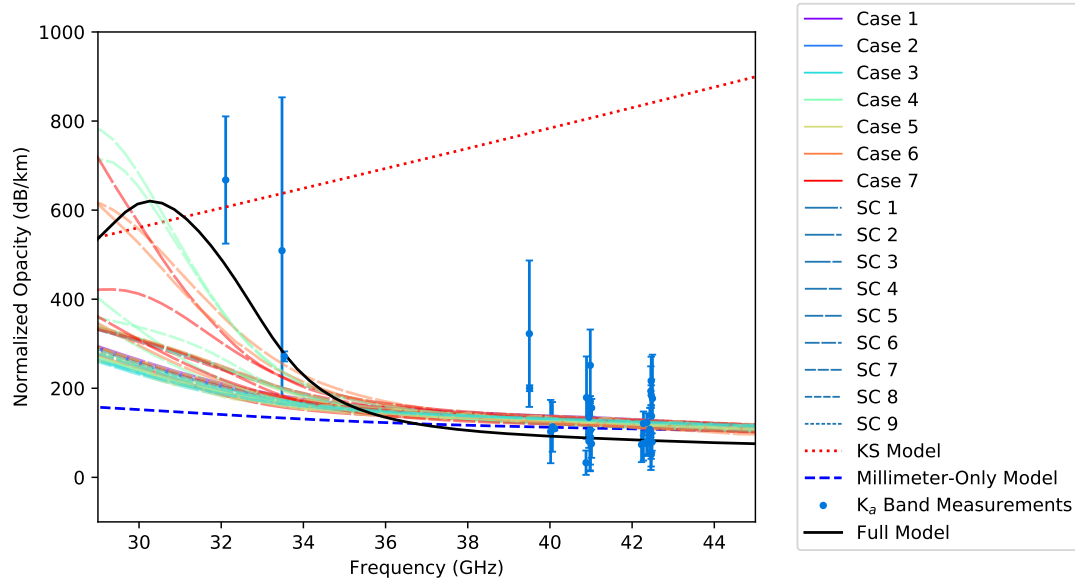
Figure 3.2: K$_a$ Band laboratory data taken at pressures of 0.15 bar normalized by H$_2$SO$_4$ mole fraction and temperature compared to the microwave model of Kolodner and Steffes (KS) [41], the millimeter-only model, best-fit models for all free parameter cases and selection criteria (SC), and the selected full band model (Case 7, SC 1).
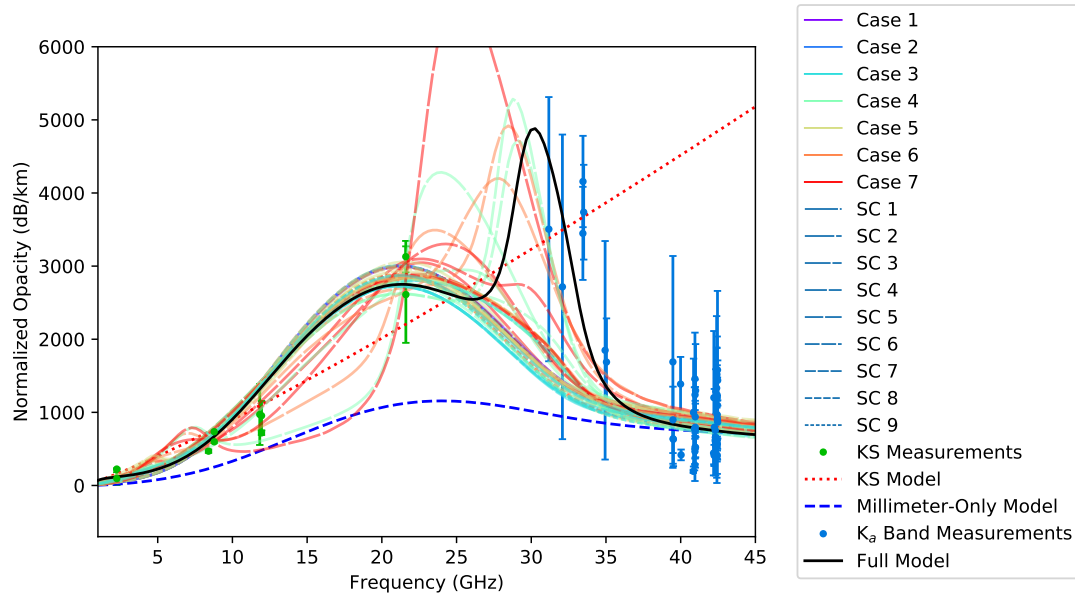
Figure 3.3: Microwave and K$_a$ Band laboratory data taken near pressures of 1 bar normalized by H$_2$SO$_4$ mole fraction and temperature compared to the microwave model of Kolodner and Steffes (KS) [41], the millimeter-only model, best-fit models for all free parameter cases and selection criteria (SC), and the selected full band model (Case 7, SC 1).
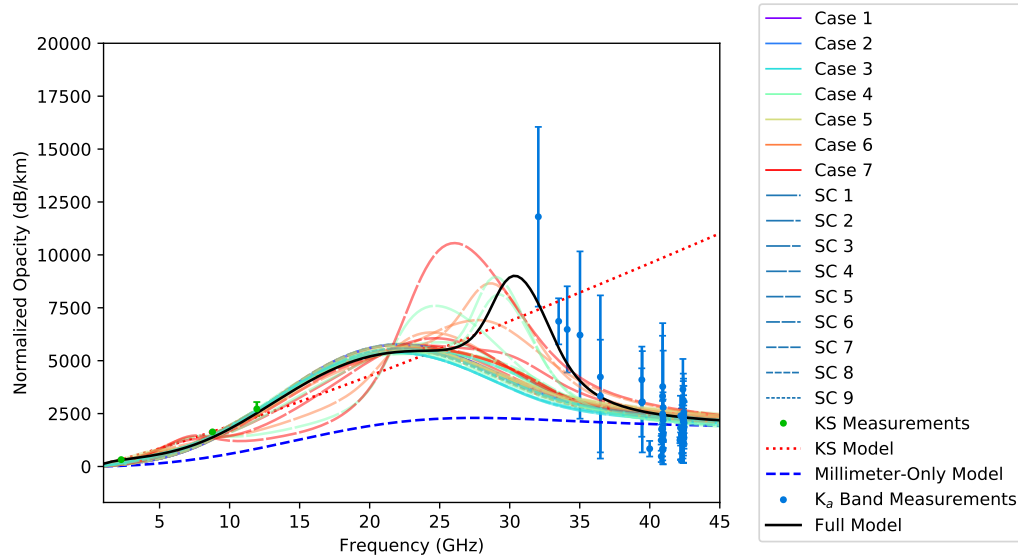
Figure 3.4: Microwave and K$_a$ Band laboratory data taken near pressures of 2 bar normalized by H$_2$SO$_4$ mole fraction and temperature compared to the microwave model of Kolodner and Steffes (KS) [41], the millimeter-only model, best-fit models for all free parameter cases and selection criteria (SC), and the selected full band model (Case 7, SC 1).
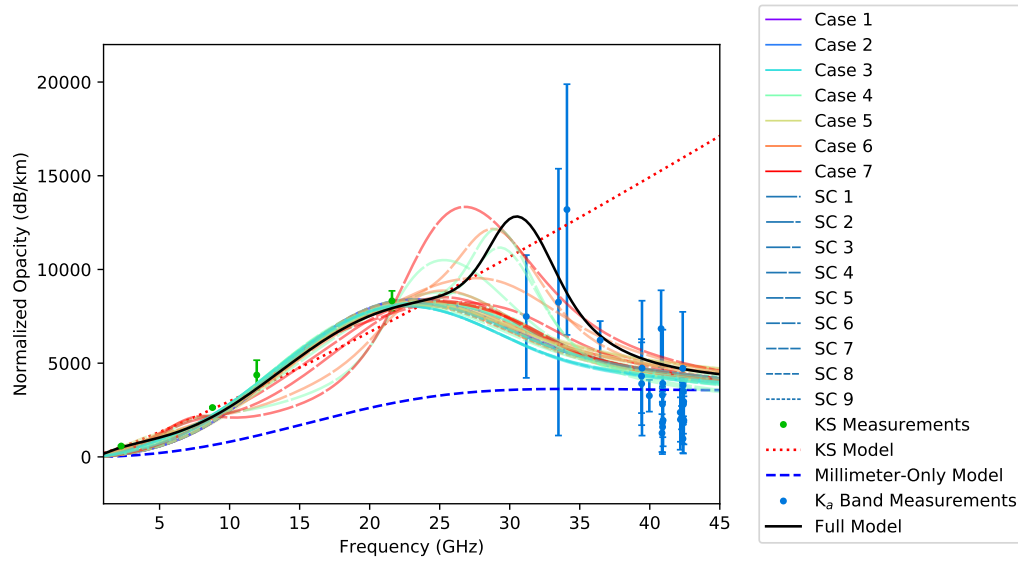
Figure 3.5: Microwave and K$_a$ Band laboratory data taken near pressures of 3 bar normalized by H$_2$SO$_4$ mole fraction and temperature compared to the microwave model of Kolodner and Steffes (KS) [41], the millimeter-only model, best-fit models for all free parameter cases and selection criteria (SC), and the selected full band model (Case 7, SC 1).
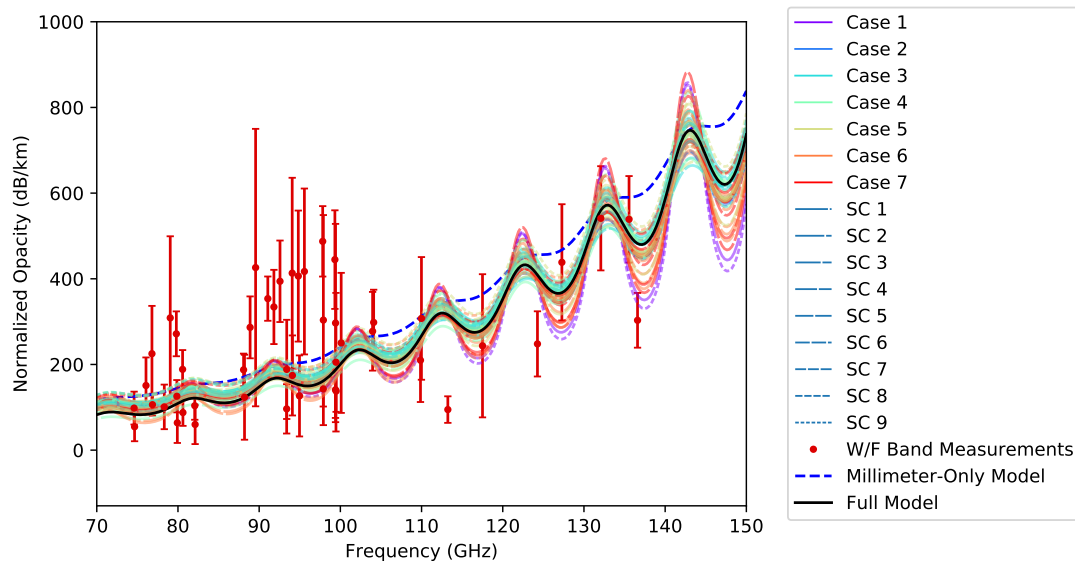
Figure 3.6: W and F Band laboratory data taken at pressures of 0.15 bar normalized by H_2SO_4 mole fraction and temperature compared to the millimeter-only model, best-fit models for all free parameter cases and selection criteria (SC), and the selected full band model (Case 7, SC 1).
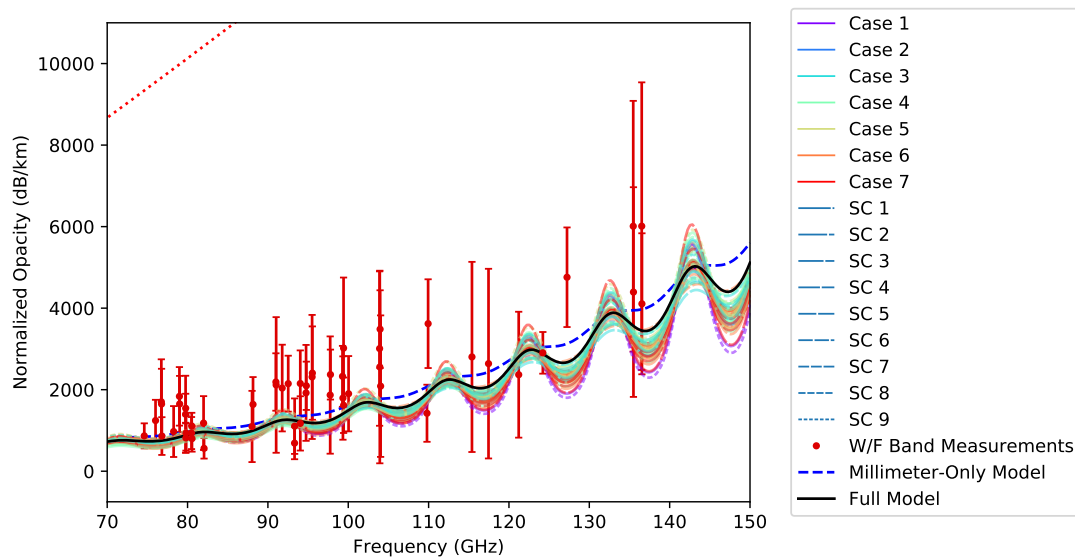
Figure 3.7: W and F Band laboratory data taken near pressures of 1 bar normalized by H_2SO_4 mole fraction and temperaturecompared to the millimeter-only model, best-fit models for all free parameter cases and selection criteria (SC), and the selected full band model (Case 7, SC 1).
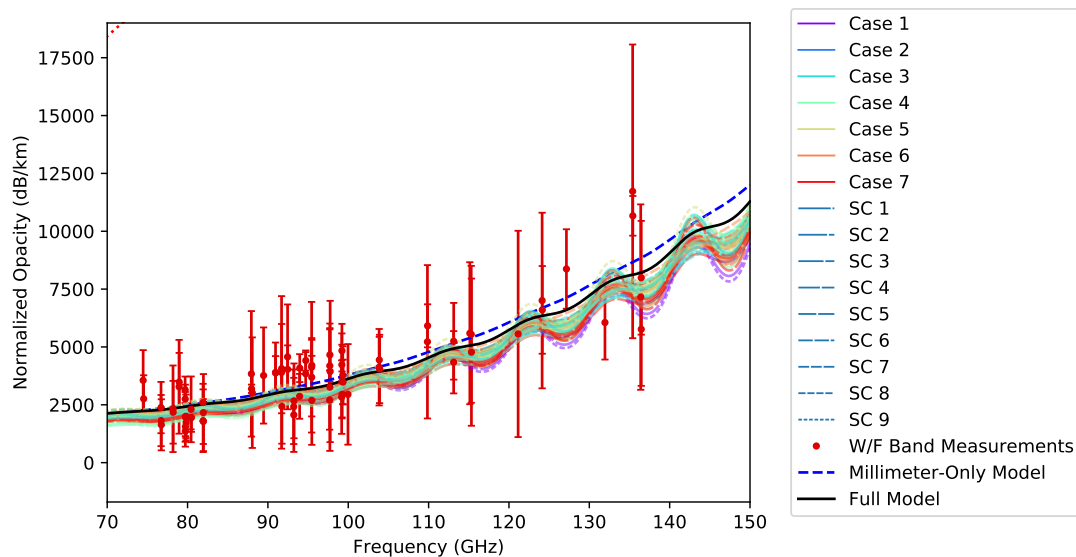
Figure 3.8: W and F Band laboratory data taken near pressures of 2 bar normalized by H_2SO_4 mole fraction and temperature compared to the millimeter-only model, best-fit models for all free parameter cases and selection criteria (SC), and the selected full band model (Case 7, SC 1).
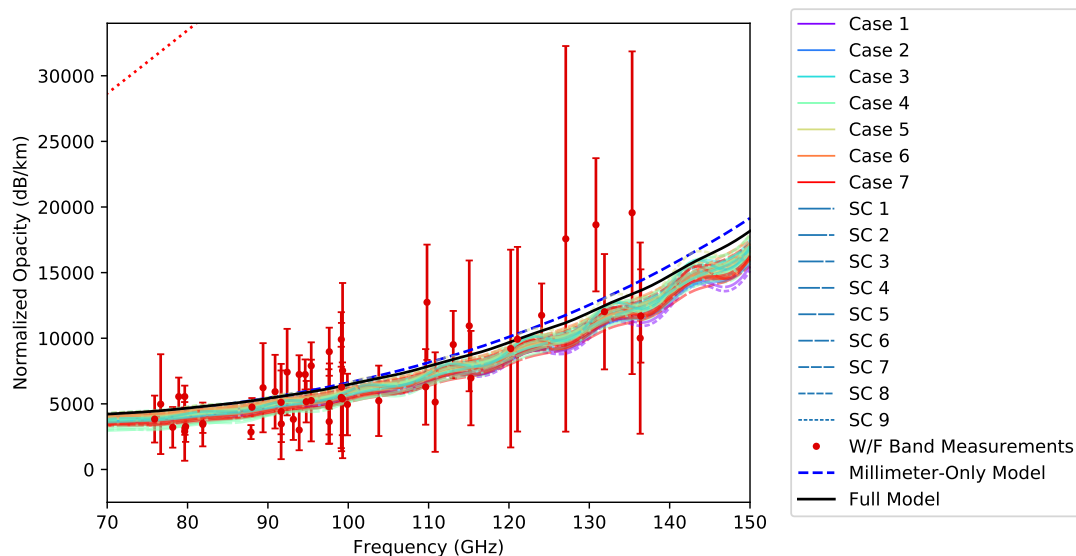
Figure 3.9: W and F Band laboratory data taken near pressures of 3 bar normalized by H_2SO_4 mole fraction and temperature compared to the millimeter-only model, best-fit models for all free parameter cases and selection criteria (SC), and the selected full band model (Case 7, SC 1).
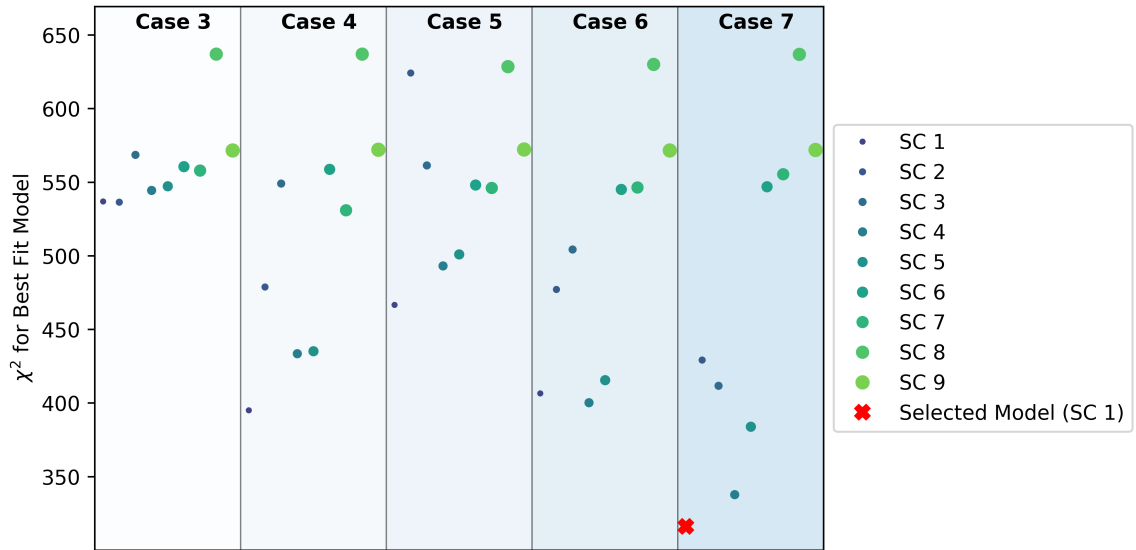
Figure 3.10: Obtained cost function value for all models using Case 3-7 free parameters.

The resulting models were also implemented in a microwave radiative transfer model for the Venus atmosphere (described in detail in the following chapter). Using a nominal H_2SO_4 vapor abundance in the Venus atmosphere, the models were assessed for their ability to match the disk-averaged brightness temperature of Venus as determined by the model. Figure 3.11 shows the disk-averaged brightness temperatures obtained by the model as compared to accurate microwave measurements made using the Very Large Array by Perley and Butler in 2012 and a millimeter-wavelength single-dish measurement using the Millimeter Wave Observatory by Ulich [79, 80]. The difference between these values is shown in Figure 3.12. While the selected model does not obtain the minimum brightness temperature difference for each frequency, it is among the top performers for the majority of the observations.

The values of the free parameters for the full band model are shown in Tables 3.10 and 3.11. The values of the errors for each parameter are determined by selecting a subset of the population results from the DE algorithm that are able to achieve a cost function value within 50% of the best fit value. The standard deviation of the resulting distribution for each free parameter is taken as the model uncertainty. It is important to note, however, that
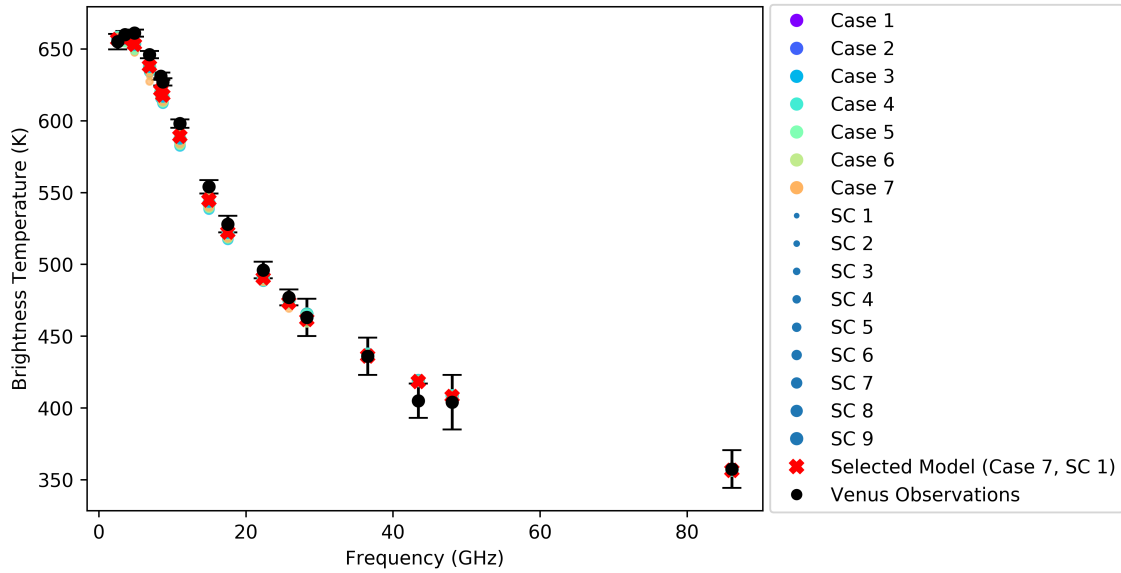
Figure 3.11: Observed disk-averaged Venus brightness temperature [79] and modeled values for each considered H_2SO_4 vapor model for a nominal Venus atmosphere. The temperature and pressure profiles are taken from the low-latitude Venus International Reference Atmosphere model, the Mariner 10 radio occultation profile for H_2SO_4 vapor is assumed, and a uniform deep atmosphere SO_2 abundance of 50 ppm is specified.
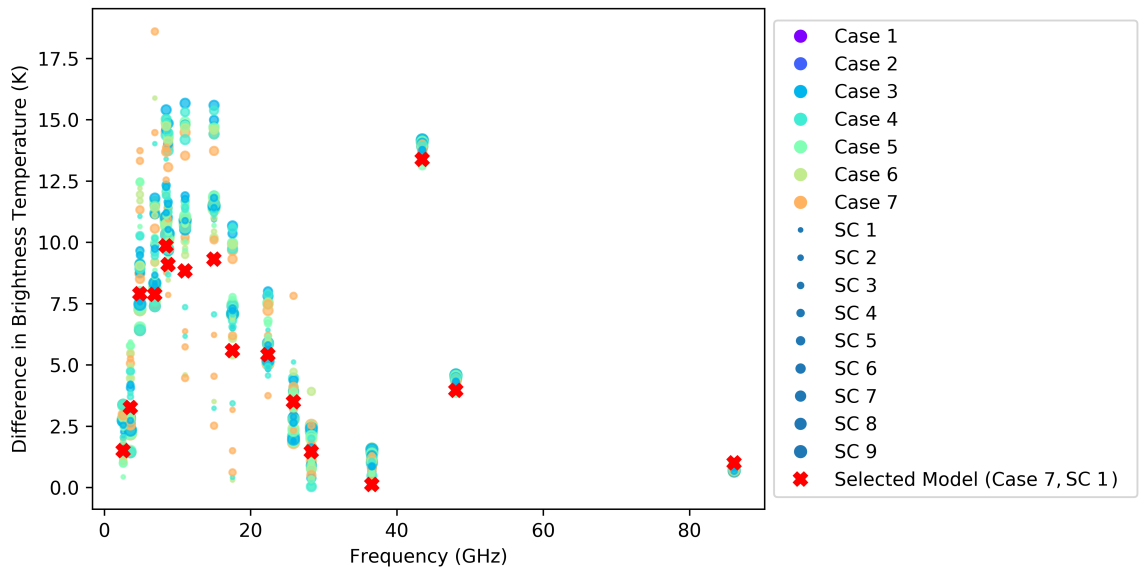
Figure 3.12: Difference between observed disk-averaged Venus brightness temperature [79] and modeled values for each considered H_2SO_4 vapor model. The temperature and pressure profiles are taken from the low-latitude Venus International Reference Atmosphere model, the Mariner 10 radio occultation profile for H_2SO_4 vapor is assumed, and a uniform deep atmosphere SO_2 abundance of 50 ppm is specified.

57

the distributions of these free parameters are not entirely independent. Figure 3.13 shows

the correlation matrix for each of the free parameters derived from the subpopulation

Table 3.10: Scaling parameters for H_2SO_4 vapor model

Parameter	Value
D_i	1.041 ± 0.02
D_e	0.922 ± 0.01
$D_{s,1}$	19.146 ± 4.01
$D_{s,2}$	1.617 ± 0.61
$D_{s,3}$	18.683 ± 3.57
$s_{e,1}$	1.079 GHz ± 0.37
$s_{e,2}$	32.993 GHz ± 2.15
$s_{e,3}$	29.049 GHz ± 2.18

Table 3.11: Line broadening parameters for H_2SO_4 vapor model

Parameter	j=H_2SO_4	j=H_2O	j=SO_3	j=CO_2
γ_j^i (MHz/torr)	83.55 ± 3.66	60.24 ± 19.09	11.52 ± 1.53	4.13 ± 0.85
γ_j^e (MHz/torr)	12.20 ± 8.25	8.02 ± 4.69	6.01 ± 1.92	3.75 ± 0.51
$\gamma_j^{e,1}$ (MHz/torr)	18.84 ± 7.75	12.15 ± 6.53	7.23 ± 1.97	1.02 ± 0.25
$\gamma_j^{e,2}$ (MHz/torr)	89.52 ± 6.34	56.33 ± 8.75	12.05 ± 1.64	9.79 ± 0.78
$\gamma_j^{e,3}$ (MHz/torr)	37.38 ± 10.24	23.84 ± 3.21	6.06 ± 1.02	1.15 ± 0.6
m_i	0.83 ± 0.06	0.83 ± 0.06	0.83 ± 0.06	0.83 ± 0.06
m_e	1 ± 0.08	1 ± 0.08	1 ± 0.08	1 ± 0.08

Figures 3.14-3.24 show the full model superimposed over all models from the subpop-

ulation for the measurements of Kolodner and Steffes and the W, F, and K_a Band measure-

ments. The percent fit for the H_2SO_4 vapor absorption model of Kolodner and Steffes, the

millimeter-only model, and the full model were evaluated by identifying the total number

of laboratory measurements for which the model predicted absorption fell within the 2σ

uncertainty of the absorption measurements. The results are shown in Table 3.12.
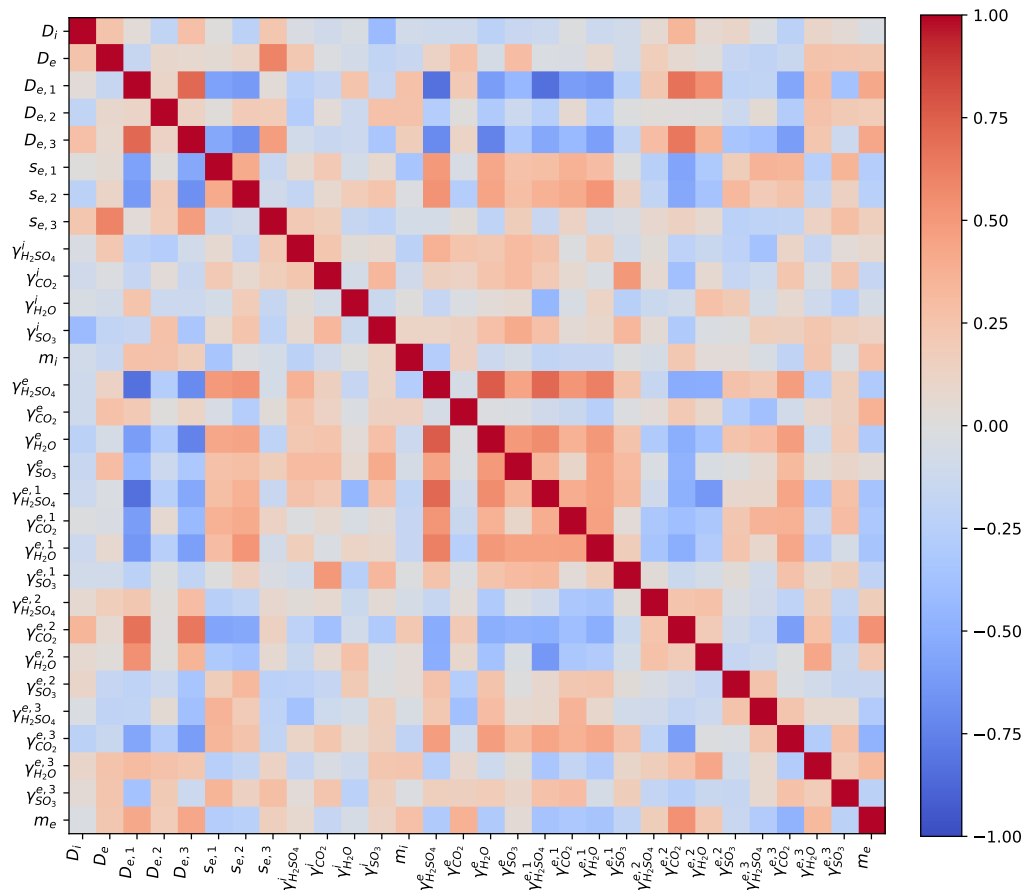
Figure 3.13: Correlation between parameters for the subpopulation of models acheiving within 50 % of the best fit value.
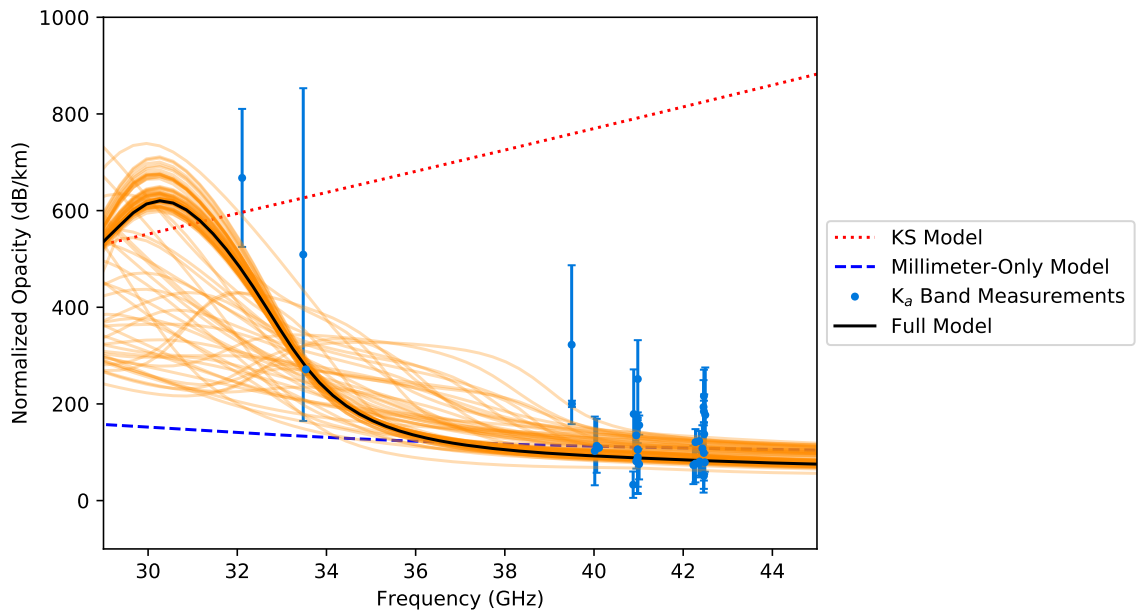
Figure 3.14: K_a Band laboratory data taken at pressures of 0.15 bar normalized by H_2SO_4 mole fraction and temperature compared to the microwave model of Kolodner and Steffes (KS) [41], the millimeter-only model, and the full band model.
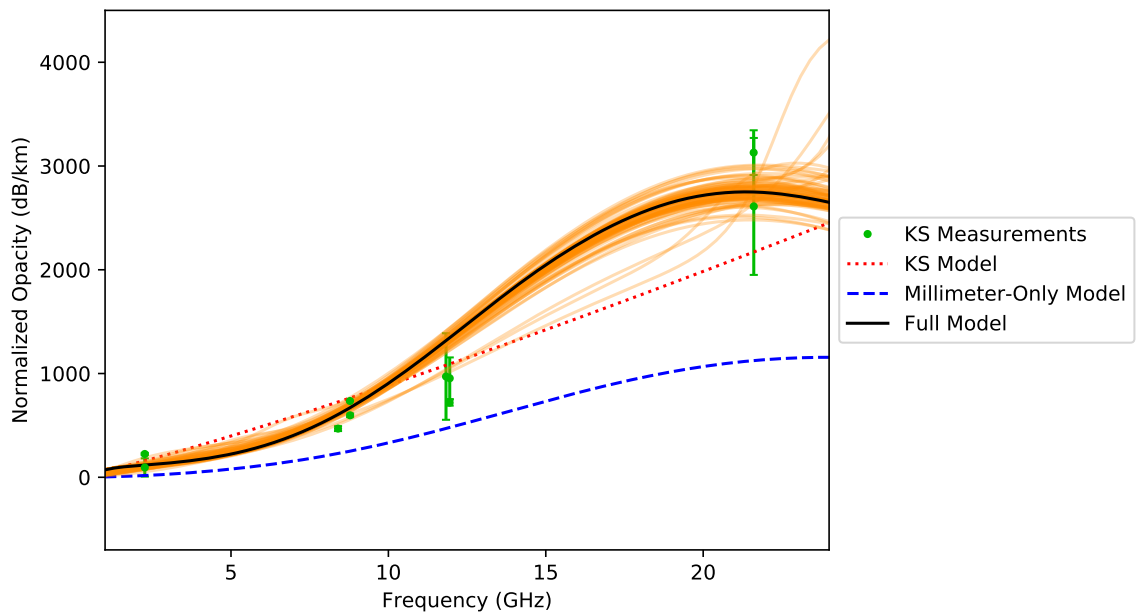
Figure 3.15: Microwave laboratory data taken near pressures of 1 bar normalized by H_2SO_4 mole fraction and temperature compared to the microwave model of Kolodner and Steffes (KS) [41], the millimeter-only model, and the full band model.
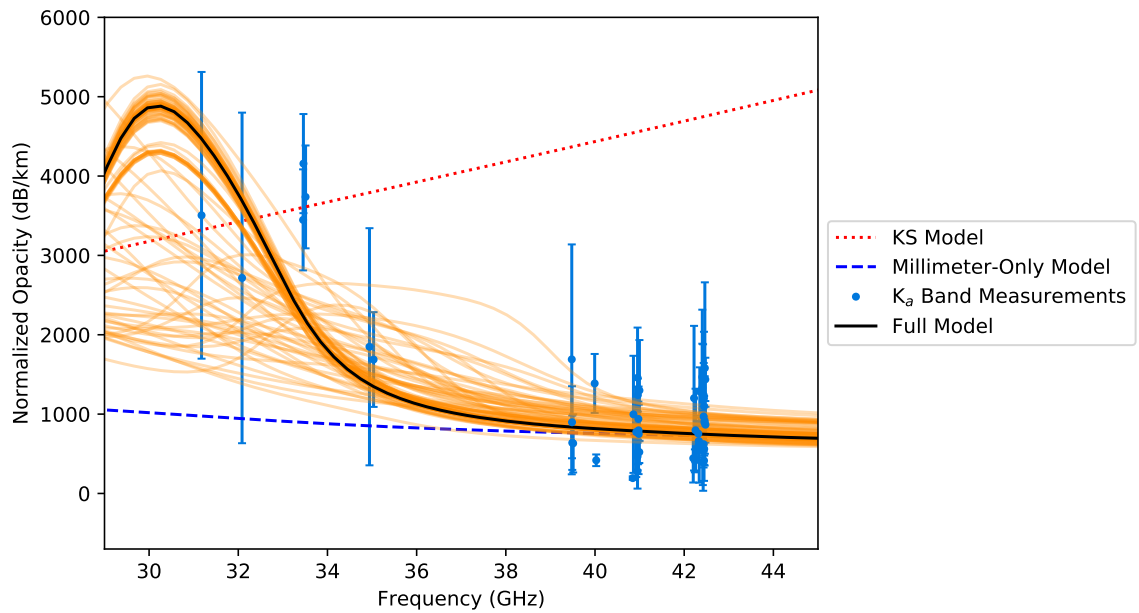
Figure 3.16: K_a Band laboratory data taken near pressures of 1 bar normalized by H_2SO_4 mole fraction and temperature compared to the microwave model of Kolodner and Steffes (KS) [41], the millimeter-only model, and the full band model.
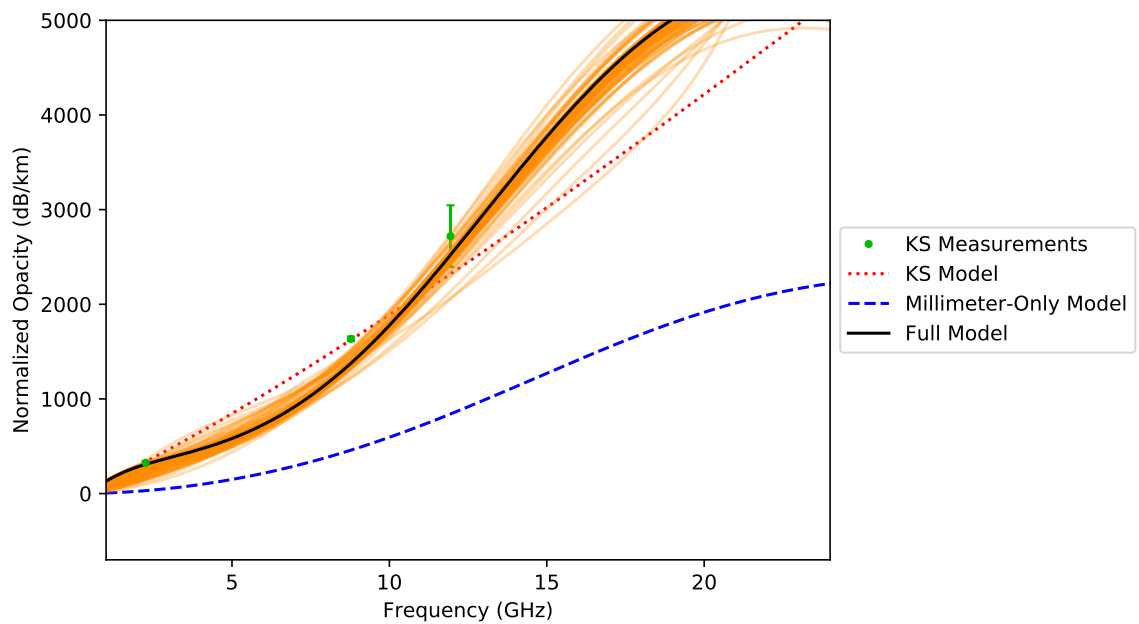
Figure 3.17: Microwave laboratory data taken near pressures of 2 bar normalized by H_2SO_4 mole fraction and temperature compared to the microwave model of Kolodner and Steffes (KS) [41], the millimeter-only model, and the full band model.
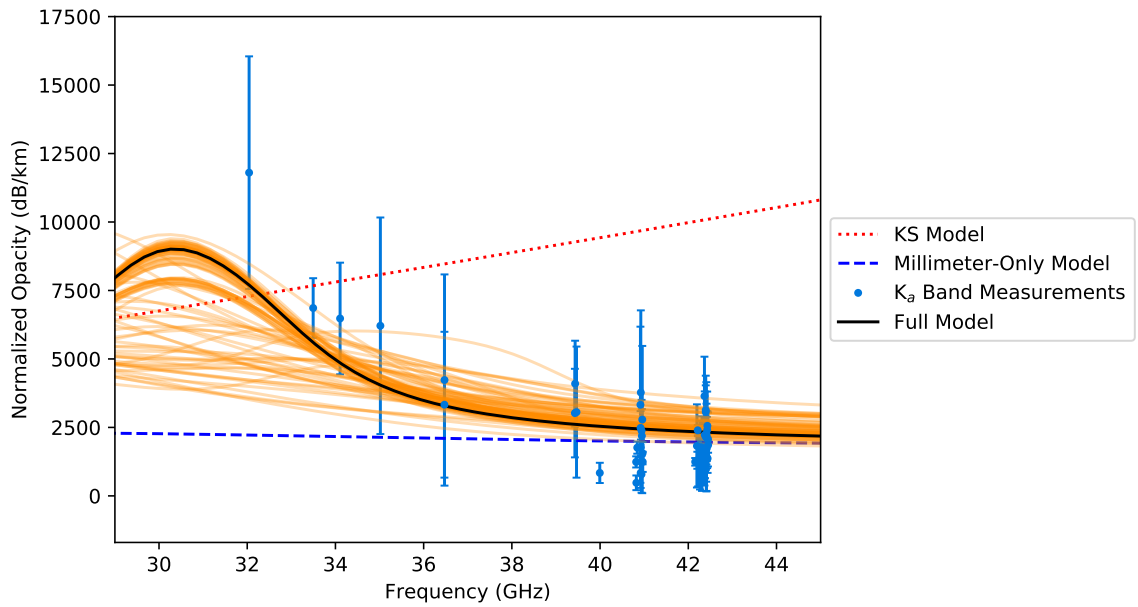
Figure 3.18: K_a Band laboratory data taken near pressures of 2 bar normalized by H_2SO_4 mole fraction and temperature compared to the microwave model of Kolodner and Steffes (KS) [41], the millimeter-only model, and the full band model.
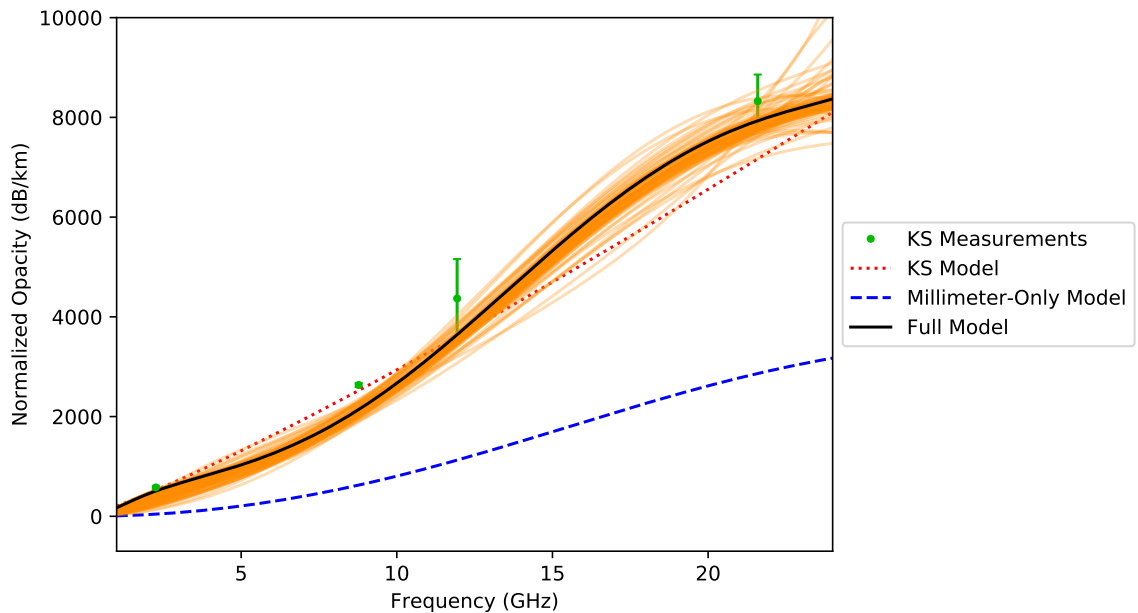
Figure 3.19: Microwave laboratory data taken near pressures of 3 bar normalized by H_2SO_4 mole fraction and temperature compared to the microwave model of Kolodner and Steffes (KS) [41], the millimeter-only model, and the full band model.
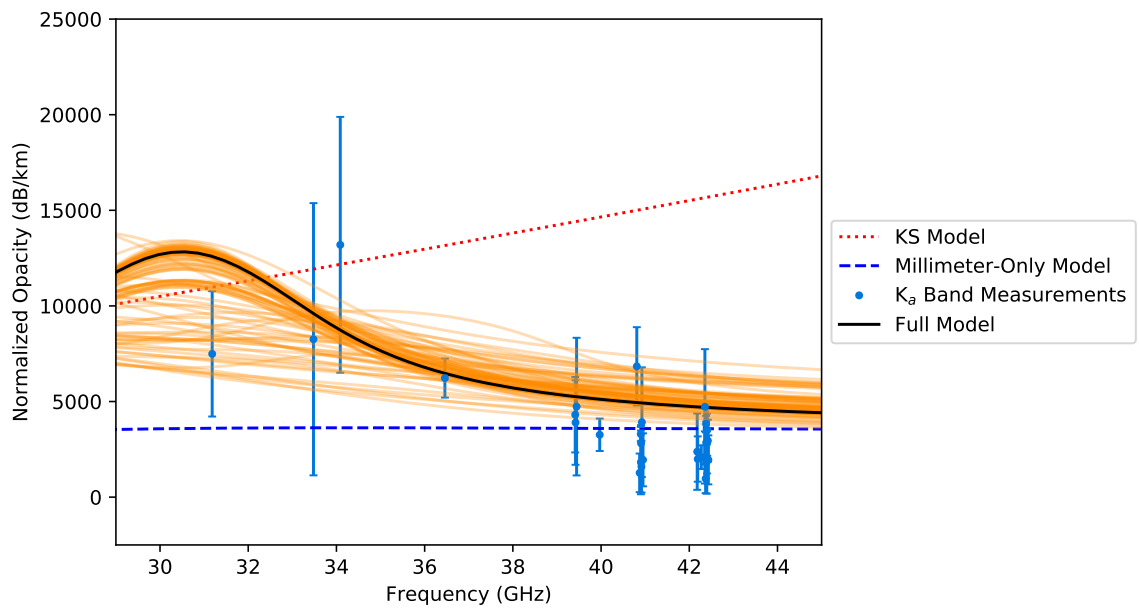
Figure 3.20: K_a Band laboratory data taken near pressures of 3 bar normalized by H_2SO_4 mole fraction and temperature compared to the microwave model of Kolodner and Steffes (KS) [41], the millimeter-only model, and the full band model.
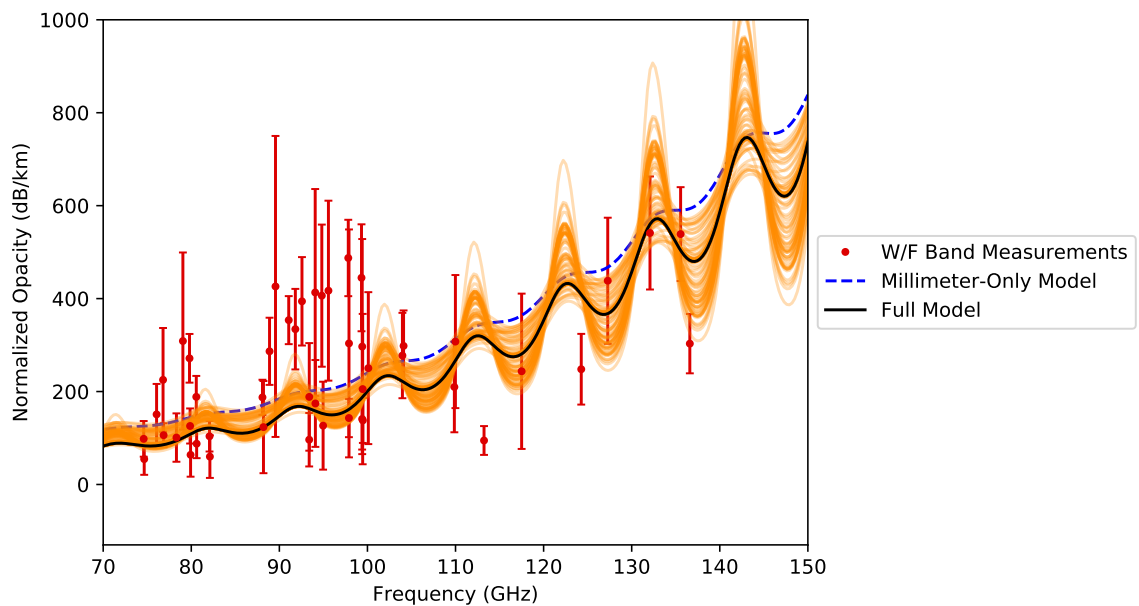
Figure 3.21: W and F Band laboratory data taken at pressures of 0.15 bar normalized by H_2SO_4 mole fraction and temperature compared to the millimeter-only model and the full band model.
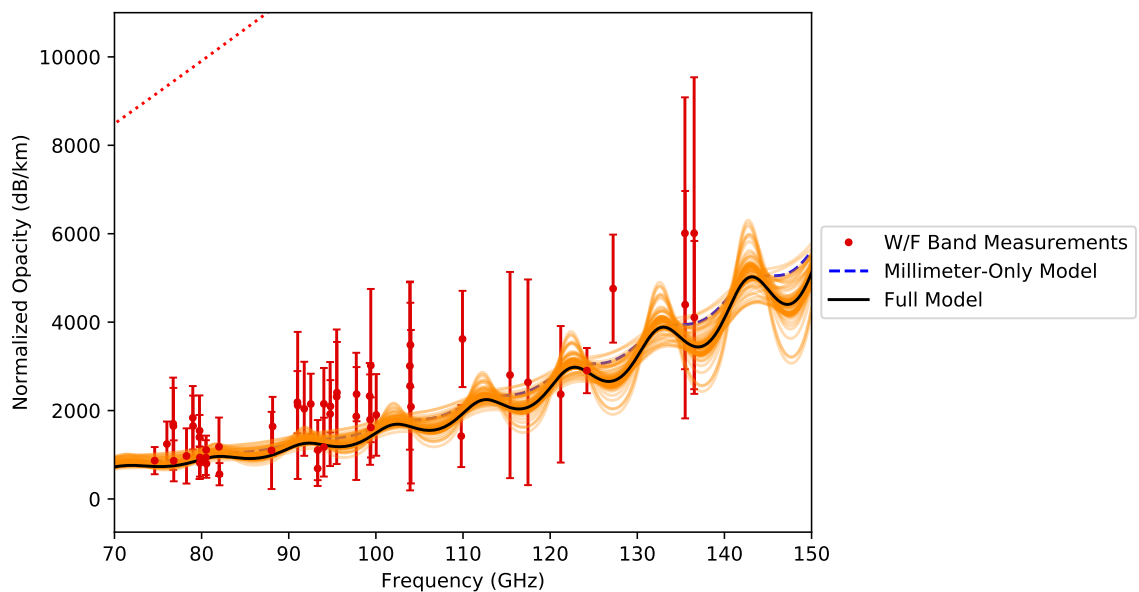
Figure 3.22: W and F Band laboratory data taken near pressures of 1 bar normalized by H_2SO_4 mole fraction and temperature compared to the millimeter-only model, and the full band model.
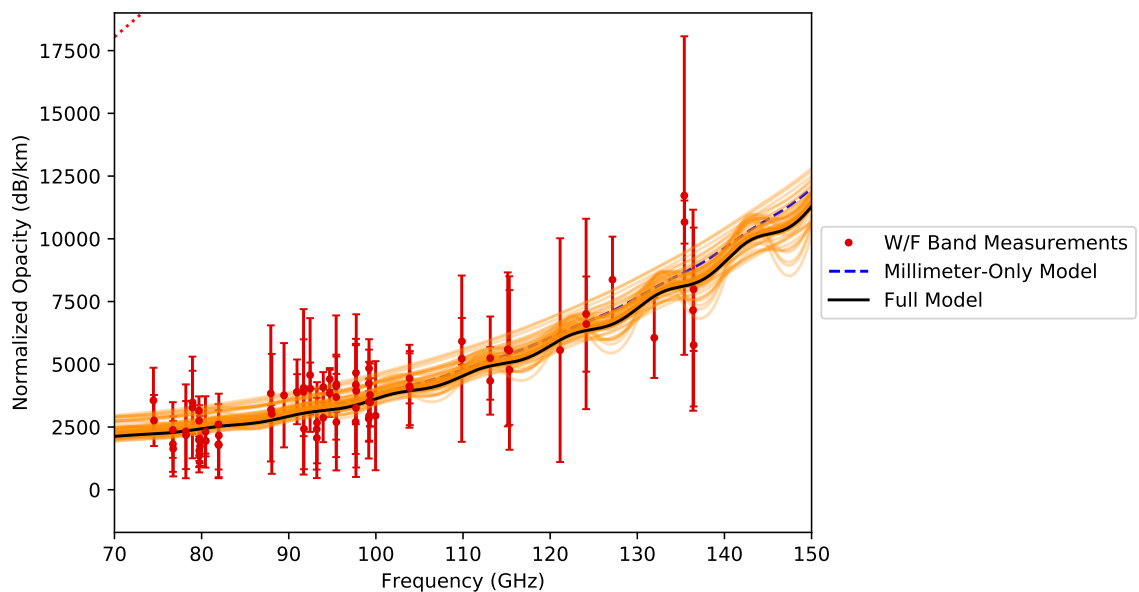
Figure 3.23: W and F Band laboratory data taken near pressures of 2 bar normalized by H_2SO_4 mole fraction and temperature compared to the millimeter-only model and the full band model.
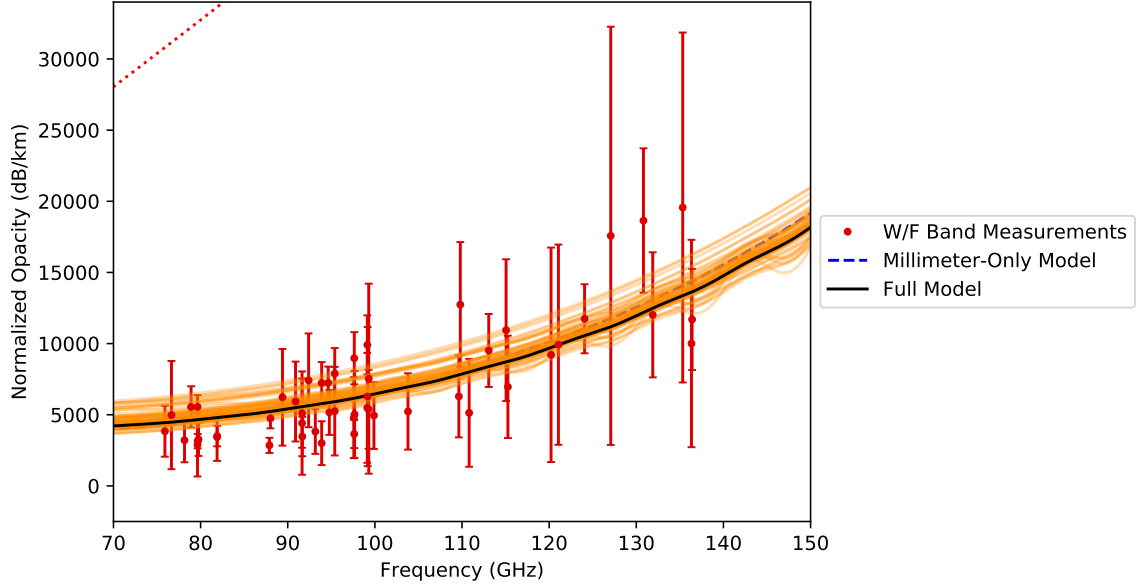
Figure 3.24: W and F Band laboratory data taken near pressures of 3 bar normalized by H_2SO_4 mole fraction and temperature compared to the millimeter-only model and the full band model.

$$\mathbf{1}_{model}(\alpha) = \begin{cases} 1 & : |\alpha_{measured} - \alpha_{model}| \leq \sqrt{Err_{2\sigma}^2} \\ 0 & : |\alpha_{measured} - \alpha_{model}| > \sqrt{Err_{2\sigma}^2} \end{cases} \tag{3.19}$$

$$\text{Percent Fit} = \frac{\sum_{i=1}^{N} \mathbf{1}_{model}(\alpha)}{N} \times 100\% \tag{3.20}$$

Table 3.12: Fit percent for all models over different measurement bands

Model	1-10 GHz	10-25 GHz	25-40 GHz	40-50 GHz	> 50 GHz
Kolodner and Steffes [41]	23%	50%	38%	0%	0%
Millimeter-only	0%	0%	49%	60%	83%
Full model	23%	50%	63%	49%	79%

The derived model performs comparably to the Kolodner and Steffes model and the millimeter-only model in their respective measurement bands while also providing a better fit to the K_a Band measurements. The three models are shown in Figures 3.25-3.28. To

65

achieve this, however, a sizable discontinuity in the predicted opacity occurs in the 25-30 GHz portion of the model spectrum. Future laboratory measurements are needed to target this frequency band to provide further bounds on the model presented here.

3.4 Refractivity of H_2SO_4 vapor

The number density-normalized refractivity of H_2SO_4 vapor has been determined for representative frequencies within each of the measurement bands. These results are shown in Table 3.13 with the results derived from Kolodner and Steffes at S Band [41].

Table 3.13: Normalized refractivity of H_2SO_4 vapor at several frequencies

Center Frequency	Normalized Refractivity (cm^3/molecule)
2.26 GHz [41]	$(3.086 \pm 0.272) \times 10^{-16}$
42 GHz	$(1.405 \pm 0.291) \times 10^{-15}$
120 GHz	$(1.150 \pm 0.263) \times 10^{-15}$
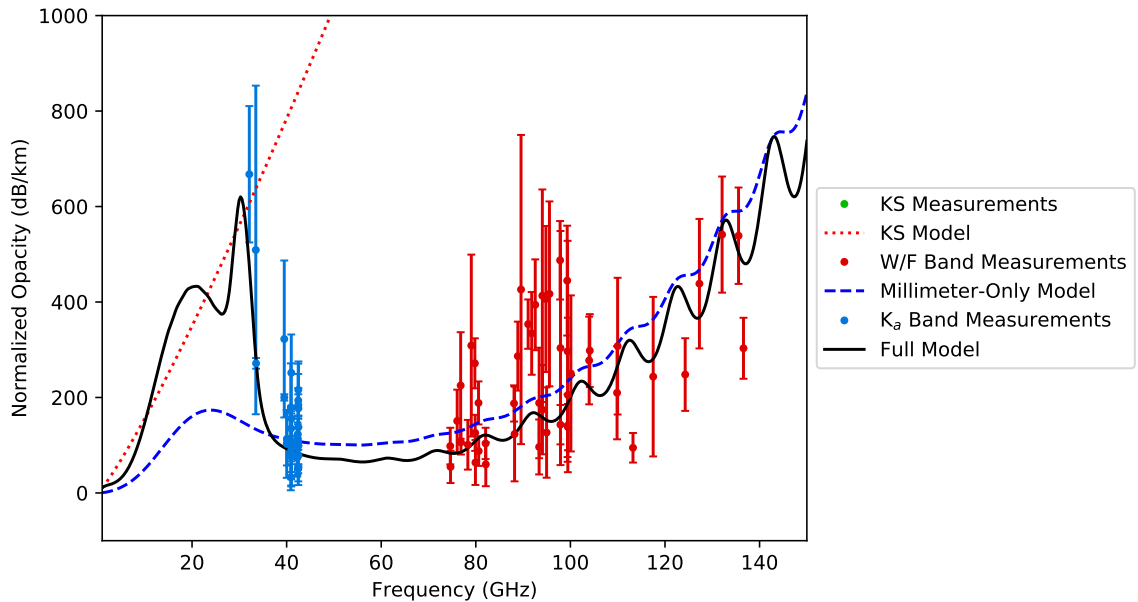
Figure 3.25: All H_2SO_4 laboratory data taken at pressures of 0.15 bar normalized by H_2SO_4 mole fraction and temperature compared to opacity models.
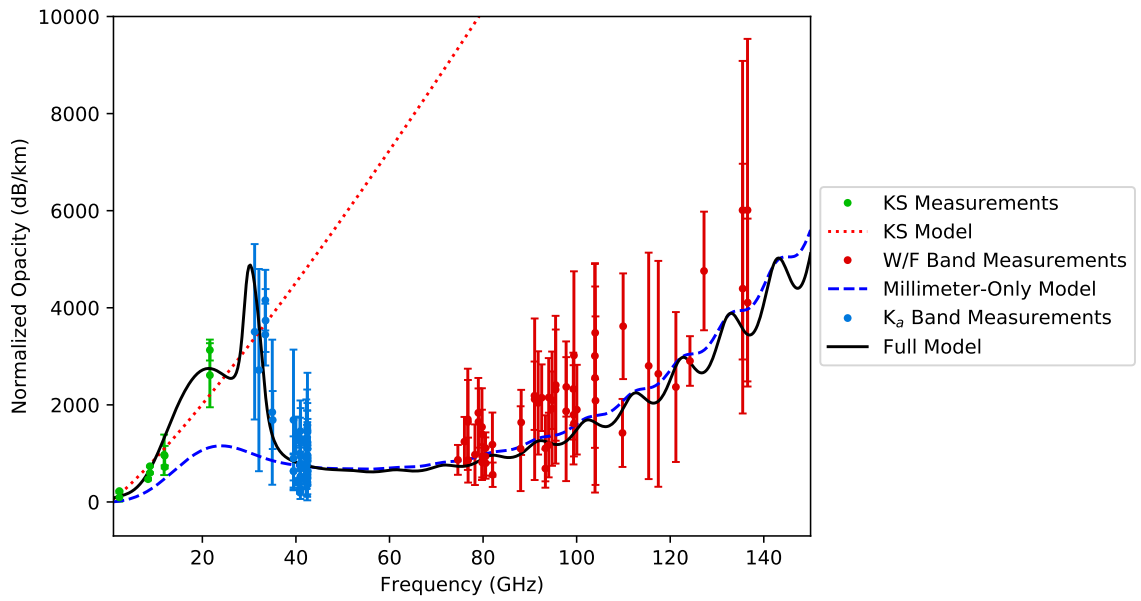
Figure 3.26: All H_2SO_4 laboratory data taken near pressures of 1 bar normalized by H_2SO_4 mole fraction and temperature compared to opacity models.
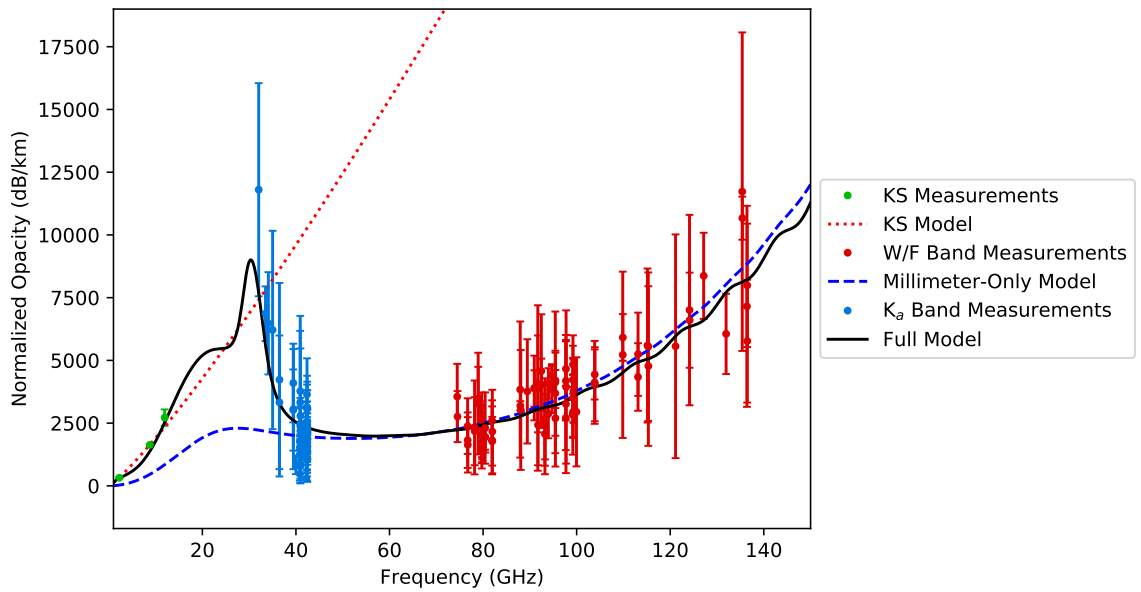
Figure 3.27: All H_2SO_4 laboratory data taken near pressures of 2 bar normalized by H_2SO_4 mole fraction and temperature compared to opacity models.
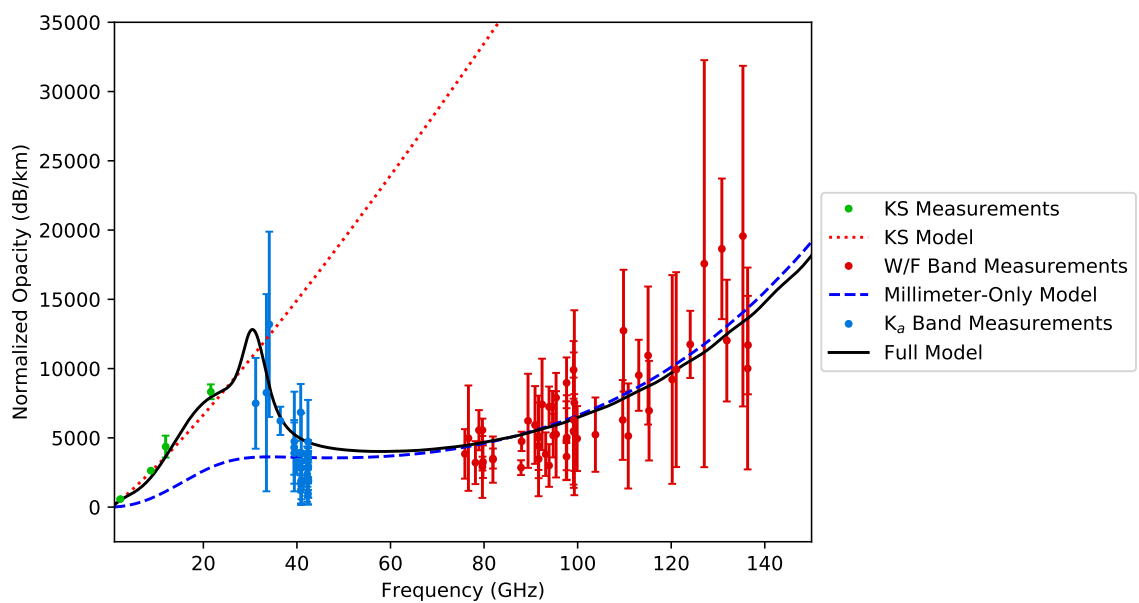
Figure 3.28: All H_2SO_4 laboratory data taken near pressures of 3 bar normalized by H_2SO_4 mole fraction and temperature compared to opacity models.

CHAPTER 4

RADIATIVE TRANSFER MODELING

Microwave radiometer instruments measure the intensity of emitted radiation over a defined bandwidth from a target body. The expected microwave emission intensity of Venus seen by a observer can be modeled using information about the structure and composition of the atmosphere combined with the equations of radiative transfer. The inversion of this model can be used to derive estimates of atmospheric characteristics. In the following sections, a radiative transfer model of the Venus atmosphere is described, discussing both the underlying equations of radiative transfer and the model inputs. Block diagrams illustrating the forward model and its inversion are shown in Figure 4.1.
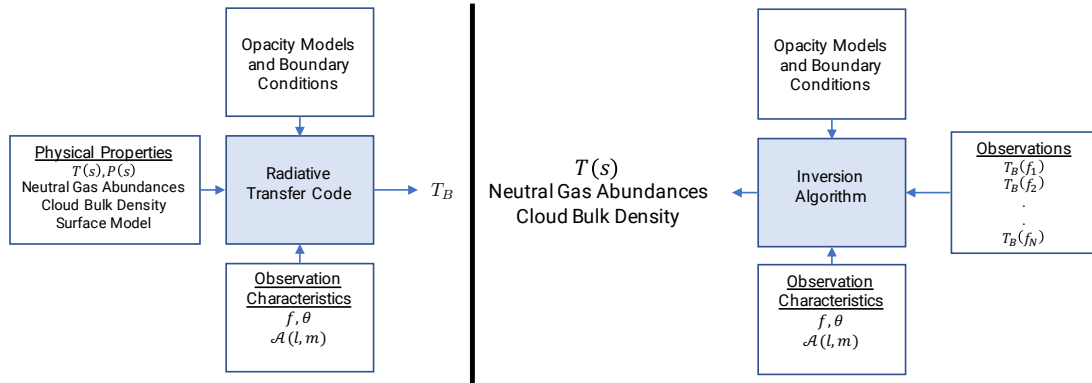
Figure 4.1: The forward model (left) generates a brightness temperature for a given model atmosphere, opacity models, and observation characteristics. The inverse model (right) can be used to estimate the physical properties of the atmosphere from observed brightness temperatures

4.1 Atmospheric Radiative Transfer Equations for Terrestrial Bodies

The emission of electromagnetic radiation from a body in space can be compared to emission from a perfect blackbody, i.e. a body that absorbs and emits at all frequencies. The intensity of emitted radiation B_λ from a blackbody is given by Planck's Law as a function of wavelength λ and the brightness temperature T_B of the blackbody [81]. c is the speed of light, h is Planck's constant, and k_B is Boltzmann's constant.

$$B_\lambda(T) = \frac{2hc^2}{\lambda^5 \left(e^{hc/k_B \lambda T_B} - 1\right)} \tag{4.1}$$

For centimeter and millimeter wavelengths, this intensity can be approximated by the Rayleigh-Jeans distribution.

$$B_\lambda(T) = \frac{2k_B c}{\lambda^4} T_B \tag{4.2}$$

According to Kirchoff's law, the electromagnetic radiation with intensity J_λ emitting from matter is the product of the ideal blackbody radiation at a given temperature and a wavelength-dependent absorption coefficient or absorptivity α. Roughly speaking, Kirchoff's law states that the capability of matter to absorb electromagnetic radiation is equal to its capability to emit radiation under the assumption of local thermodynamic equilibrium.

$$J_\lambda = \alpha B_\lambda(T) \tag{4.3}$$

The equations of atmospheric radiative transfer describe the absorption and emission of electromagnetic radiation through a differential equation. Consider a planetary surface with temperature T_s emitting electromagnetic radiation $I_{\lambda,0}$ in accordance with Equation 4.3. The emissivity of the planetary surface material and Kirchoff's law yield the emitted radiation intensity. The change in the intensity dI_λ of the radiation emitted from the surface as it propagates through a path s in the atmosphere is equal to the absorption and the

70

emission of radiation by the atmospheric constituents within the path length ds.

$$dI_\lambda(s) = -\alpha(s)I_\lambda(s)ds + \alpha(s)B_\lambda(T(s))ds \qquad (4.4)$$

This equation can be integrated along the path to give the radiation intensity as a function of the path position. The absorption of upwelling radiation along a path is commonly referred to as the optical depth τ.

$$\tau(s) = \int_0^s \alpha(s)ds' \qquad (4.5)$$

The differential optical depth element $d\tau = \alpha(s)ds$ can be substituted into Equation 4.4.

$$\frac{dI_\lambda(s)}{d\tau(s)} = B_\lambda(T(s)) - I_\lambda(s) \qquad (4.6)$$

Multiplying both sides of Equation 4.6 by e^τ and integrating from the surface to some point s gives an expression for the radiation intensity along the path, assuming the relevant boundary conditions.

$$I_\lambda(s) = I_{\lambda,0}e^{-\tau(s)} + \int_{\tau(0)}^{\tau(s)} B_\lambda(T(s'))e^{-(\tau(s)-\tau(s'))}d\tau(s') \qquad (4.7)$$

Equation 4.7 only describes the path of upwelling radiation traveling through the atmosphere. In addition to upwelling radiation, the effects of downwelling radiation incident on the top of the atmosphere (primarily from the sun and from cosmic background radiation) must also be considered. For microwave radiative transfer, it is convenient to express the measured intensity as a brightness temperature, or the equivalent temperature of a blackbody radiating emission of the same intensity. Equation 4.8 gives the brightness temperature of the emission measured at s_t for a terrestrial planet with a non-negligible atmosphere, where ϵ is the surface emissivity and $R_\epsilon = 1 - \epsilon$. The first term represents

the contribution from the surface emission, the second term gives the contribution from up-welling atmospheric radiation, and the final term gives the contribution from downwelling radiation that reflects from the surface.

$$T_B = \epsilon T_{surf} e^{-\tau(s_t)} + \int_{\tau(0)}^{\tau(s_t)} T_{atm}(s') e^{-(\tau(s_t)-\tau(s'))} d\tau(s') + R_\epsilon T_{down} e^{-\tau(s_t)} \qquad (4.8)$$

$$T_{down} = \int_{\tau(s_t)}^{\tau(0)} \left(T_{atm}(s') + T_{cmb}\right) e^{-\tau(s')} d\tau(s') \qquad (4.9)$$

4.2 Ray Tracing Implementation

The expression for observed brightness temperature given in Equation 4.8 assumes an emission angle normal to the surface of the planet. For planets with a tenuous atmosphere, the expression can be modified to calculate the observed brightness temperature as a function of emission angle by dividing all τ terms by $\mu = \cos(\theta)$ where θ is the angle descending from zenith. While the assumption of a tenuous atmosphere is valid for the 70% N_2 atmosphere of Earth, it does not hold true for the 96.5% CO_2 atmosphere covering Venus. In order to accurately model the radiative transfer of Venus, a ray tracing scheme must be introduced to emulate atmospheric refraction for a spherical planet.

4.2.1 Iterative Ray Tracing

Radiation traveling through the atmosphere of Venus can be modeled as a ray passing through a series of discrete, homogeneous slabs [82]. For convenience, this ray is modeled as traveling towards the surface, as the ingress and egress ray paths are identical. To determine the emission path, an inbound ray begins at the top of the atmosphere ($>$100 km) and is defined by a location vector $\mathbf{R_o}$ and a direction vector $\mathbf{R_d}$. These vectors are established in a three-dimensional coordinate system with the origin $\mathbf{S_c}$ at the center of the planet. The

coordinates of the location and direction vectors are initialized at a reference latitude and longitude of (0°N, 0°W). The desired sub-ray latitude and longitude is specified, and the location and direction vectors are rotated through multiplication with the $\mathbb{R}$ matrix, defined in Equation 4.10 [83]. $\mathbb{I}$ is the 3×3 identity matrix, and $\mathbb{K}$ is the cross product matrix for a given unit vector $\mathbf{k} = [k_x, k_y, k_z]$, which is the rotation axis. The $\mathbb{R}$ matrix is defined separately for longitude and latitude rotations.

$$\mathbb{R} = \mathbb{I} + \sin(\theta)\mathbb{K} + (1 - \cos(\theta))\,\mathbb{K}^2 \tag{4.10}$$

$$\mathbb{K} = \begin{bmatrix} 0 & -k_z & k_y \\ k_z & 0 & -k_x \\ -k_y & k_x & 0 \end{bmatrix}$$

After rotation to the appropriate latitude and longitude point, the ray propagates layer by layer to the surface. At the interface between two layers, the ray will refract in accordance with Snell's Law. The new direction vector $\mathbf{L}$ of ray propagation is determined as a function of the incoming direction vector $\mathbf{I}$ (which is equivalent to $\mathbf{R}_d$), the surface normal vector $\mathbf{N}$, the relative index of refraction η, and the ingress and egress angles θ. Figure 4.2 shows the orientation of these vectors [82].

$$\mathbf{L} = \eta\mathbf{I} + (\eta\cos(\theta_1) - \cos(\theta_2))\,\mathbf{N} \tag{4.11}$$

$$\eta = \frac{\eta_1}{\eta_2} \tag{4.12}$$

$$\cos(\theta_2) = \sqrt{1 - \eta^2\left(1 - \cos^2(\theta_1)\right)} \tag{4.13}$$

$$\mathbf{N} = \frac{\mathbf{R_o} - \mathbf{S_c}}{\|\mathbf{R_o} - \mathbf{S_c}\|} \tag{4.14}$$
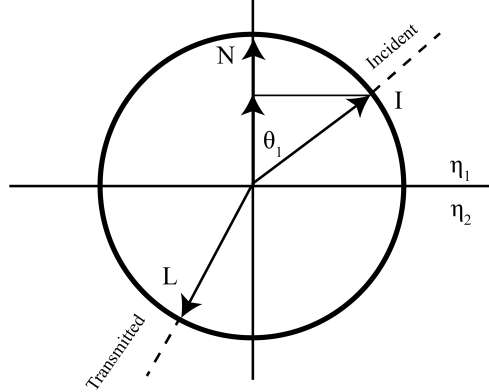
Figure 4.2: Refraction at the atmospheric layer boundary from Hoffman [82]

After the direction is updated by setting $\mathbf{R_d} = \mathbf{L}$, the ray travels through the next layer. If the incoming ray travels at an off-nadir angle, the distance traveled through this layer will be greater than the layer height. The distance ds from the ray origin at the prior layer to the intersection point with the next layer is given as a quadratic equation in terms of the location vector, the direction vector, and the vertical distance S_r between the next layer and the center of the planet.

$$ds = \frac{-B \pm \sqrt{B^2 - 4AC}}{2A}, \quad A = \|\mathbf{R_d}\|_2^2, \quad B = 2(\mathbf{R_o} \cdot \mathbf{R_d}), \quad C = \|\mathbf{R_o}\|_2^2 - S_r^2 \tag{4.15}$$

The smallest value of ds gives the correct distance. If the discriminant is positive, the ray travels to the next position specified by the equation below.

$$\mathbf{R_o^{n+1}} = \mathbf{R_o^n} + \mathbf{R_d} ds \tag{4.16}$$

After traveling the specified distance, the ray refracts at the next boundary layer. This process of ray refraction and propagation occurs until the ray impacts the surface. At each step in the ray propagation, information on the temperature, pressure, and mole fractions of atmospheric constituents are recorded for the final opacity calculation. If the discriminant for the distance equation is negative, the ray does not travel any farther towards the surface and exits the atmosphere. This represents the limb emission case. Both of these cases are illustrated in Figure 4.3.
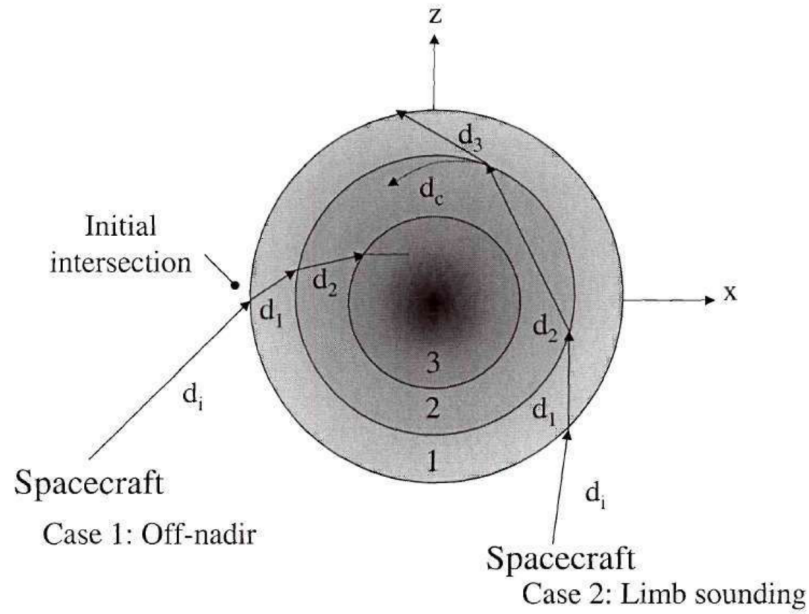
Figure 4.3: Possible ray paths from Hoffman [82]

For a ray that contacts the surface, the observed brightness temperature of radiation following the egress ray path is calculated using a discretized version of Equation 4.8 [84]. The discretized optical depth component $\tau_{i,j}$ is calculated as the product of the distance the ray travels through layer i and the total attenuation calculated for that layer for frequency j.

$$T_{B,j} = \epsilon T_{surf} e^{\left(-\sum_{l=1}^{N} d\tau_{i,j}\right)} + R_\epsilon T_{cmb} e^{\left(-2\sum_{l=1}^{N} d\tau_{i,j}\right)} + \sum_{i=1}^{N} T_j W_{i,j}^{up} + \sum_{i=1}^{N} T_j W_{i,j}^{down} \quad (4.17)$$

$$W_{i,j}^{up} = \left(1 - e^{-d\tau_{i,j}}\right) e^{\left(-\sum_{l=i+1}^{N} d\tau_{l,j}\right)} \tag{4.18}$$

$$W_{i,j}^{down} = R_\epsilon \left(1 - e^{-d\tau_{i,j}}\right) e^{\left(-\sum_{l=1}^{i-1} d\tau_{l,j}\right)} e^{\left(-\sum_{l=1}^{N} d\tau_{l,j}\right)} \tag{4.19}$$

A slight modification of Equation 4.17 gives the brightness temperature observed for the limb emission case. The weighting function values are only specified down to the point of deepest ray ingress.

$$T_{B,j}^{limb} = T_{cmb} e^{\left(-2\sum_{l=1}^{N} d\tau_{i,j}\right)} + \sum_{i=1}^{N} T_j W_{i,j}^{up} + \sum_{i=1}^{N} T_j \frac{W_{i,j}^{down}}{R_\epsilon} \tag{4.20}$$

While this iterative ray tracing scheme discussed is accurate, it is a relatively computationally expensive process. It is particularly useful for microwave observations below 10 GHz, where the contribution of surface emission becomes apparent and accurate maps of the surface emissivity and topography as a function of latitude and longitude are necessary.

4.2.2 Analytic Ray Tracing

For millimeter-wavelength observations of Venus, the contribution of the surface to the observed brightness temperature is minimal, and a simple surface model can be assumed with a uniform dielectric constant. This eliminates the requirement to precisely determine the latitude and longitude of the ray impact, and the location of the R_o vector does not need to be specified. For a spherically symmetric atmosphere, the path s of the ray can be determined analytically using Snell's law. Defining r as the distance of the ray from the center of Venus, n as the refractive index of the atmosphere as a function of r, θ as the look angle, and $k = \frac{2\pi}{\lambda}$ as the spatial wavenumber,

$$nr\sin(\theta) = k. \tag{4.21}$$

The value of k is calculated for a given starting emission angle, and the path length ds through each layer of the atmosphere can be calculated as

$$ds = \int_{r_i}^{r_{i-1}} \frac{nr}{\sqrt{(nr)^2 - k^2}} dr \tag{4.22}$$

Discretization of this integral enables efficient computation of ds for the entire ray path [85].

4.3   Model Inputs

The inputs to the microwave radiative transfer model consist of vertical profiles of atmospheric temperature and pressure, as well as vertical profiles of the abundance of microwave absorbers. These profiles are based on measurements made by science instruments onboard prior missions to Venus and the results of chemical modeling of the atmosphere. The volume mole fractions for all gas phase trace constituents below 100 kilometers is shown in Figure 4.4. Additionally, models of microwave and millimeter-wavelength opacity of the gas and aerosol constituents derived from laboratory measurements are included. All absorption models specified in the following sections yield values of absorption in units of decibels per kilometer.

4.3.1   Temperature and Pressure Profiles

The temperature and pressure profiles for the model are taken from both the Pioneer Venus entry probe experiments and the first Venus International Reference Atmosphere (VIRA). The temperature and pressure profiles from the Pioneer Venus Sounder and North Probes are used for lower and higher latitudes, respectively. The VIRA profiles are given for latitudes $< 30°$, $45°$, $60°$, $75°$, and $> 80°$, and hemispheric symmetry is assumed [86]. Plots of the temperature and pressure profiles with altitude are included in Figure 4.5 and 4.6.
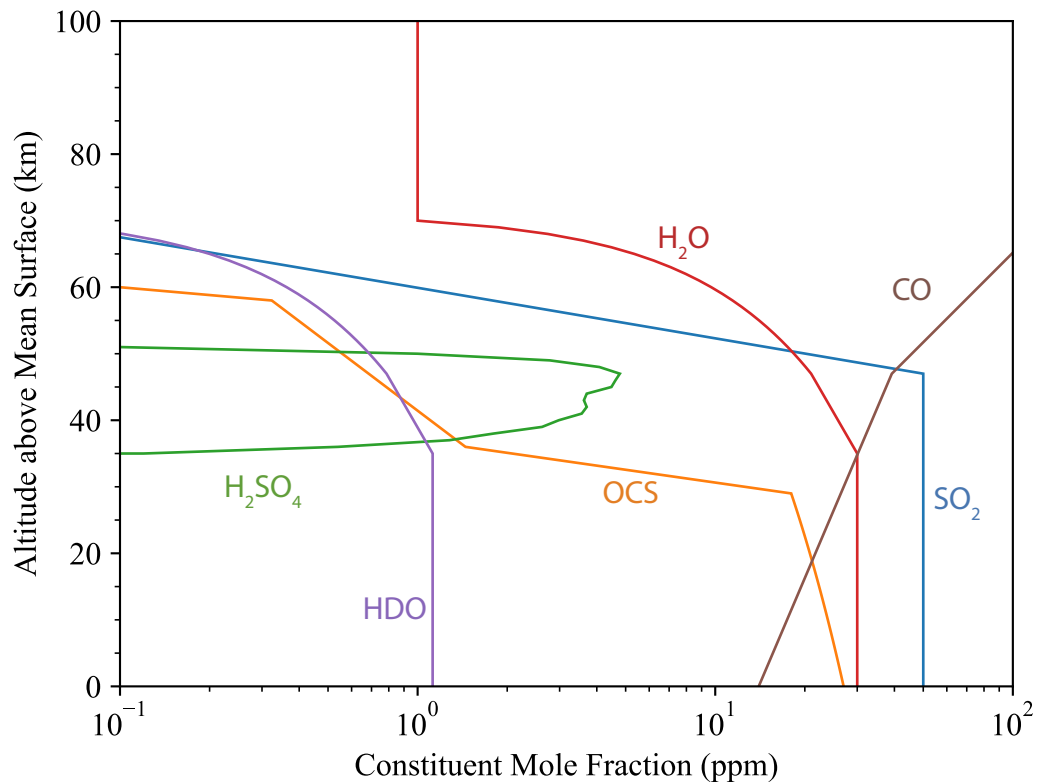
Figure 4.4: Mole fractions for gas phase trace constituents in the Venus atmosphere included in the radiative transfer model derived from chemical models [7, 8]. This plot shows a uniform subcloud SO_2 mole fraction of 50 ppm and a H_2SO_4 vapor profile derived from the Magellan Orbit 3212 radio occultation measurement.
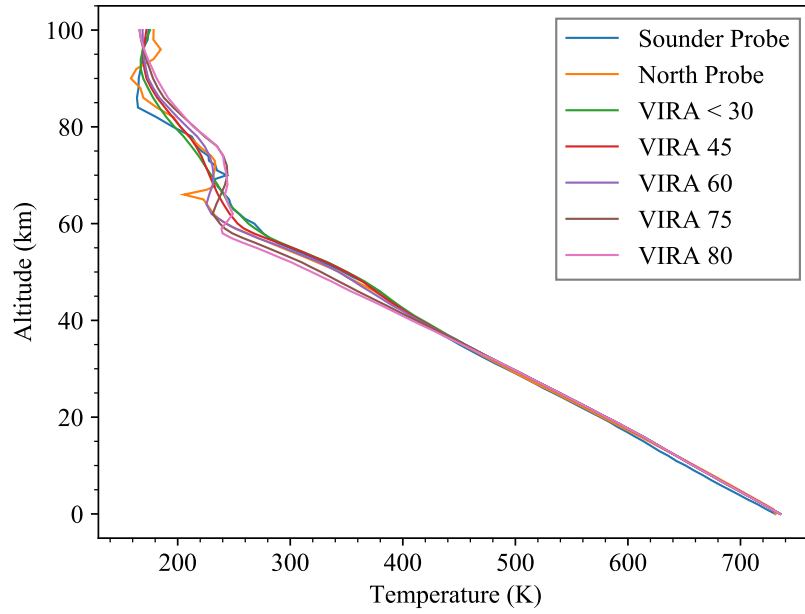
Figure 4.5: Temperature profile inputs to the radiative transfer model
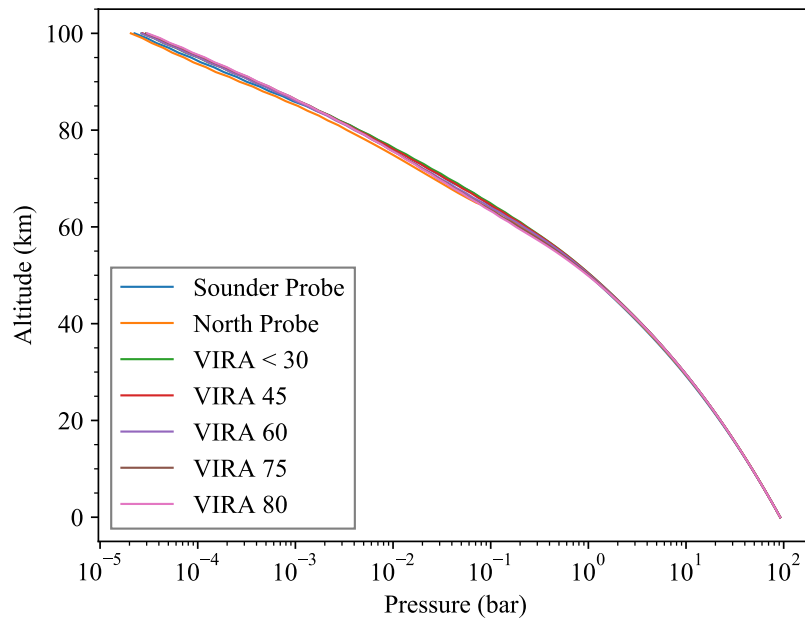
Figure 4.6: Pressure profile inputs to the radiative transfer model

4.3.2 Spectral Line Absorption

The opacities of the atmospheric constituents in this radiative transfer model are determined using pressure-broadened rotational spectral line absorption formalisms, many of which are informed by laboratory measurements under relevant Venus conditions. This absorption is calculated using the center frequencies $\nu_{o,j}$, intensities I_o, and the lower energy states E_o of the spectral lines for each constituent obtained from the JPL Millimeter and Submillimeter Spectral Line Catalog [67]. The pressure broadening of each line is described using the Van Vleck-Weisskopf formalism, which is applicable to microwave and millimeter-wavelength line broadening phenomena. The amount of pressure broadening is also governed by the pressure and temperature dependence of the line width $\Delta\nu$. This is further divided into the self-broadening contribution, and the contribution from broadening by foreign gases. The expressions for pressure-broadened absorption are given in Equations 4.23 through 4.27, where T_o is a reference temperature of 300 K.

$$\alpha = 10^6 log_{10}(e) \sum_j A_j \pi \Delta\nu F_j\left(\nu, \nu_{0,j}, \Delta\nu_j\right) \quad \text{dB/km} \tag{4.23}$$

$$F_{j,VVW}\left(\nu, \nu_{0,j}, \Delta\nu_j\right) = \frac{1}{\pi}\left(\frac{\nu}{\nu_{0,j}}\right)^2 \left(\frac{\Delta\nu_j}{\left(\nu_{0,j}-\nu\right)^2 + \Delta\nu_j^2} + \frac{\Delta\nu_j}{\left(\nu+\nu_{0,j}\right)^2 + \Delta\nu_j^2}\right) \quad \text{MHz}^{-1} \tag{4.24}$$

$$\Delta\nu = \gamma_s p_s \left(\frac{T_o}{T}\right)^m + \gamma_f p_f \left(\frac{T_o}{T}\right)^n \quad textMHz \tag{4.25}$$

$$A_j = 102.458 \frac{T_o}{T} I_j \frac{p_{H_2SO_4}}{\Delta\nu} \quad \text{cm}^{-1} \tag{4.26}$$

$$I_j = I_o \left(\frac{T_o}{T}\right)^{(n_j+1)} e^{-\left(\frac{hc}{k}E_o\left(\frac{1}{T}-\frac{1}{T_o}\right)\right)} \quad \text{nm}^2\text{MHz} \tag{4.27}$$

4.3.3 Sulfuric Acid Vapor and Aerosol

Abundance profiles for H_2SO_4 vapor are derived from the results of radio occultation measurements made using Mariner 10 and Magellan [41]. For low latitudes, the results of the Mariner 10 radio occultation experiment are used, while the Magellan results are used for higher latitudes. These models are in agreement with the theoretical saturation vapor pressure of H_2SO_4. Above the altitudes specified by the radio occultation results, the H_2SO_4 vapor abundance is assumed to be negligible, in accordance with ground-based observations [31]. Below the refraction limit of the radio occultation results (altitudes less than 32.8 km), the H_2SO_4 abundance is also assumed to be negligible, as at sufficiently high temperatures, H_2SO_4 dissociates to H_2O vapor and SO_3. Figure 4.7 shows the retrieved H_2SO_4 vapor abundances from the Mariner 10 and Magellan radio occultation experiments. Also shown are several H_2SO_4 vapor profiles derived from radio occultations performed by Venus Express (Oschlisniok, personal communication). The expression for H_2SO_4 vapor opacity at used is the same as the model derived earlier in this work.

The model input for the bulk density of the H_2SO_4 cloud layers is taken from the Pioneer Venus Large Probe cloud particle size spectrometer (LCPS) experiment, which remains the most reliable dataset of its kind for the lower latitude cloud properties of Venus [87]. The LCPS instrument measured cloud and haze structure between 30 and 70 kilometers above the surface of Venus, as shown in Figure 4.8.

The cloud region of Venus spans 45-70 kilometers and can be divided into the upper, middle, and lower cloud regions by the measured mass loading. Within the lower and middle cloud, a trimodal distribution of particle sizes was measured with mean diameters near 0.5, 2, and 8 μm. For this model, only the contribution of the lower cloud region from 47-50 kilometers is included. The concentration of the clouds is assumed to equal 85% H_2SO_4, although the concentration near the cloud base may be higher than this estimate [88].

The microwave and millimeter-wavelength opacity of liquid H_2SO_4 is taken from the
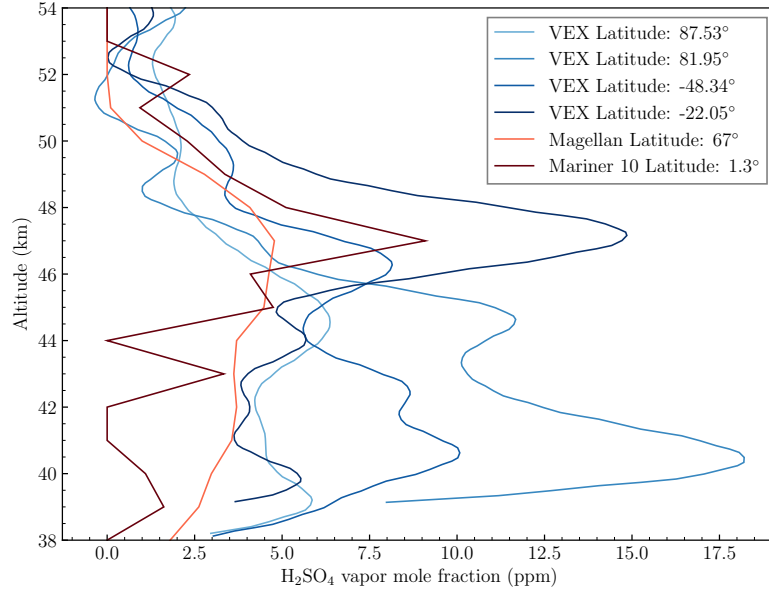
Figure 4.7: H_2SO_4 vapor abundance profiles measured from prior Venus radio occultation experiments (Oschlisniok, personal communication).

laboratory measurements of Fahd and Steffes for 85% and 99% H_2SO_4 solutions [42]. M is the cloud bulk density in mg/m^3, and ρ is the density of liquid H_2SO_4 (1.84×10^9 mg/m^3). Opacities for a cloud bulk density of 50 mg/m^3 are shown in Figure 4.9.

$$\alpha_{cloud} = \frac{246 M \epsilon_r''}{\rho \lambda \left[\left(\epsilon_r' + 2 \right)^2 + \left(\epsilon_r'' \right)^2 \right]} \tag{4.28}$$

$$\epsilon_r^{85\%} = \epsilon_r' - j\epsilon_r'' = 3.3 + \frac{87.5 - 3.3}{1 + j \left(2\pi f \left(1.7 \times 10^{-11} \right) \right)^{0.09}} \tag{4.29}$$

$$\epsilon_r^{99\%} = \epsilon_r' - j\epsilon_r'' = 4.96 + \frac{94.24 - 4.96}{1 + j \left(2\pi f \left(6.38 \times 10^{-11} \right) \right)^{0.143}} \tag{4.30}$$

Calculations of the Mie coefficients resulting for cloud droplet scattering are not included in this model due the relatively small size of the cloud aerosols at Venus. During its descent, the Pioneer Venus probe measured a mean mode 3 particle diameter of 8 μm
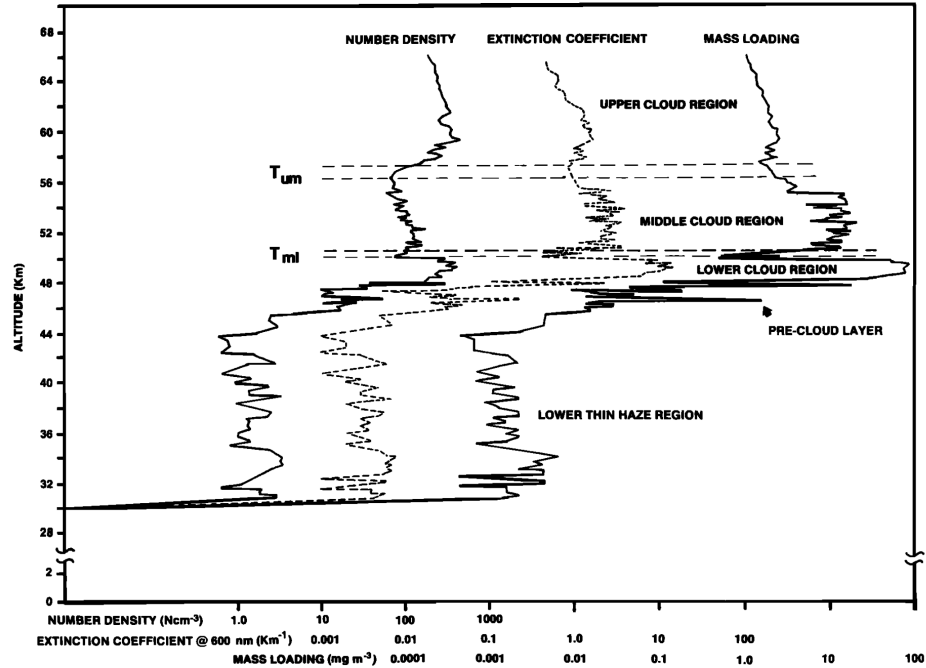
Figure 4.8: Cloud number density, extinction coefficient, and mass loading as measured by the LCPS instrument from Knollenberg and Hunten [87]

and did not sample any cloud aerosols with a diameter greater than 35 μm. The extinction, scattering, and absorption cross sections for an 85% H_2SO_4 cloud particle were determined as a function of cloud droplet radius for a frequency of 100 GHz using the equations for Mie scattering [89]. These calculations suggest that cloud particle radii on the order of 300 micron would be needed for scattering to contribute significantly to the extinction of millimeter wavelength radiation, as illustrated in Figure 4.10.

4.3.4   Sulfur Dioxide

There are two treatments of the SO_2 abundance in this model. The first is to assume a uniform mole fraction of SO_2 below 47 kilometers and exponential decay above this reference altitude with a scale height of 3.3 kilometers. This decay continues until a mean altitude of 80 km above the surface, at which point there is either a slight increase or a leveling off of the mole fraction, in accordance with chemical models [8, 9]. The model discrepancy in the SO_2 mole fraction in the mesosphere does not significantly affect the radiative
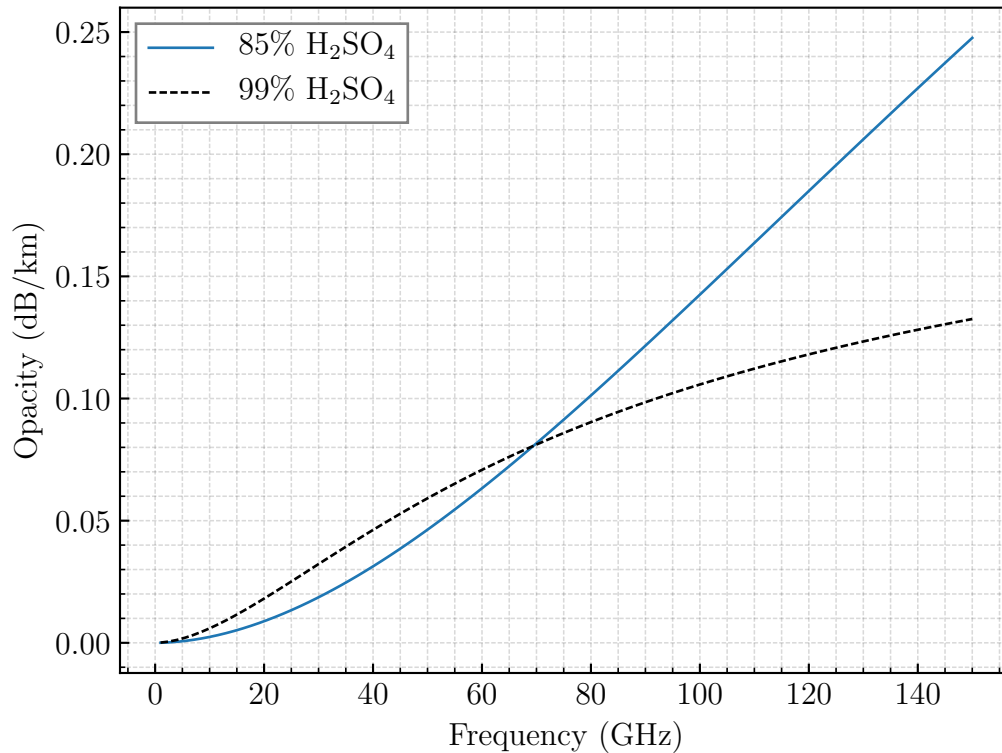
Figure 4.9: Opacity of a 85% and 99% H_2SO_4 cloud with a bulk density of 50 mg/m^3

transfer model of 2-4 millimeter emission, so the results of Krasnopolsky's photochemical model are used by default [8]. The uniform mole fraction in the troposphere is assumed to be between 50 and 150 ppm. For low latitudes, the value is set to 150 ppm, which is the consensus of satellite and ground-based remote observations in the infrared [90]. At higher latitudes, however, the mole fraction of SO_2 may decrease [23].

This treatment of the SO_2 mole fraction is at odds with the results of the ISAV 1 and ISAV 2 ultraviolet experiments onboard the Vega 1 and Vega 2 landers. With atmospheric insertion times just four days apart, the retrieved SO_2 profiles appear drastically different immediately below the cloud layers, as shown in Figure 4.11 [91].

If correct, these profiles indicate significant longitudinal variability in the sub-cloud and lower cloud SO_2 mixing ratio. Furthermore, both the results suggest that the mixing ratio
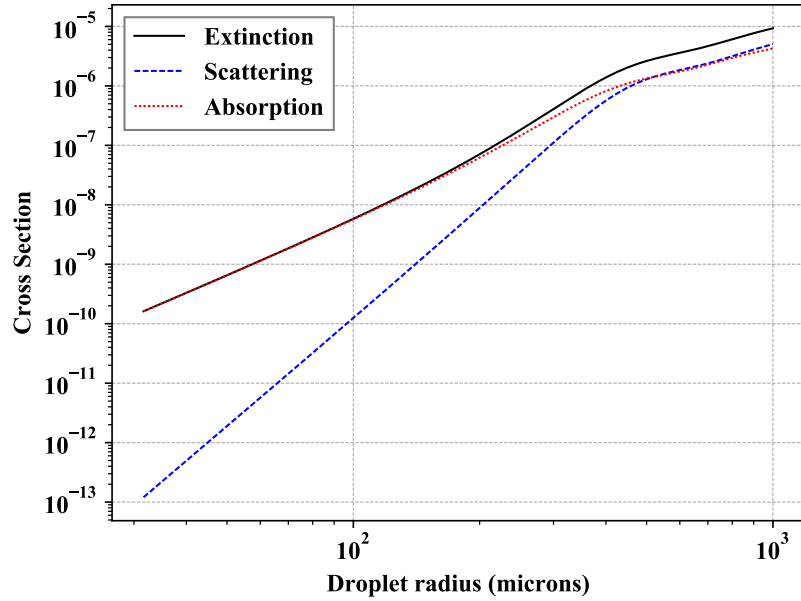
Figure 4.10: Contribution of absorption and scattering to the extinction cross section of a droplet of liquid H_2SO_4 as a function of the droplet radius. These values are calculated assuming a cloud bulk density of 50 mg/m^3 for a frequency of 100 GHz.

of SO_2 decreases towards the surface.

The microwave and millimeter-wavelength absorption of SO_2 has been measured under a variety of conditions relevant to the Venus atmosphere [39, 40, 43, 37]. The Van Vleck-Weisskopf model presented by Fahd and Steffes [39] (using the temperature coefficients from Suleiman et al. [40]) provides the best fit to the data, and the parameters corresponding to the equations in Subsection 4.3.2 are given in Table 4.1.

4.3.5   Abundance of Carbon Dioxide, Nitrogen, and other Trace Species

H_2O vapor, OCS, and CO have also been included in this radiative transfer model. Although these species contribute to atmospheric opacity near strong millimeter-wavelength spectral lines, they contribute negligibly to the continuum microwave opacity of the atmosphere. The mole fractions of the limited absorbers are taken from the atmospheric chemical models [7, 8]. Due to its limited abundance and limited opacity, HCl has not been included in the model [44]. The abundances of CO_2 and N_2 are determined by subtracting
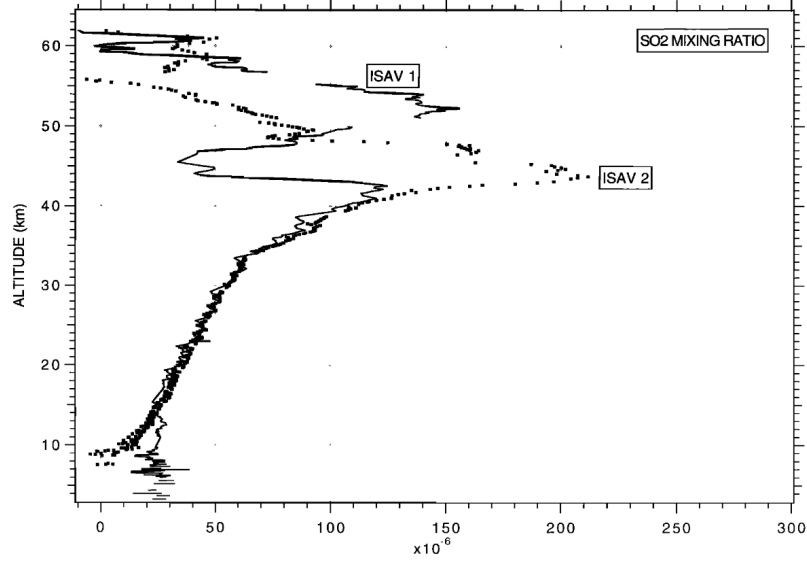
Figure 4.11: Tropospheric profiles of SO$_2$ derived from the ISAV 1 and ISAV 2 experiments [91]

the sum the abundance q of other constituents $\left(1 - \sum_i q_i\right)$ and multiplying the result by 96.5% and 3.5%, respectively. While it has been suggested that a nitrogen gradient exists in the altitude range of 10 kilometers to the surface, this is not taken into account for this model [92].

The expression for CO$_2$-N$_2$ absorption as a function of mixing ratio q, pressure p, temperature T, and frequency f comes from the work of Ho et al. [36].

$$\alpha_{CO_2/N_2} = 1.12 \cdot 10^8 \left(q_{CO_2}^2 + 0.25 q_{CO_2} q_{N_2} + 0.0054 q_{N_2}^2\right) f^2 p^2 T^{-5} \quad \text{dB/km} \quad (4.31)$$

Most models for H$_2$O absorption at microwave and millimeter-wavelengths consist of a spectral line contribution and a continuum contribution [66]. For the spectral line contribution, the JPL spectral line catalog is used [67], and the linewidths and temperature coefficients for CO$_2$ broadening of H$_2$O spectral lines use the values calculated by Bauer et al. [68], where $\Delta\nu$ = 6.24 MHz/torr and the corresponding temperature coefficient is 0.57 for the 183 GHz line. For the continuum absorption contribution (α_c), the continuum model of Bauer et al.[69] for absorption of H$_2$O and CO$_2$ mixtures at 239 GHz as a function

of temperature is extrapolated to lower frequencies (ν).

$$\alpha_c = \nu^2 p_{H_2O} \left(a(T) p_{CO_2} + b(T) p_{H_2O} \right) \quad \text{cm}^{-1}/\text{Torr} \tag{4.32}$$

$$a(T) = 8.21 \times 10^{-14} \left(\frac{296}{T} \right)^{5.07}, \quad b(T) = 6.022 \times 10^{-13} \left(\frac{296}{T} \right)^{7.84} \tag{4.33}$$

For the other constituents described in this section, no laboratory measurements exist of the millimeter-wavelength opacity under Venus conditions. Absorption is approximated using a Van Vleck-Weisskopf lineshape model with broadening parameters derived from laboratory measurements at lower temperatures. The linewidth and temperature coefficient parameters used for the spectral contributions from each component are given in Table 4.1 with their sources. The parameterizations employed for these limited absorbers, while not thorough treatments, are sufficient to estimate their opacity contribution.

Table 4.1: Table of lineshape parameters for gas phase constituents

Constituent	γ_s (MHz/torr)	γ_f (MHz/torr)	m	n	Source
SO_2	16	7	0.85	0.85	[39]
H_2O	18.80	6.24	0.79	0.57	[68]
CO	3.36	4.93	1.03	0.8	[93, 94, 95]
OCS	4.24	9.6	0.9	0.9	[96]

4.3.6 Refractivity

The refractivity $N(z)$ for each layer in the model Venus atmosphere can be calculated as a function of position. N here represents the density-normalized refractivity of a 96.5% CO_2 and 3.5% N_2 atmosphere (251.09 m^3/kg) [97]. From the refractivity, the index of refraction $n(z)$ can be determined.

$$N(z) = \frac{NP(z)}{RT(z)} \tag{4.34}$$

$$n(z) = N(z) \times 10^{-6} + 1 \qquad (4.35)$$

Although both SO_2 and H_2SO_4 are highly refractive, their limited abundances preclude significant refractive effects on the ray path. Additionally, it is assumed that the atmosphere is in local thermodynamic equilibrium, with no variations in refractive index within any given slab. This is certainly not true, but this assumption is sufficient to provide an approximation of the ray path.

4.3.7 Surface Model

For microwave remote sensing, the emission properties of the surface can contribute substantially to the observed brightness temperature at low frequencies [98]. Models of surface reflectivity and topography, shown in Figures 4.12 and 4.13, are included in the radiative transfer model from the Global Topography, Emissivity, Reflectivity, and Slope Data Record derived from the Magellan radar experiment [99].
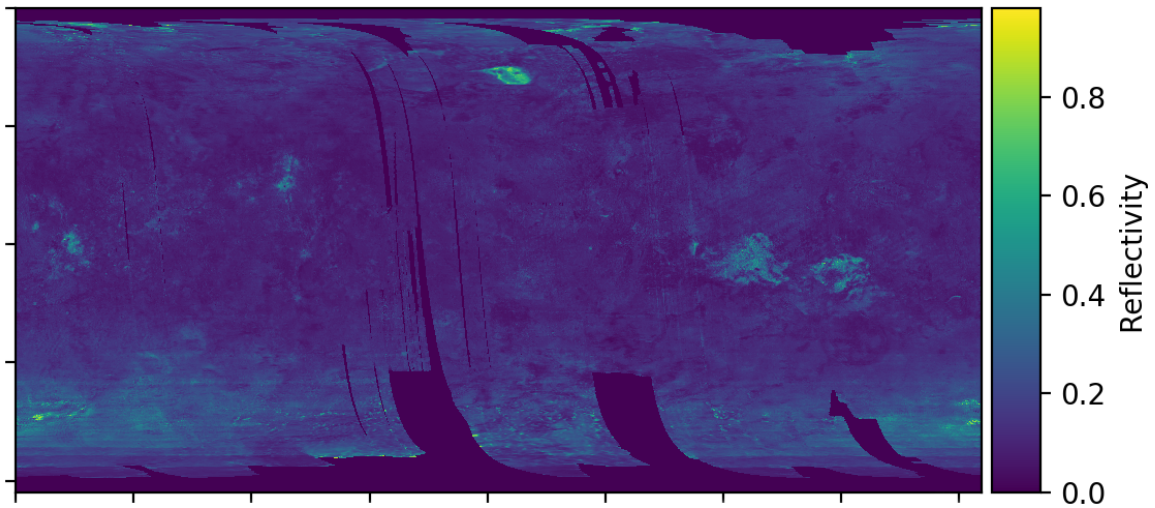
Figure 4.12: Map of Venus surface reflectivity from the Magellan Global Reflectivity Data Record [99].

Each pixel from these maps covers a 4,641 by 4,641 meter area of the surface. The topographical map is changed to give the height of surface features as a distance in kilo-
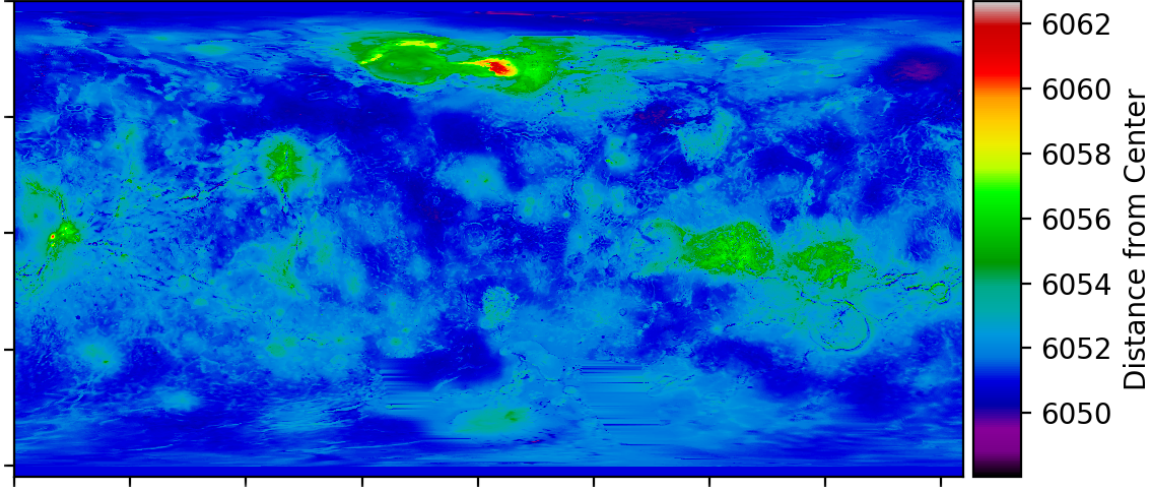
Figure 4.13: Map of Venus surface topography from the Magellan Global Topography Data Record [99]. Units for topography are kilometers from the center of Venus.

meters from the mean Venus radius of 6051.8 kilometers. This surface height serves as the termination point for the ray-tracing process. To determine the dependence of the surface reflectivity and thereby emissivity on angle of emission/impact, the map reflectivity data are converted into surface dielectric constant (ε) values .

$$\varepsilon = \left(\frac{1 + \sqrt{R}}{1 - \sqrt{R}} \right)^2 \tag{4.36}$$

The surface reflectivity as a function of angle can then be calculated from this information and from the index of refraction of the atmospheric layer immediately above the surface η_1. This reflectivity can be used to calculate the emissivity ($R_\epsilon = 1 - \epsilon$).

$$R_\epsilon(\theta) = \frac{1}{2} \left[\frac{cos(\theta) - \sqrt{\frac{\varepsilon}{\eta_1^2} - sin^2(\theta)}}{cos(\theta) + \sqrt{\frac{\varepsilon}{\eta_1^2} - sin^2(\theta)}} \right]^2 + \frac{1}{2} \left[\frac{\frac{\varepsilon}{\eta_1^2} cos(\theta) - \sqrt{\frac{\varepsilon}{\eta_1^2} - sin^2(\theta)}}{\frac{\varepsilon}{\eta_1^2} cos(\theta) + \sqrt{\frac{\varepsilon}{\eta_1^2} - sin^2(\theta)}} \right]^2 \tag{4.37}$$

No expression for subsurface emission is included in this model. For the simple surface approximation applicable to millimeter-wavelength observations, the surface is assumed to be uniform with a distance from the center of the planet equal to the mean radius of Venus

and a dielectric constant $\epsilon_r = 4$ [100].

4.4 Model Outputs

The outputs of the radiative transfer model are the observed brightness temperatures and the atmospheric weighting functions as described in Equations 4.17-4.19. An example of the atmospheric weighting functions are shown assuming a uniform SO_2 sub-cloud abundance of 150 ppm and the H_2SO_4 vapor profile from the Mariner 10 radio occultation.
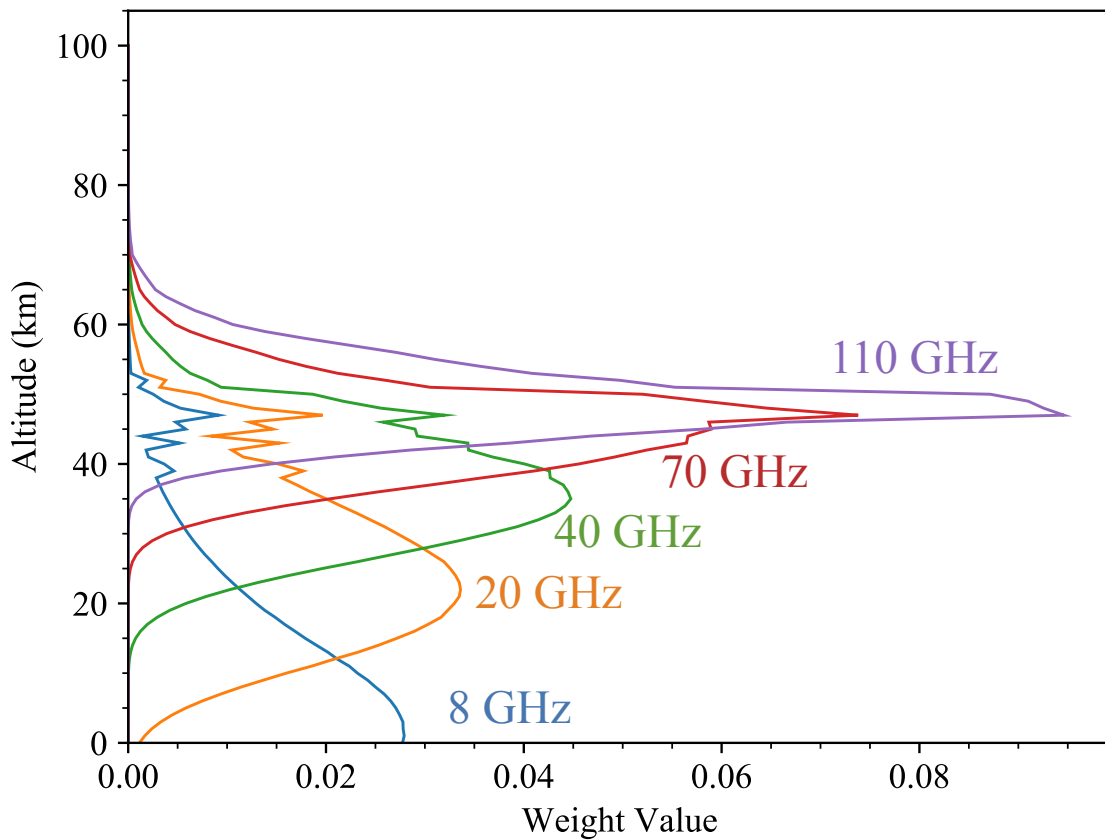
Figure 4.14: Weighting functions for several observation frequencies as a function of altitude.

These weighting functions describe the effective contribution of the neutral atmosphere to the observed emission temperature as a function of frequency and altitude. While lower frequencies ($<$10 GHz) are primarily sensitive to surface emission, higher frequencies are

sensitive to emission from higher in the atmosphere. The weighting functions change significantly at frequencies associated with spectral lines of trace species in the Venus atmosphere, such as CO.

Figure 4.15 shows a comparison of model disk-averaged brightness temperature output with prior microwave observations of Venus [84].
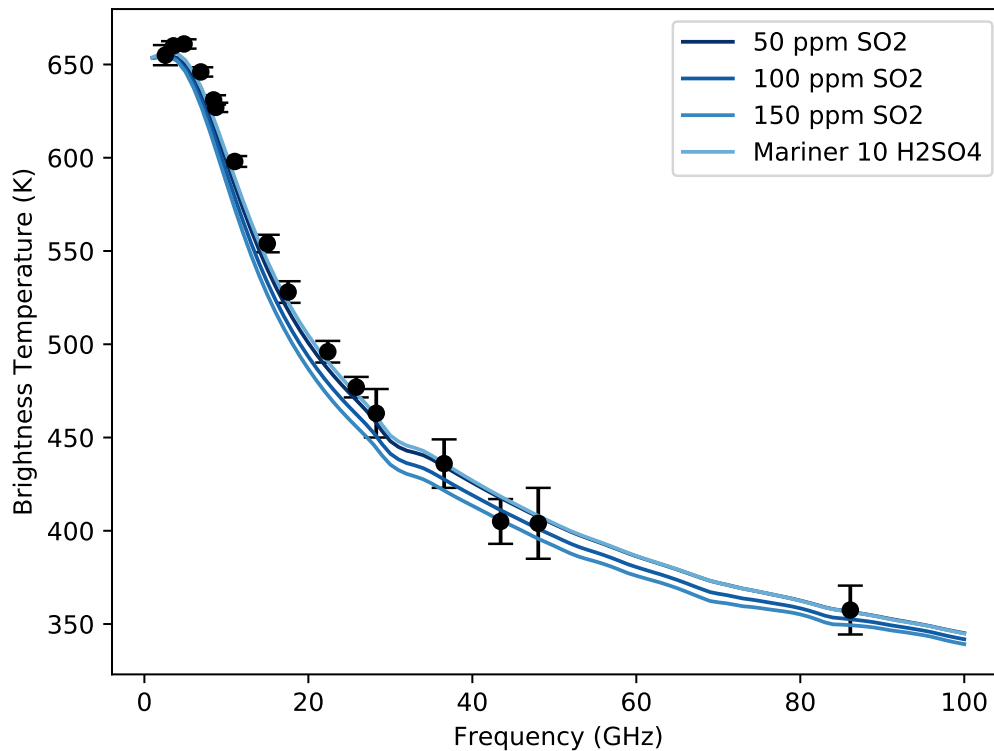
Figure 4.15: Microwave observations of Venus [79, 80] as compared with the radiative transfer model output brightness temperature.

4.4.1 Dual Band Radio Occultations of Venus

The radio occultation technique measures the doppler shift and attenuation of a coherent radio signal transmitted between a spacecraft and the ground station as it passes through the atmosphere. These measurements can be used to determine the ray impact parameter a and the bending angle δ (shown in Figure 4.16), which can be in turn be converted to

vertical profiles of atmospheric refraction and absorption via the inverse Abel Transform [101, 102].

$$\ln(n(r_0)) = \frac{1}{\pi} \int_{a(r_0)}^{\infty} \frac{\delta(a)da}{\sqrt{a^2 - a(r_0)^2}} \tag{4.38}$$

$$\alpha(r_0) = -\frac{n(r_0)}{\pi a(r_0)} \frac{d}{da} \left[\int_{a(r_0)}^{\infty} \frac{\tau(a)ada}{\sqrt{a^2 - a(r_0)^2}} \right] \tag{4.39}$$
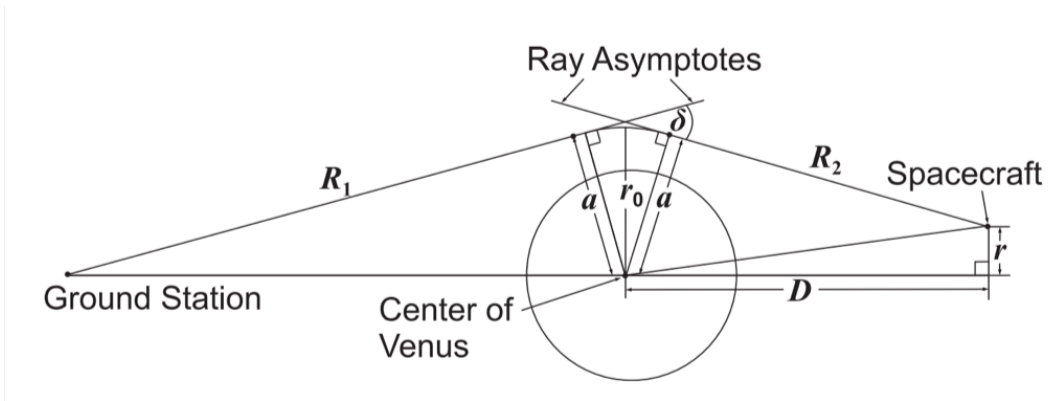
Figure 4.16: Ray geometry for the radio occultation measurement [102]

The τ term in Equation 4.39 represents the contribution of the atmospheric opacity to the total signal attenuation. Losses in the signal also occur due to refractive defocusing, shown in Figure 4.17, and antenna mispointing.

Prior missions to Venus have flown with radio occultation experiments operating at S Band (2.3 GHz) and X Band (8.3 GHz), but the K_a Band (32 GHz) operating frequency of the Deep Space Network (DSN) has yet to be used for occultations of Venus. The results of the laboratory measurements of H_2SO_4 vapor opacity can be used in conjunction with the radiative transfer model to predict the atmospheric attenuation experienced by a K_a Band occultation signal.

For S, X, and K_a Band occultations, empirical absorption expressions have been fit to the laboratory measurements nearest to the DSN operating frequencies, as discussed in Chapter 3. The expressions for the S and X band absorption are modified from the original
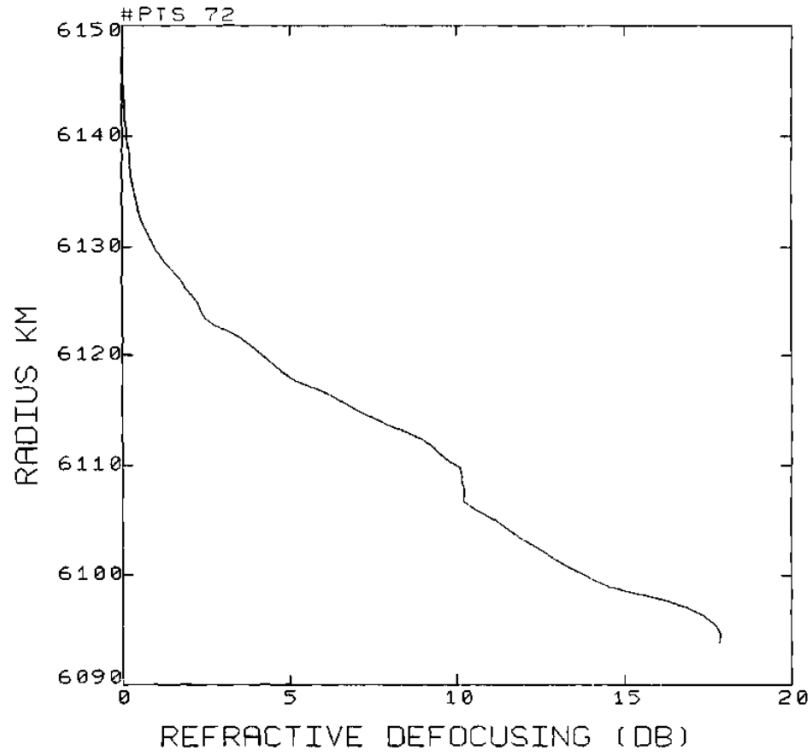
Figure 4.17: Example of signal attenuation due to refractive defocusing from Jenkins [103]

expressions given by Kolodner and Steffes due to a redetermination of the H_2SO_4 mole fraction present during their laboratory measurements based on Appendix A. These revised expressions have been applied to radio occultation measurements of Venus Express and suggest improved agreement between measured H_2SO_4 vertical profiles and the saturation vapor pressure of H_2SO_4 (Oschlisniok, personal communication). Figure 4.18 shows the 32 GHz absorptivity in dB/km of H_2SO_4 vapor and aerosol, SO_2 and CO_2 assuming a uniform SO_2 abundance below the clouds of 150 ppm and the Magellan orbit 3212 radio occultation experiment H_2SO_4 vapor profile.
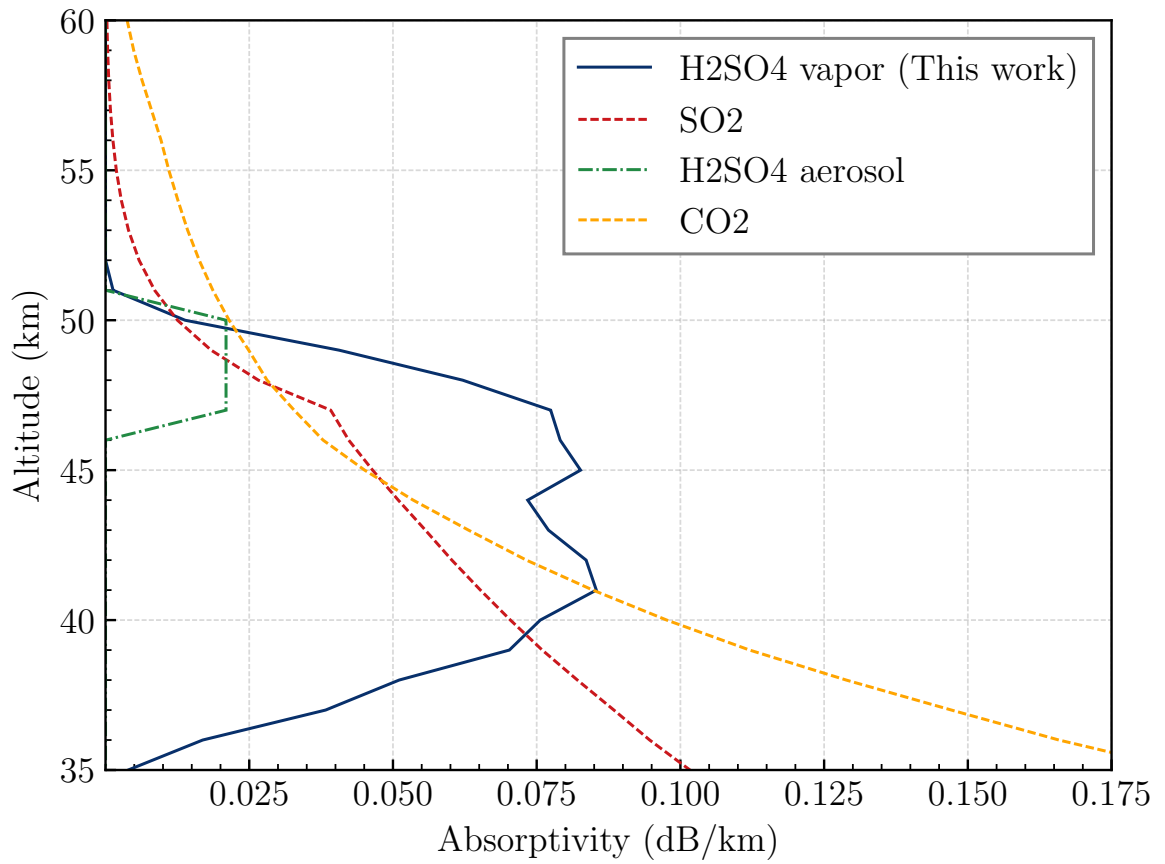
Figure 4.18: Absorptivity of CO_2 and trace gases in the Venus atmosphere at 32 GHz.

The opacity of the Venus atmosphere is much greater at K_a Band than at X or S Band, and the sounding depth of the K_a Band signal will be attenuation-limited. This enhanced opacity, however, provides an opportunity to extract additional meaningful information from a dual band radio occultation experiment. The opacity associated with H_2SO_4 vapor determined by S or X band attenuation can be subtracted from the K_a Band signal, and the residual attenuation can be associated with variations in the bulk density of the lower cloud. The change in signal attenuation due to the presence of the cloud has been simulated for three H_2SO_4 abundance profiles shown in Figures 4.19-4.21.
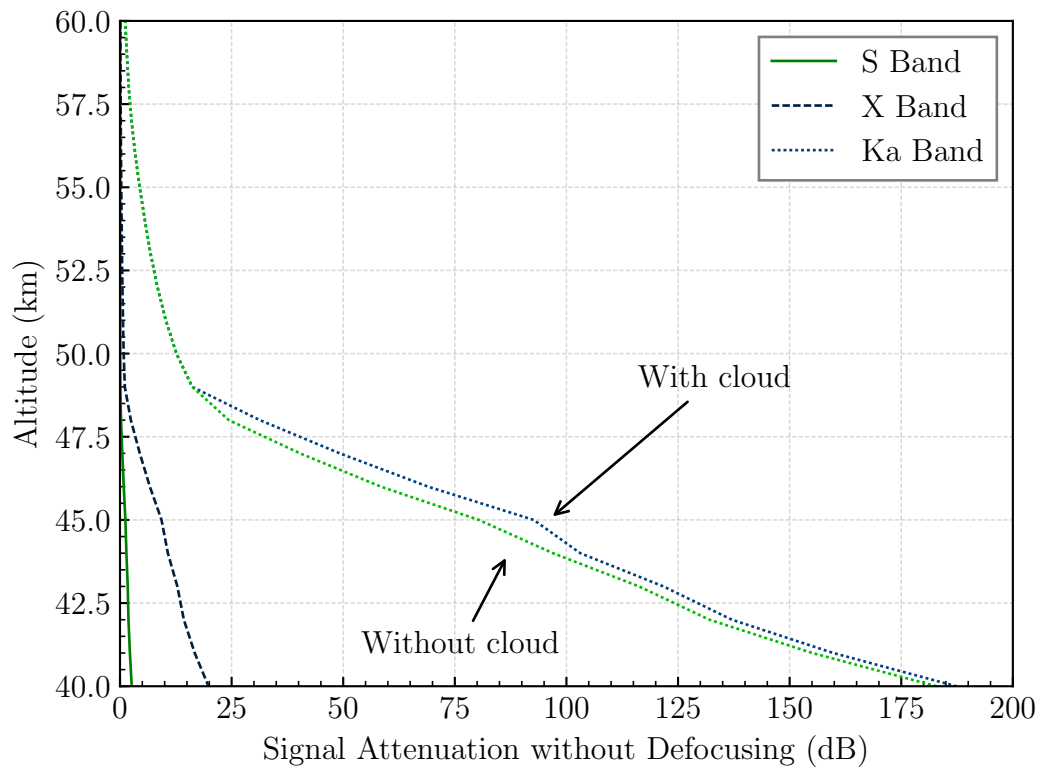
Figure 4.19: Difference between atmospheric signal attenuation at S, X, and K_a Band occultation frequencies with and without a cloud component. The H_2SO_4 profile used here is that of the Magellan orbit 3212 radio occultation experiment [41]. This plot does not include effects of atmospheric defocusing on signal intensity
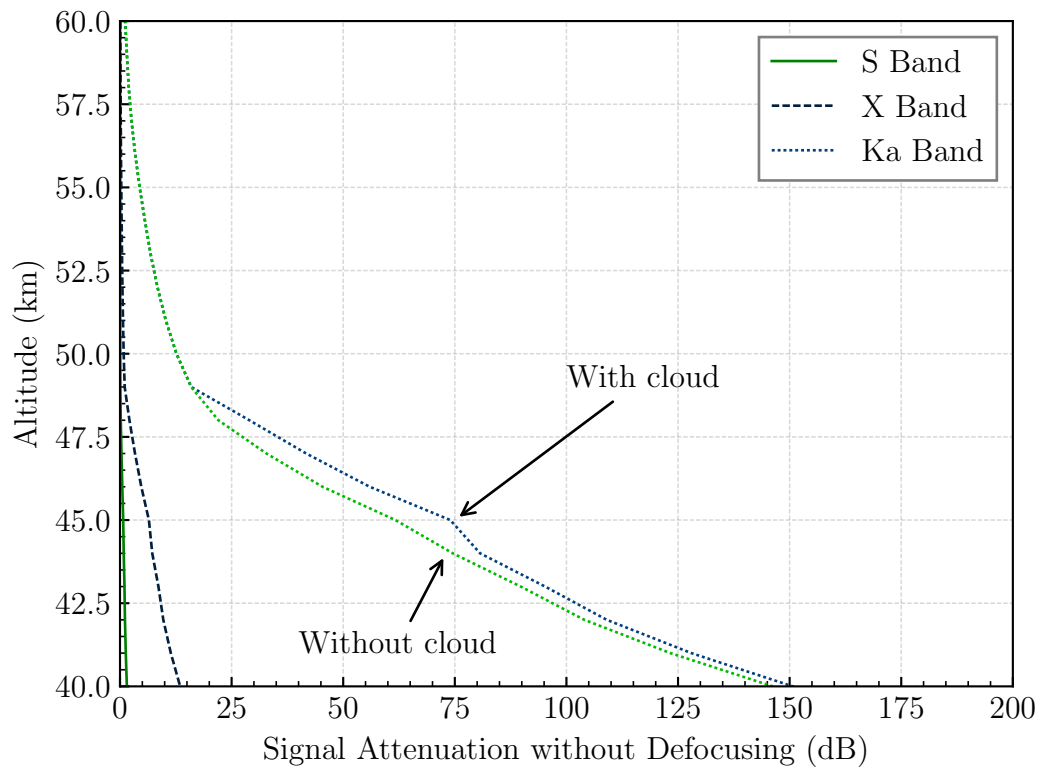
Figure 4.20: Difference between atmospheric signal attenuation at S, X, and K_a Band occultation frequencies with and without a cloud component. The H_2SO_4 profile used here is half that of the Magellan orbit 3212 radio occultation experiment [41]. This plot does not include effects of atmospheric defocusing on signal intensity
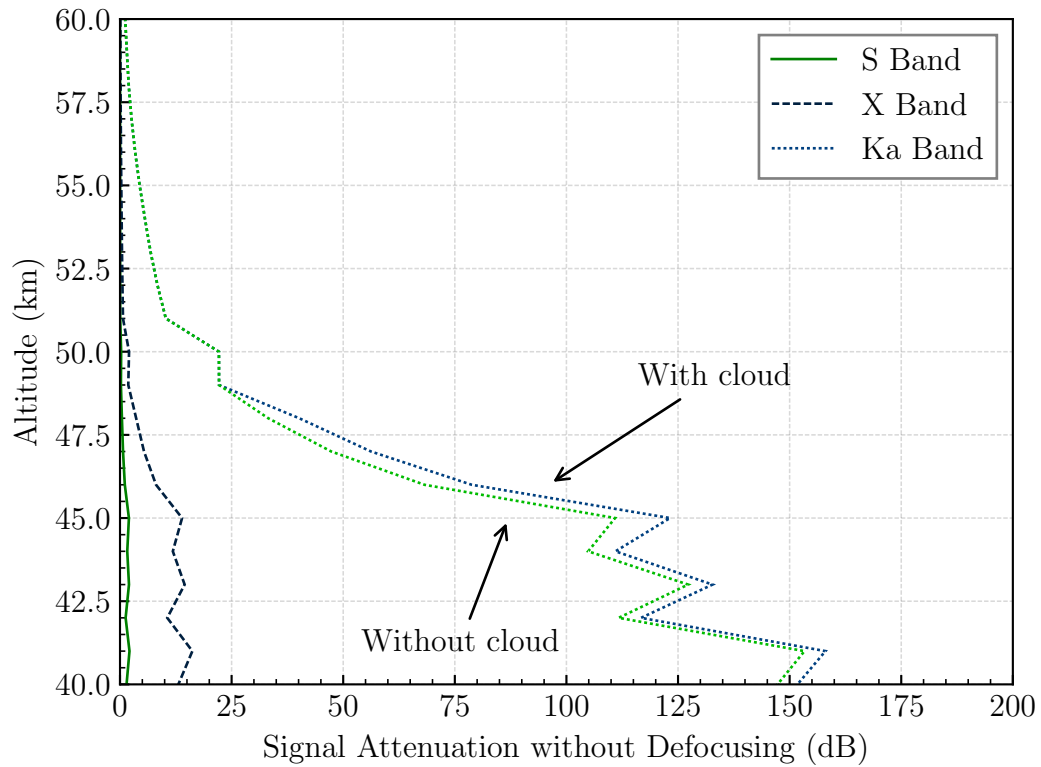
Figure 4.21: Difference between atmospheric signal attenuation at S, X, and K_a Band occultation frequencies with and without a cloud component. The H_2SO_4 profile used here is that of the Mariner 10 radio occultation experiment [41]. This plot does not include effects of atmospheric defocusing on signal intensity

These profiles are representative of high latitude, middle latitude, and lower latitude Venus atmospheric conditions, respectively. A more complete picture of H_2SO_4 variation as a function of latitude derived from the Venus Express radio occultation experiment is shown in Figure 4.22 [19].
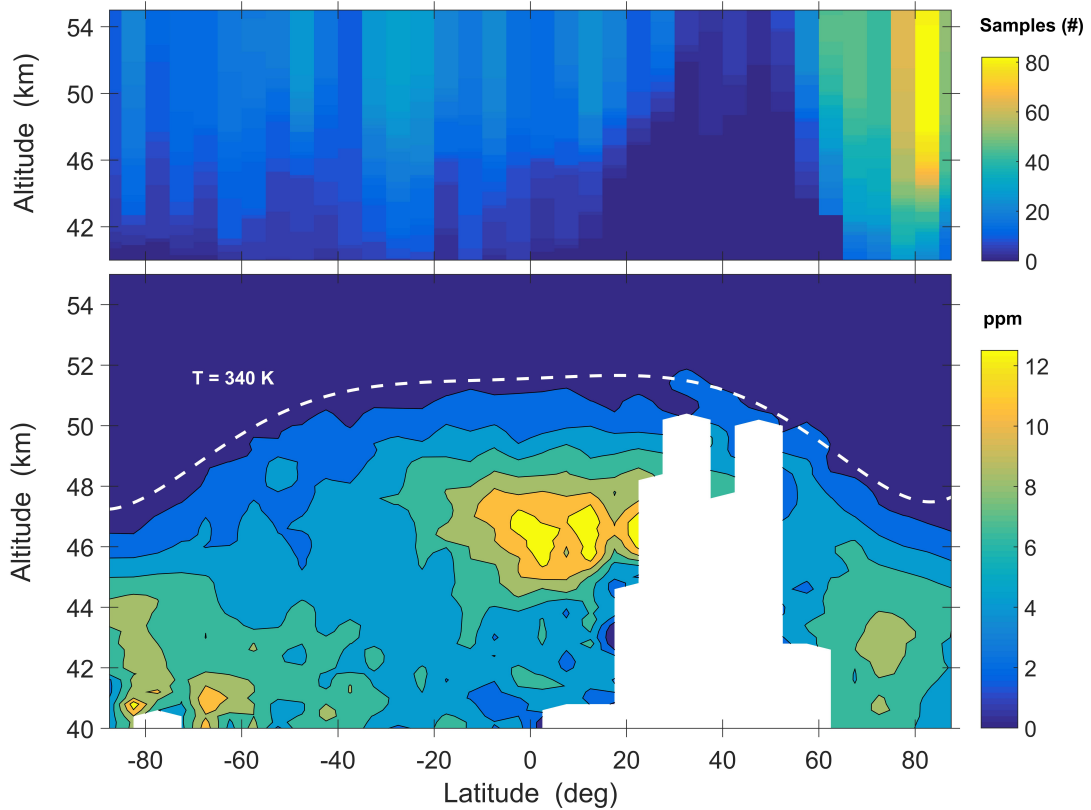
Figure 4.22: H_2SO_4 vapor abundance as a function of latitude from the results of the Venus Express VeRa radio occultation experiment from Oschlisniok et al. [104].

These results can be used to estimate the sounding depth of the 32 GHz radio occultation signal. First, the signal to noise ratio P_r/P_n for a nominal K_a Band radio occultation experiment can be determined through the Friis transmission equation and the noise power equation [89].

$$P_r = \frac{\eta A_t A_r P_t}{\lambda^2 R^2} \quad \text{Watts,} \tag{4.40}$$

$$P_n = kT_{sys}B \quad \text{Watts} \tag{4.41}$$

Assuming a transmitter power P_t of 20 W, a distance R from Venus of 0.71 AU, the effective areas A of the Magellan 3.7-m high gain antenna (10.7 m^2) and the DSN 34-meter antennas (555.6 m^2) , and the noise temperature (25 K) and bandwidths ($<$1 Hz) for the DSN radio science receivers, a free space signal to noise ratio of 84 dB is determined [105, 14, 106]. Losses in signal strength will occur due to refractive defocusing L_r, antenna mispointing L_m, loss due to propagation through the Earth's atmosphere L_e, and loss due to propagation through the Venus atmosphere L_v. The maximum L_v that can be sustained before the signal falls below the noise floor is then

$$L_v = \frac{P_r}{P_n} - L_r - L_m - L_e \quad \text{dB} \tag{4.42}$$

Assuming $L_r = 20$ dB, $L_m = 4$ dB, $L_e = 1$ dB, the maximum sustainable Venus atmospheric loss $L_v = 59$ dB. For the profiles shown in Figures 4.19-4.21, this occurs between 46-47 kilometers above the surface. While the parameters of this calculation will vary depending on the radio occultation experiment design and the parameters and orientation of the DSN antennas, it is clear that the K_a band signal will not penetrate the Venus atmosphere down to the refraction limit of 32.8 km.

CHAPTER 5

INTEROFEROMETRIC OBSERVATIONS OF VENUS

All passive observations of the millimeter-wavelength emission from Venus have been carried out with ground-based radio telescopes. Powerful radio interferometers capable of carrying out correlated measurements of millimeter-wavelength emission from Venus have enabled the development of spatially resolved measurements of the planet. In this chapter, images derived from recent observational campaigns are discussed. The theory of practical solar system radio interferometry is discussed, followed by the presentations of spatially resolved images of the Venus disk from 2-3 millimeter-wavelengths.

5.1 Millimeter-wavelength Interferometry

For astronomical observations, it is generally useful to be able to resolve fine spatial features of the object of interest. The relationship $\theta \propto \frac{\lambda}{D}$ gives a theoretical limit to the obtainable angular resolution θ for an observation at a particular wavelength λ with a telescope of having an aperture diameter of D. At microwave and millimeter-wavelengths, this limit imposes unreasonable constraints on the size of a single radio telescope necessary so as to obtain arcsecond-scale resolutions. As an example, obtaining a 1 arcsecond resolution for an observation at 2 millimeters would roughly require a radio telescope with a dish diameter of 400 meters. To obtain higher angular resolution at longer wavelengths, the intensity measured by multiple smaller telescopes concurrently can be correlated, yielding measurements of the Fourier transform of the sky brightness. This interferometric technique is analogous to sampling the intensity measured by a telescope with a greater diameter.

A radio interferometer measures the Fourier transform, commonly referred to as the visibility function $V(u, v)$, of a target sky brightness distribution $I(l, m)$. Here, l and m are direction cosines with reference to the unit vector in the direction of the pointing center

of the array, and u and v describe the distances between the antennas in the plane of the array. For two antennas at positions $\mathbf{r}_1$ and $\mathbf{r}_2$, the measured visibility is defined as the correlation of the electric fields $\mathbf{E}(\mathbf{r})$ [107].

$$V(u, v) = \langle \mathbf{E}(\mathbf{r}_1)\mathbf{E}^*(\mathbf{r}_2) \rangle \tag{5.1}$$

For N antennas in an array, $\frac{N(N-1)}{2}$ correlations are measured, and the separation of the antenna elements in the plane of the array is referred to as the baseline length. Measurements of the visibility function are taken over the course of an observation, and the inverse Fourier transform can be taken to generate a map of sky brightness.

$$I(l, m) = \iint V(u, v)e^{-j2\pi(ul+vm)}dudv \tag{5.2}$$

The u and v coordinates are specified in units of wavelengths ($\lambda = c/\nu$) to arrive at the form shown in Equation 5.2.

$$\frac{\mathbf{r}_1 - \mathbf{r}_2}{\lambda} = [u, v, 0] \tag{5.3}$$

For practical observing, the inferred sky brightness distribution obtained from taking the Fourier transform of the unedited visibility function samples does not provide a good representation of the true emission from a celestial object, and the dataset needs to be edited. While modern arrays are designed with exacting specifications, the measured correlations between antennas can become corrupted by systematic or transient errors due to problems with antenna temperature and positioning, receiver electronics, radio-frequency interference, etc. Excepting sophisticated RFI excision algorithms, these problems must be flagged manually by the user and removed from the data set. Measured visibilities must also be calibrated based on observations of reference sources. The relationship between the

uncalibrated visibilities $\tilde{V}(t)$ and the true visibilities is given as

$$\tilde{V}(t) = G(t)V(t) + \epsilon(t) + \eta(t), \tag{5.4}$$

where $G(t)$ is the baseline-based complex gain, $\epsilon(t)$ is the baseline-based complex off-set, and $\eta(t)$ represents observation noise which is assumed to be wide-sense stationary over the course of an observation [108]. The baseline-based gains and offsets are dependent on the complex gains of the individual antennas which are determined empirically via observations of compact sources. Reference sources are also observed to calibrate the receiver passband and to determine an accurate absolute flux density measured at the array. While the bandpass and flux reference sources are observed at the start of the observation, the complex gain calibrator is observed periodically between observations of the science target to ensure that changes in the state of the atmosphere in the pointing direction are accounted for. For microwave observations, these periodic observations are normally sufficient to compensate for atmospheric variability, but at millimeter-wavelengths, atmospheric path-length variability will result in significant decorrelation on the order of minutes. This rapid decorrelation can be mitigated through a self-calibration procedure, wherein the complex antenna gains are set as free parameters and fit to a model (usually an initial image of the sky brightness). Self-calibration produces reliable results because the number of baseline correlations is greater than the number of antennas, and the problem is therefore overdetermined. After editing and calibration procedures have been applied to the dataset, the Fourier transform of the sample visibility function produces an image that is closer to the true sky brightness distribution. Since the number of array elements is finite, however, the visibility function is an incomplete sampling of the spatial frequencies corresponding to the source, and the effect of the sampling must be deconvolved from the inverted image. There is no unique solution to this deconvolution problem, but deconvolution algorithms rely on prior knowledge about the source to constrain the results. Following deconvolution, the derived sky brightness image can then be interpreted scientifically.

5.2   Explaining Prior Millimeter-wavelength Observations of Venus

Spatially resolved 2-3 millimeter-wavelength observations of Venus made prior to 2010 exhibit significant longitudinal brightness temperature variations on the order of 30-80 K, with the brighter regions appearing on the night side of the planet [28, 26, 27]. Due to the inherent difficulties associated with observing celestial sources at millimeter-wavelengths, it is possible that the brightness variations are artifacts of the imaging process. The Hat Creek observations of de Pater et al. [26] and the Owens Valley Radio Observatory observations of Shah et al. [28] were made with three elements in various arrangements over several days, and the observations of Sagawa [27] were made with the six element Nobeyama Millimeter Array. The use of fewer array elements requires longer observing times to obtain sufficient baseline coverage and increasing the likelihood of error due to atmospheric path length variations. If the apparent variations are not due to observing error, however, they must result from physical processes within the atmosphere of Venus. This argument is strengthened by more recent studies; the strength of Venus atmospheric convection near the lower cloud region is thought to be enhanced on the nightside [109], and evidence for significant nightside activity can be seen in infrared images from the Akatsuki IR2 instrument, showing atmospheric structures with sharp contrasts and similar spatial scales to the millimeter-wavelength observations [110]. If the atmospheric dynamics associated with these features are strong enough, they could perhaps cause significant variations in atmospheric composition as a function of longitude.

The radiative transfer model described in the previous chapter has been used to investigate the effects of varying atmospheric conditions on emission temperature. For comparison with the observations of Sagawa [27], a frequency of 103 GHz is used for forward model simulations. The radiative transfer model predicts a limb darkening of roughly 8 K from the center of the Venus disk to near the limb. While the temperature of the Venus atmosphere within the lower cloud altitude range will vary with longitude, the magnitude of

these changes is likely within 10 K and does not predict the spatial inhomogeneity observed in the radio images [111]. In addition, it is likely that the list of microwave absorbers considered in this model is exhaustive, and no unknown spatially-variable microwave absorber exists at a high enough concentration to affect the observable emission temperature. With this in mind, the following simulations explore the variations in abundance of three microwave absorbers: H_2SO_4 vapor, SO_2, and the liquid H_2SO_4 cloud aerosol. Variations in the abundances of these absorbers are explored numerically in the model by either scaling the abundance profiles by a constant value or shifting the abundances within different altitude ranges. The resulting brightness temperature predicted by the radiative transfer model for the displaced absorbers is recorded for comparison. The abundances of the absorbers are not linked through any thermochemical or dynamical model, and future work is needed to study the variations of these absorbers in the context of a mass transport model for the troposphere of Venus.

Sulfuric Acid Vapor Abundance

The baseline profile $P_{baseline}(h)$ for H_2SO_4 vapor abundance is the profile derived from the Magellan radio occultation experiment during orbit 3212 [41]. To simulate the effects of variations in the H_2SO_4 vapor abundance on observed brightness temperature, an additional abundance feature is added to this baseline profile. The abundance associated with this feature $P(h)$ is a function of the height h above the mean surface. Initially, $P(h)$ is defined using the saturation vapor pressure expression of Kolodner, reproduced in Equation A.1 [112]. p is the partial pressure of H_2SO_4 vapor in atmospheres, T_o is the reference temperature of 375 K, and T_c is the critical temperature of 910.5 K for H_2SO_4.

$$ln(p) = 10156 \left[-\frac{1}{T} + \frac{0.38}{T_c - T_o} \left(1 + ln\left(\frac{T_o}{T}\right) - \frac{T_o}{T} \right) \right] - \frac{\Delta F}{RT} + 16.259 \qquad (5.5)$$

This equation constrains the additional abundance of H_2SO_4 vapor given by $P(h)$ above 48 kilometers above the mean surface. It is assumed that no H_2SO_4 vapor is present below 48 kilometers for the initial generation of the $P(h)$ profile; this limitation does not apply for later modifications. A matrix of H_2SO_4 vapor profiles can be created by modifying this $P(h)$ profile as a function of height with a scale factor a and a shift factor h' and adding this term to the baseline abundance derived from the Magellan results. The addition of $P(h)$ simulates the effect of a large localized spike in H_2SO_4 vapor abundance.

$$\mathbb{P}_{ij} = a_i P\left(h - h'_j\right) + P_{baseline}(h) \tag{5.6}$$

Each profile generated through this shifting and scaling operation is used as an input to the radiative transfer model, and the resulting nadir brightness temperature is calculated. The effects on the brightness temperature derived from changing the abundance of H_2SO_4 vapor is summarized in Figure 5.1.

The scaling and shifting of the H_2SO_4 vapor profile through $P(h)$ in this figure is an exaggeration of what is physically feasible at Venus. Although the increase in mole fraction is consistent with the results of the Venus Express VeRa radio occultation experiment, the shifts in the location of peak abundance are not likely [102]. At higher altitudes, the abundance of H_2SO_4 vapor is constrained by the saturation vapor pressure expression, while at lower altitudes (below 40 km), thermal dissociation results in the breakdown of H_2SO_4 into SO_3 and H_2O vapor. However, Figure 5.1 shows that variations in H_2SO_4 vapor abundance would not directly explain the brightness temperature variations described by Sagawa [27], even including the exaggerated abundance profiles.

Sulfur Dioxide Abundance

Variations in brightness associated with changes in the SO_2 abundance are studied through scaling of features observed in the abundance profiles derived from the Vega landers at 44 and 52 kilometers (shown in Figure 4.11). The scaling of these profiles is performed by
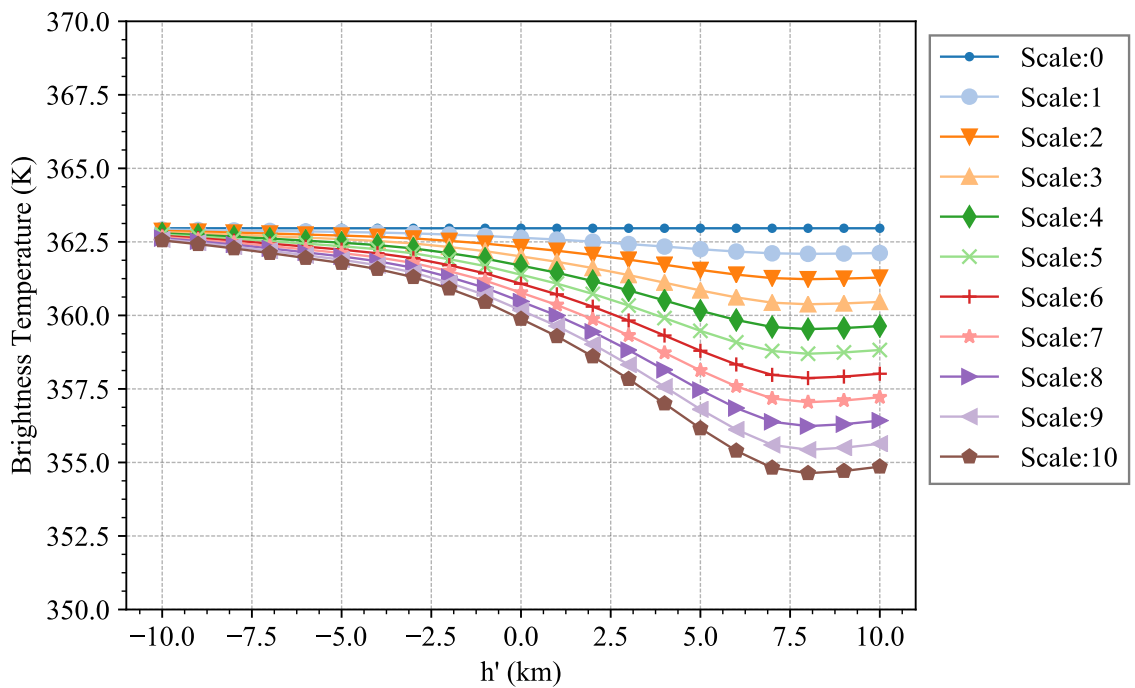
Figure 5.1: Nadir brightness variations at 103 GHz resulting from changes in H_2SO_4 vapor abundance. The abscissa gives the value of h' in Eq. 5.6, and the ordinate gives the resulting nadir brightness temperature predicted by the radiative transfer model. Each superimposed plot represents a different value of the scale factor a. A uniform SO_2 mole fraction below the cloud of 50 ppm and q a 50 mg/m^3 H_2SO_4 cloud are assumed.

establishing a vector x of mixing ratios for eight anchor altitudes. The constants a_{44} and a_{52} are used to scale the abundances at the corresponding altitudes.

$$\mathbf{x} = \left[x_0, x_{10}, x_{35}, x_{40}, a_{44}x_{44}, a_{52}x_{52}, x_{80}, x_{100}\right] \tag{5.7}$$

For altitudes between the anchor values, the mole fraction is calculated by power law expression with an interpolated scale height. This interpolation approximates the expected abundance between the anchor points.

$$P(h) = x_{lower}e^{-(h-h_{lower})/H} \tag{5.8}$$

$$H = \frac{h_{lower} - h_{upper}}{ln\left(x_{upper}/x_{lower}\right)} \tag{5.9}$$

The results of scaling the 44 and 52 kilometer abundances within the range of values retrieved from the Vega measurements is shown in Figure 5.2.

Figure 5.2 suggests that the spatial variation of SO_2 implied by the Vega lander results would be visible as spatial brightness temperature variations on the order of 25K at millimeter wavelengths.

Lower Cloud Bulk Density

The effect of orders of magnitude changes in the lower cloud bulk density has also been simulated using the microwave radiative transfer model. For the model inputs, it is assumed that the aerosol size distribution profile is similar to that retrieved by the Pioneer Venus probes, with a maximum aerosol radius below 25 microns [87]. H_2SO_4 liquid concentrations of 85% and 99% are used for the simulations. Modifications of the cloud bulk density are treated similarly to the H_2SO_4 vapor abundance profiles. The baseline profile consists of a region between 47 and 50 km populated by a cloud with a bulk density of 50 mg/m^3 in accordance with the Pioneer Venus profiles (see Figure 4.8 [87]. The bulk density
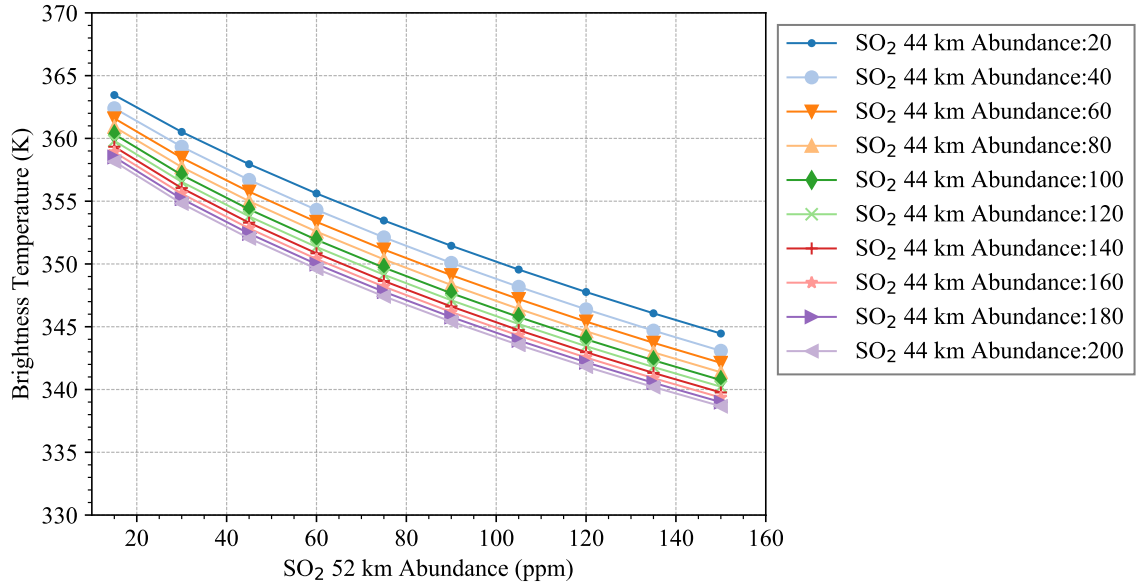
Figure 5.2: Nadir brightness variations at 103 GHz resulting from changes in SO_2 abundance. The abscissa gives the mole fraction of SO_2 at 52 kilometers, and the ordinate gives the resulting nadir brightness temperature predicted by the radiative transfer model. Each superimposed plot represents a different SO_2 mole fraction at 44 kilometers. The Magellan orbit 3212 H_2SO_4 vapor profile and a 50 mg/m^3 H_2SO_4 cloud are assumed.

profile is shifted and scaled by up to a factor of 10, and the brightness temperature is calculated for each element in the shift-scale matrix. The results of this analysis are presented in Figure 5.3.

As is the case with SO_2, substantial variations in the bulk density of the clouds could result in spatial inhomogeneity of the brightness temperature on the order of 35 K. It is unlikely, however, that the cloud bulk density would exceed 200 mg/m^3 [87], limiting the temperature variation to 15 K.

The results of these simulations suggest that substantial variations in atmospheric structure and composition in the lower cloud region could explain the observations of de Pater [26]. To explain the observations of Sagawa, however, the maximum variation of SO_2 and H_2SO_4 abundance, cloud bulk density, and temperature would need to occur; this is highly unlikely. Since H_2SO_4 vapor, aerosol, and SO_2 variations would all contribute to the variation in emission temperature, determination of atmospheric composition from observations
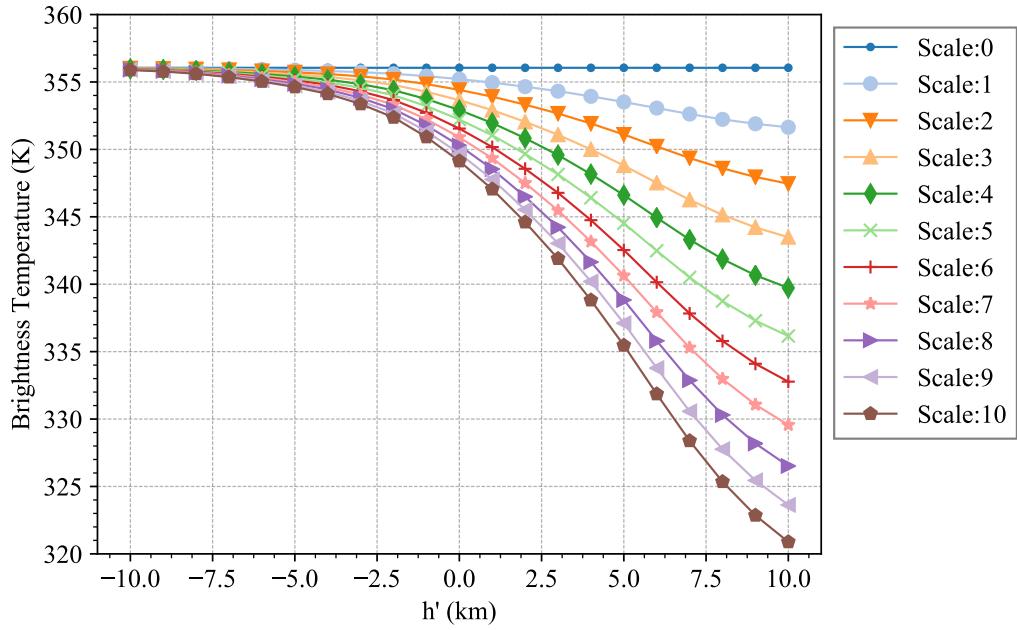
(a)
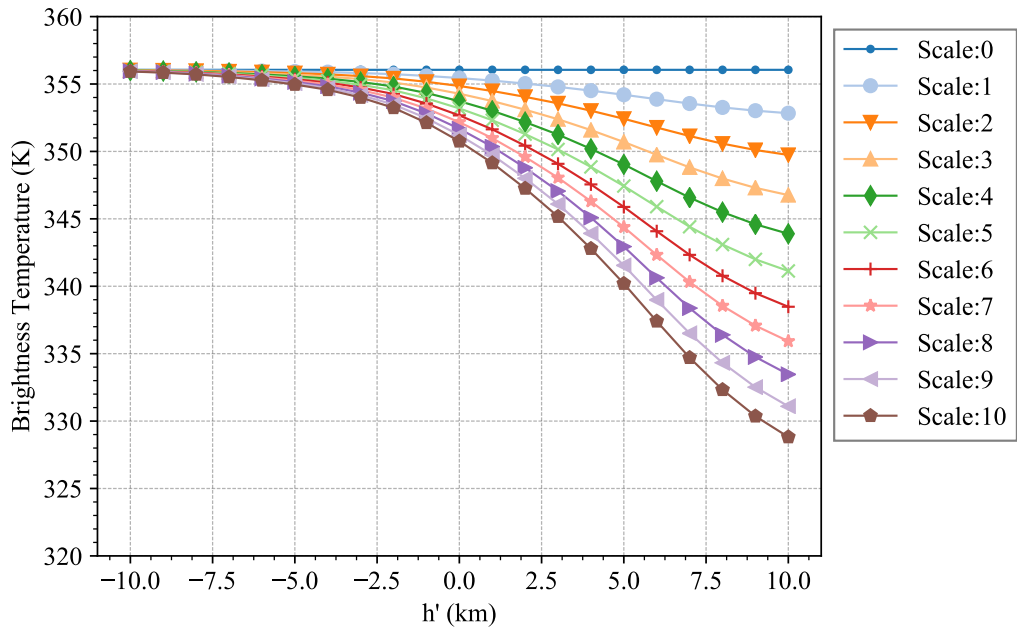
(b)

Figure 5.3: Nadir brightness variations at 103 GHz resulting from changes in cloud bulk density for a cloud consisting of (a) 85 % H_2SO_4 and (b) 99% H_2SO_4 aerosols. The abscissa gives the altitude shift value h' (as similarly used in Eq. 5.6), and the ordinate gives the resulting nadir brightness temperature predicted by the radiative transfer model. Each superimposed plot represents a different value of the cloud bulk density scale factor. A uniform SO_2 mole fraction below the cloud of 50 ppm and the Magellan orbit 3212 H_2SO_4 vapor profile are assumed.

of the millimeter-wavelength emission of Venus is an ill-posed problem. This can be mitigated through observations at multiple wavelengths. Figures 5.4 and 5.5 show the effect of varying SO_2 abundance and cloud bulk density on the observed brightness temperature at different frequencies.
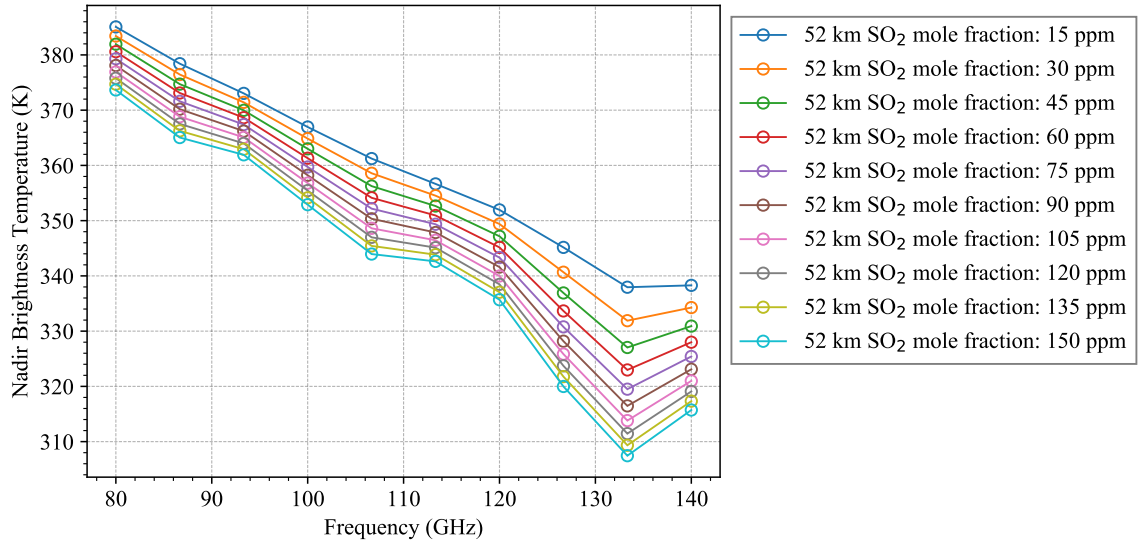
Figure 5.4: The effect of scaling the 52 km mixing ratio of SO_2 on the brightness temperature for 80 to 140 GHz emission.

Continuum observations between 130 and 135 GHz are particularly sensitive to changes in the abundance of SO_2. In general, the brightness temperature decreases associated with a higher SO_2 abundances has a greater dependence on frequency.

These radiative transfer model simulations suggest that significant longitudinal variations in emission temperature at Venus could be possible, but they do not address the question of error incurred during observations. In the years since the observations of de Pater and Sagawa, more powerful millimeter-wavelength interferometers have been developed: the Combined Array for Research in Millimeter-wavel Astronomy (CARMA), and the Atacama Large Millimeter/submillimeter Array (ALMA) [113, 114]. ALMA in particular has provided unprecedented low-noise imaging capabilities and significant spatial and spectral resolution to the astronomical community. The remainder of this chapter will
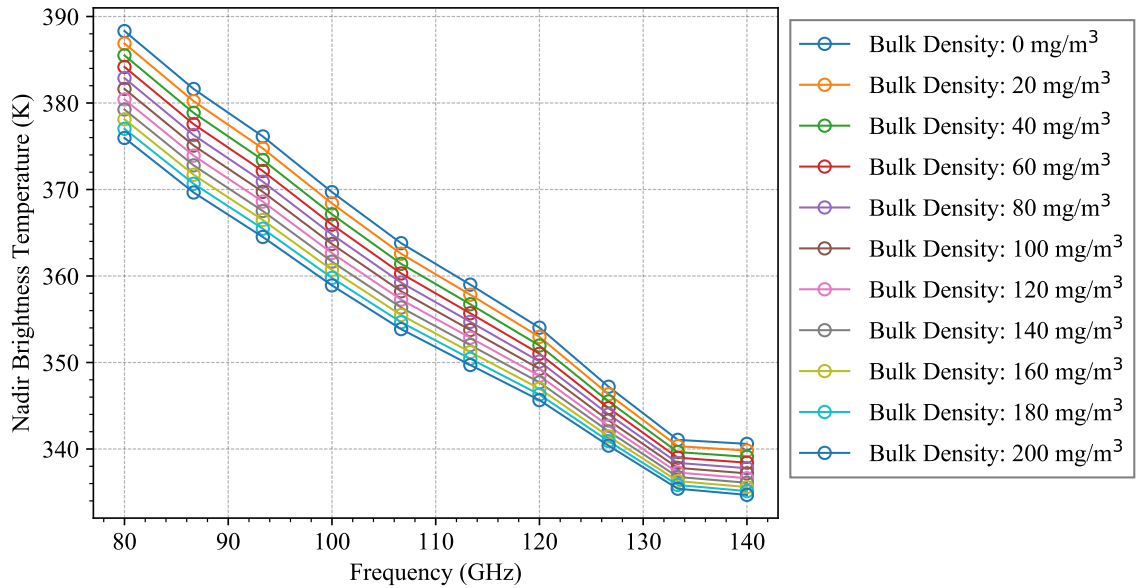
Figure 5.5: The effect of scaling the lower cloud bulk density on the brightness temperature for 80 to 140 GHz emission.

present an analysis of Venus observations made with CARMA and ALMA.

5.3 CARMA Observations

Venus was observed using CARMA between October and November of 2013 when the planet was near eastern elongation. CARMA, which has since ceased operation, was a heterogenous millimeter interferometer located at Cedar Flat, California composed of 23 antennas from the Owens Valley Radio Observatory (OVRO, six 10.4 meter dishes), the Berkeley-Illinois-Maryland Array (BIMA, nine 6.1 meter antennas), and the Sunyaev-Zel'dovich Array (SZA, eight 3.5 meter antennas) [113]. The SZA elements were primarily used to study extended emission, and only the OVRO and BIMA antennas were used for the observations discussed here. CARMA observed Venus in the 3 millimeter band in the C array configuration with a maximum baseline length near 350 meters for seven non-consecutive days. Within the 3 millimeter-wavelength band, 12 continuum windows total were observed within the lower sideband (99-101.5 GHz) and the upper sideband (112-

114.5 GHz). These continuum windows had bandwidths of 487.5 MHz and channel widths of 12.5 MHz. Narrowband data was also taken in the range of the $J = 1 \rightarrow 0$ CO line, which is not discussed further here. Each observation begins with a 5 minute observation of a flux calibrator followed by 10 minute observation of a bandpass calibrator. Venus is then observed for 15 minute intervals with intervening 3 minute observations of the antenna gain calibrator. For all scans, source integration times are 30 seconds.

While CARMA observations are calibrated by switched measurements of a temperature controlled ambient load, atmospheric turbulence and variations in water vapor abundance along the line of sight of the observing target can result in significant phase excursions for the measured visibilities; this is further exacerbated for the low elevation observations of Venus described here [115]. Weather monitoring at the CARMA site enables evaluation of observation quality, and three datasets (observed on October 19th, October 31st, and November 12th) from the observing campaign were determined to be suitable for imaging. Table 5.2 gives the ephemeris of Venus and other relevant information for these observation dates. Figure 5.6 shows the apparent Venus disk and the uv-coverage for all CARMA observation dates.

Observation Date	October 19	October 31	November 12
Distance from Earth	0.769 AU	0.677 AU	0.586 AU
Sub-Earth Latitude	4.1°	4.3°	4.2°
Sub-Earth Longitude	174.9°	205.1°	234.5°
Phase	0.557	0.500	0.435
Angular Diameter	21.7"	24.7"	28.5"
Apparent Max. Elevation	27.35°	25.92°	25.92°
Observing Times	22:00 - 25:24	21:20 - 25:05	19:20 - 25:05
Bandpass Calibrator	J1337-129	3C273	J1137-129
Flux Calibrator	MWC349	MWC349	Mars
Antenna Gain Calibrator	J1733-1304	J1733-1304	J1733-1304
Atmospheric Opacity (τ)	0.12	0.14	0.25
Mean RMS path errors	174 μm	193 μm	273 μm

Table 5.1: Venus ephemeris and observation details for the CARMA observation dates in 2013. Times exceeding 24:00 represent the following day.
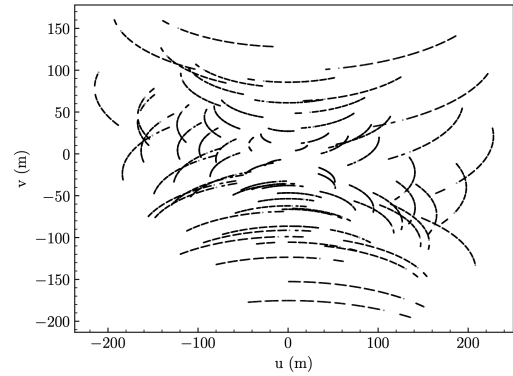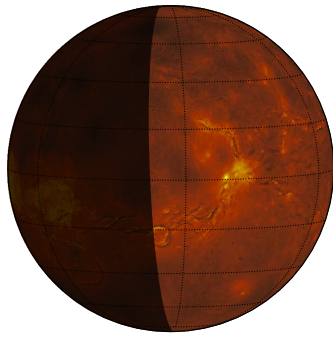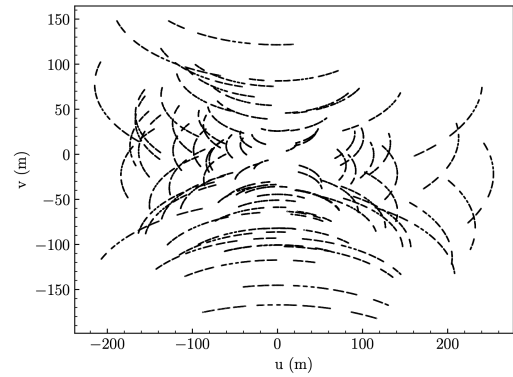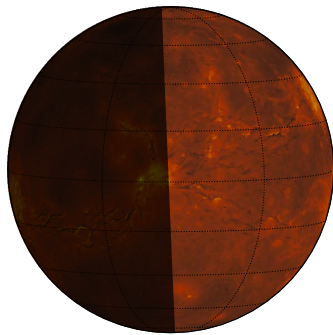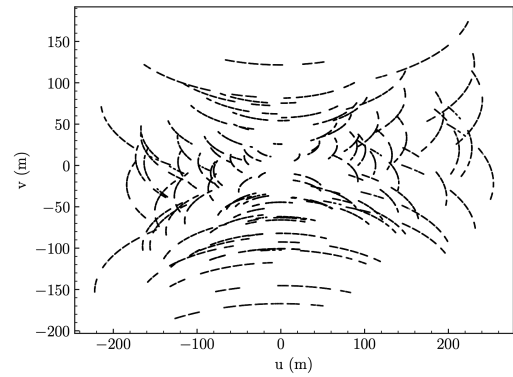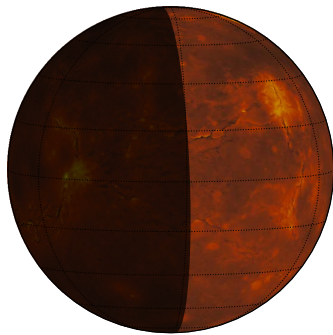
Figure 5.6: Venus viewing orientation and baseline coverage for CARMA observations on (a) Oct. 19, 2013, (b) Oct. 31, 2013, (c) Nov. 12, 2013. Venus topography data from the Magellan Global Topography Data Record [99].

5.3.1 ALMA Observations

The dayside of Venus was observed using ALMA on the afternoons of March 3rd and 13th, 2016. Compared to its predecessors (including CARMA), ALMA represents an order of magnitude improvement in millimeter-wavelength interferometric capabilities. ALMA is comprised of 66 elements, 50 of which comprise the primary 12 meter array. The remaining antennas form the Atacama Compact Array (ACA), which are not included in the observations presented here. Like the SZA elements of CARMA, the ACA is primarily used to study emission from extended sources. For the Venus observations, 30-35 of the antennas from the 12 meter array were used. In addition to the increased number of antenna elements, the performance of ALMA is greatly enhanced by the relative atmospheric stability of the Chajnantor Plateau array site in the Atacama Desert of Chile. During this campaign, Venus was observed in the C36-2/3 configuration with a maximum baseline length of 460 meters using the ALMA Band 3 (84-116 GHz) and Band 4 (125-163 GHz) receivers configured with sideband bandwidths of 2 GHz and individual channel widths of 15 MHz. For the Band 3 data, the lower and upper sideband (LSB and USB) center frequencies were 85 and 99 GHz, and the LSB and USB center frequencies for the Band 4 data were 131 and 145 GHz. While only Band 4 data was collected on March 3rd, both Band 3 and Band 4 data were collected on March 13th. Narrowband data in the range of the OCS $J = 7 \rightarrow 6$, $J = 8 \rightarrow 7$, $J = 11 \rightarrow 10$, and $J = 12 \rightarrow 11$ transitions were also taken during these observations and are not discussed here. Each ALMA observation begins with a 6 minute observation of a bandpass calibrator followed by a 3 minute observation of a flux calibrator. Venus is then observed for 6.5 minute intervals with intervening 30 second observations of the antenna gain calibrator. For all scans, source integration times are 6 seconds. During the observations, the water vapor content of the Earth's atmosphere is monitored using a water vapor radiometer mounted on each antenna, and 15 second measurements of an ambient and a hot thermally-controlled reference source are made every 15 minutes. These measurements can be used to generate antenna-based atmospheric path length and system

114

temperature corrections to the visibility data.

In addition to dedicated scientific observations, Venus has also been observed as a flux calibrator for ALMA. While most often used as a flux calibrator for observations with the Atacama Compact Array (ACA), Venus was used to calibrate shorter baseline configurations of the 12-meter array for three observations on December 6th and December 7th, 2014. The two Venus flux calibrator measurements on December 6th, 2014 in support of an Sgr B2 study [116] were made within an hour and a half of each other, and these two measurements were combined into a single dataset to be used for imaging. ALMA was arranged in the C34-1/2 configuration with a maximum baseline length of 349 meters, and the Band 3 receiver was configured to measure two 4 GHz sidebands from 88-92 GHz and from 100-104 GHz with individual channel widths of 244 kHz. Between both observations, Venus was observed for 5 minutes using 6 second integrations. Table 5.2 gives the ephemeris of Venus and other relevant information for both ALMA observations, and Figures 5.7 shows the apparent Venus disk and the uv coverage for the ALMA observation dates.

Observation Date	December 6 (2014)	March 3 (2016)	March 13 (2016)
Distance from Earth	1.674 AU	1. 505AU	1.546 AU
Sub-Earth Latitude	1.73°	0.37°	0.47°
Sub-Earth Longitude	79.93°	85.41°	112.26°
Phase	0.984	0.913	0.929
Angular Diameter	9.96"	11.08"	10.79"
Apparent Max. Elevation	72.5°	67.9°	76.4°
Observing Start Times	14:12, 15:40	16:28	12:58, 14:15
Bandpass Calibrator	J1700-2610, J1733-1304	J2148+0657	J2258-2758
Flux Calibrator	J1733-104	Neptune	Neptune, Pallas
Antenna Gain Calibrator	J1744-3116	J2146-1525	J2224-1126

Table 5.2: Venus ephemeris and observation details for the ALMA observation dates.
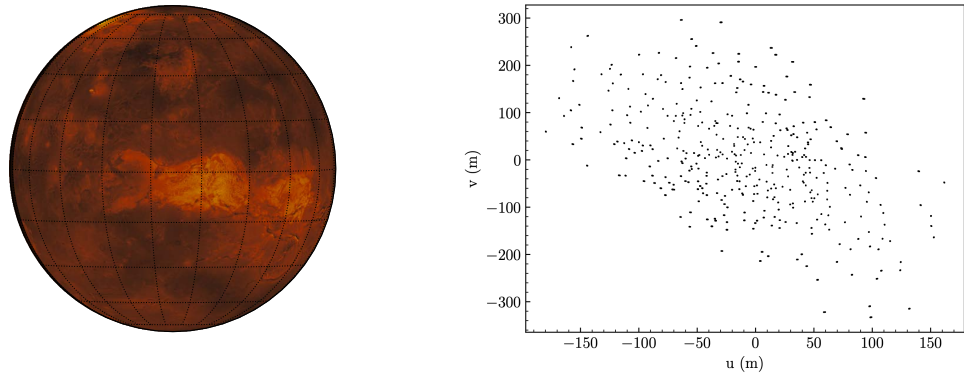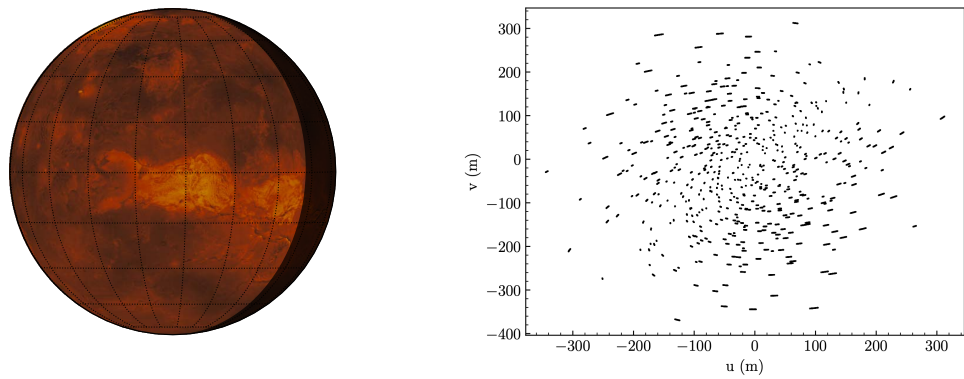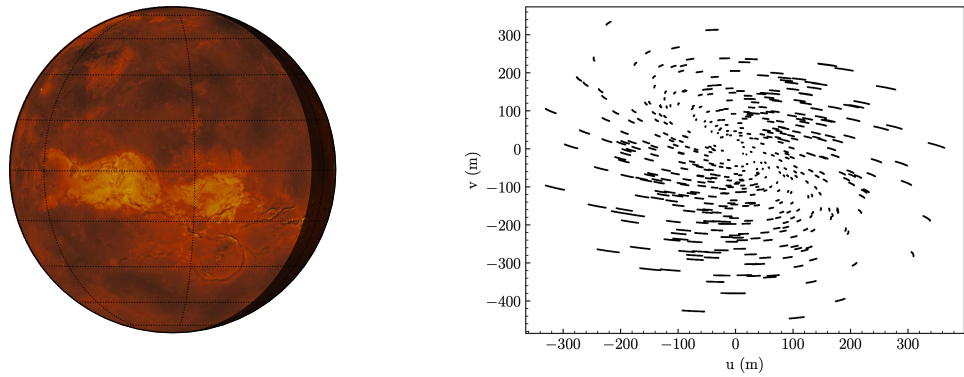
Figure 5.7: Venus viewing orientation and baseline coverage for ALMA observations on (a) Dec. 06, 2014, (b) Mar. 03, 2016, (c) Mar. 13, 2016. Venus topography data from the Magellan Global Topography Data Record [99].

5.4   Data Reduction and Imaging

5.4.1   Editing and Calibration

Prior to imaging, the observed visibility data were edited and calibrated using the Combined Astronomy Software Applications (CASA) package [117]. Flagging was initially performed to remove shadowed antennas, zero-flux measurements and edge channels before inspection of the data, and further flagging was performed at various stages of calibration to remove poor data points. For the ALMA observations, the computed antenna-based system temperature and water vapor radiometer calibrations are applied to the visibilities. For all datasets, antennas with anomalously high system temperatures are flagged before further processing.

Following initial editing, line length and bandpass calibrations are applied to the visibility data to minimize phase variations across the channels comprising the continuum windows. The bandpass calibrated continuum windows are then divided into 500 MHz bandwidth blocks, and these blocks are channel-averaged to increase the signal-to-noise ratio of the observations. Antenna-based amplitude and phase calibrations are then applied to the data from the gain calibrator observations, followed by amplitude scaling from measurements of the flux calibrator. For extrasolar flux calibrators, a point source structure is assumed, and measurements of the Stokes parameters are made periodically by the observing array. Due to day-to-day emission variabilities of these cosmic sources and uncertainties in the measurements themselves, these flux calibrators are considered to be accurate on the order of 15% for CARMA and 10% for ALMA. If the flux calibrator is a solar system body, the emission intensity is determined using models derived from prior observations and radiative transfer simulations [118], and the accuracy of these flux scales are estimated to be on the order of 5% [119]. Solar system objects were used as flux calibrators for the November 12th, 2013 CARMA measurements and for all dedicated Venus observations with ALMA. For the October 19th and October 31st, 2013 CARMA observa-

tions, flux scaling based on observations of the MWC349 star system resulted in inaccurate emission intensity estimations. For these observation dates, the antenna gain calibrator J1733-1304 (a blazar, or active galactic nucleus with a relativistic jet) was used as the flux reference. The Stokes I intensity was determined within 7% for both observation dates as $I = a \left(\nu / \nu_0 \right)^{b + c \cdot log(\nu / \nu_0)}$ where $a = 2.41 \pm 0.17$, $b = -0.80 \pm 0.17$ and $c = 0.27 \pm 0.15$. The reference intensity a is the average recorded intensity at 103 GHz at in the CARMA archive from a period spanning September to December 2013, and the frequency dependence was determined via fitting the b and c parameters using 2013 archive measurements at 31.4 GHz, 103 GHz, and 227 GHz. For the ALMA observations, an accurate measure of the absolute flux density was unable to be obtained due to systematic errors in the system temperature calibration procedure for the observation of bright extended sources (Sagawa, personal communication). After all source calibrations are applied, an initial image of Venus is made and used as the starting model for an iterative phase self-calibration procedure which concludes with a single amplitude and phase self calibration.

Figure 5.8 illustrates the difference between the uncalibrated and calibrated datasets via comparison of the real part of the visibilities for a CARMA mid-band channel (100.2 GHz).

(a)   (b)
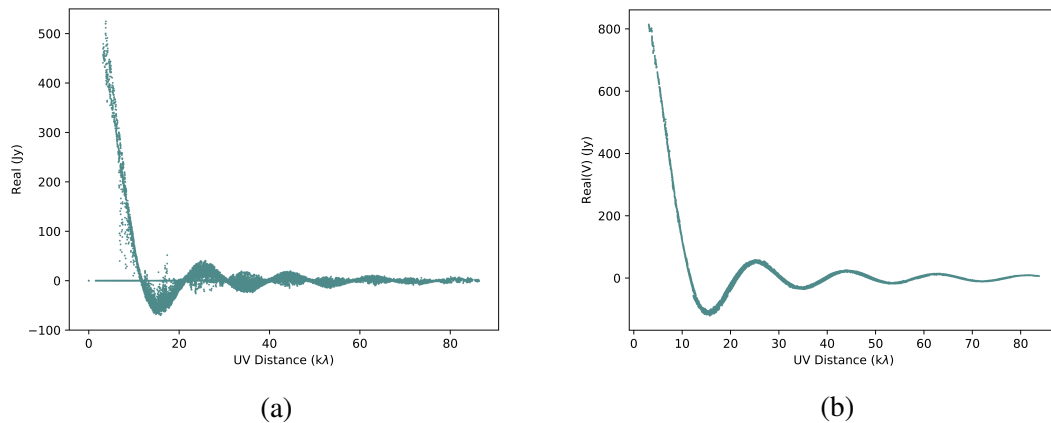
Figure 5.8: Real part of the visibilities for the (a) uncalibrated and (b) calibrated datasets from the 100.2 GHz channel of the CARMA observations on October 19, 2013

When compared with the uncalibrated dataset, the real part of the calibrated dataset bears closer resemblance to that of a limb-darkened disk. Equation 5.10 describes the visibility structure of a limb-darked disk, where R is the apparent radius of the disk in radians, u and v are projected baseline separations in wavelengths, $q = 1 + p/2$ for limb darkening parameter p, $\Gamma(z)$ is the Gamma function, and $J_q(z)$ is the Bessel function of the first kind and order q [120].

$$V(\beta) = V_o \Lambda_q(2\pi\beta) \tag{5.10}$$

$$\Lambda_q(z) = \Gamma(q+1) \left(\frac{1}{2}z\right)^{-q} J_q(z) \tag{5.11}$$

$$\beta = R\sqrt{u^2 + v^2} \tag{5.12}$$

A limb-darkened disk model was fit to the calibrated visibility dataset for all observations, including V_o, p and R as free parameters to obtain the best fit. The calibrated visibility data and the best fit model for mid-band windows of all observations are given in Figures 5.9-5.12

For the CARMA visibility samples shown in Figure 5.9, the magnitude of the residuals between the data and model are lowest for the October 19, 2013 observation, as the atmospheric opacity and mean rms path errors were lowest for this date. Accordingly, the visibility data for the November 12, 2013 observation, with higher atmospheric opacity and path length errors, shows greater deviation from the model. With the exception of the observations on March 3, 2016, The ALMA visibility samples shown in Figures 5.10-5.12 also show agreement with the limb darkened disk model.
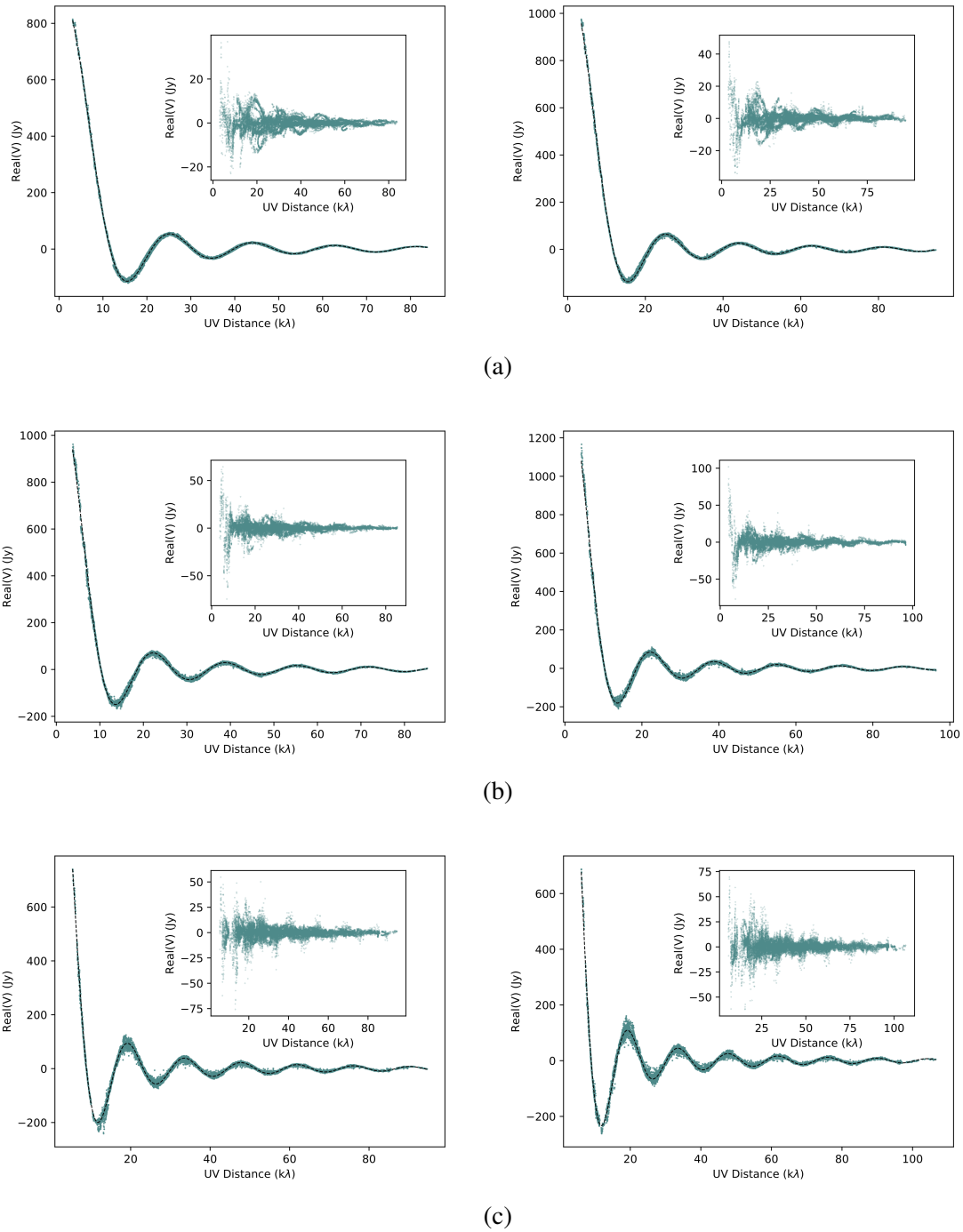
Figure 5.9: Mid-band (100.2 GHz channel on the left and 113.3 GHz channel on the right) calibrated visibilities and best fit models for CARMA observations on (a) Oct. 19, 2013, (b) Oct. 31, 2013, (c) Nov. 12, 2013. Inset plots show the residuals after the best fit model is subtracted from the data.
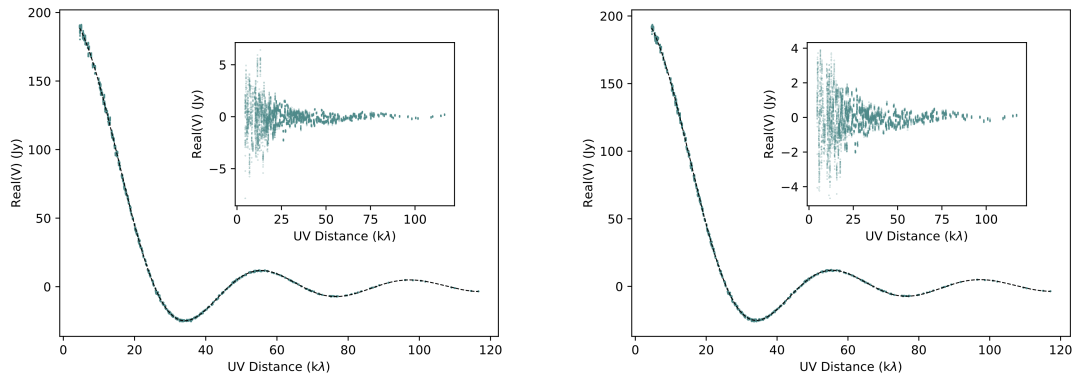
(a)

Figure 5.10: Mid-band (90.2 GHz channel on the left and 102.2 GHz channel on the right) calibrated visibilities and best fit models for ALMA observations on Dec. 6, 2014. Inset plots show the residuals after the best fit model is subtracted from the data.
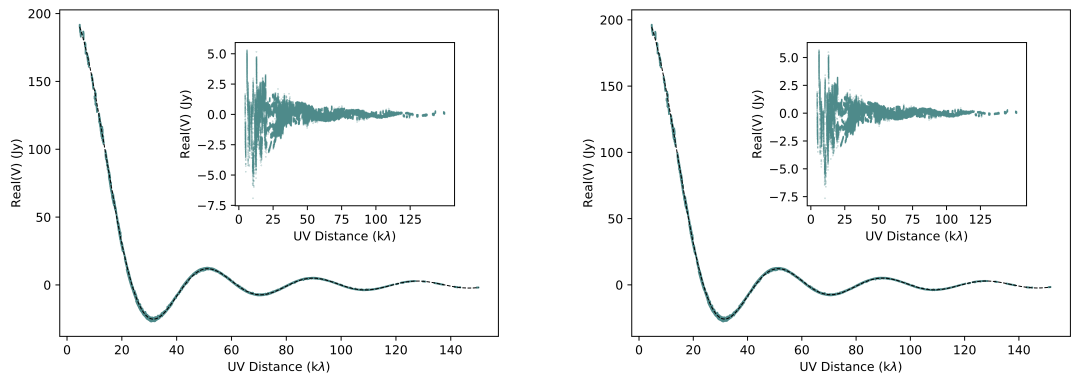
(a)

Figure 5.11: Mid-band (85.2 GHz channel on the left and 98.7 GHz channel on the right) calibrated visibilities and best fit models for Band 3 ALMA observations on Mar. 13, 2016. Inset plots show the residuals after the best fit model is subtracted from the data.
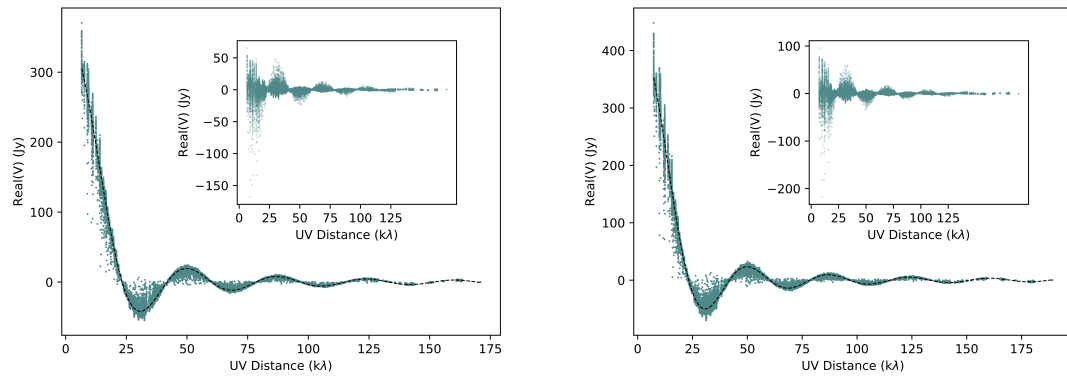
(a)
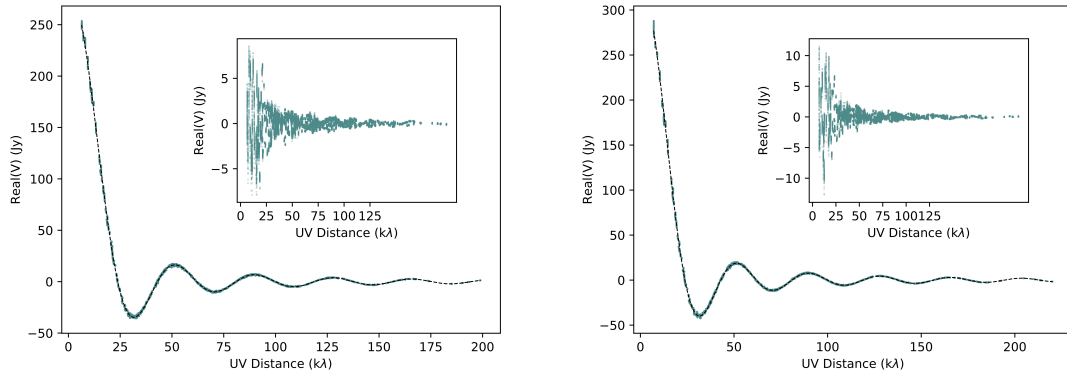
(b)

Figure 5.12: Mid-band (130.9 GHz channel on the left and 144.8 GHz channel on the right) calibrated visibilities and best fit models for Band 4 ALMA observations on (a) Mar. 3, 2016, (b) Mar. 13, 2016. Inset plots show the residuals after the best fit model is subtracted from the data.

122

5.4.2   Imaging

Following calibration, the observation data can then be used to generate images of emission from Venus. The best fit limb darkened disk visibility curve is specified as a starting model which is subtracted from the data, and the visibilities are weighted using the Briggs scheme with a robustness parameter of 0.0 [121]. CASA supports imaging with heterogeneous arrays by allowing the specification of primary beam models for each array element, and models for the OVRO and BIMA antennas comprising CARMA as well as models for the ALMA antennas are specified within the program. Since the spatial sampling of the u-v plane is inherently incomplete for interferometric operations, the image generated through direct Fourier inversion of the visibility data is a "dirty" image, representing the true sky brightness convolved by a configuration-dependent synthesized beam. Down to the half power point, the synthesized beam can be described as an elliptical Gaussian function, and the beam parameters for each observing campaign are given in Table 5.3.

Table 5.3: Table of synthesized beam parameters

Beam Parameter	CARMA	Dedicated ALMA	ALMA flux calibration
Major axis FWHM (arcsec)	3.2"-3.6"	1.2"-2.0"	3.7"-4.1"
Minor axis FWHM (arcsec)	1.7"-2.0"	0.95"-1.5"	1.6"-1.8"
Rotation (degrees)	5°-20°	79.9°-87.2°	67.6°-67.9°

A deconvolution process must be implemented to remove the effect of incomplete aperture sampling and create a realistic interpretation of the sky brightness at the time of the observation. The CLEAN algorithm is used here, which iteratively subtracts the point spread function of delta functions representing the brightest pixels in the image [122]. A finite support can be established beyond which CLEAN does not operate. This finite support is specified as a circle with a radius equal to that of Venus during the observation plus four arcseconds, which is the upper bound of the largest dimension of the synthesized beam. The locations of the brightest pixels are then added to the starting model. Following the

conclusion of the CLEAN procedure, this model is convolved with the point spread function, or CLEAN beam, and the residuals between the dirty image and the model are added in to form the final image. Illustrations of the model, CLEAN beam, residuals, and final image are shown in Figure 5.13 for the CARMA October 13, 2013 observations.

(a) Derived CLEAN components and model image

(b) Synthesized beam

(c) Residuals from imaging process

(d) Disk Image
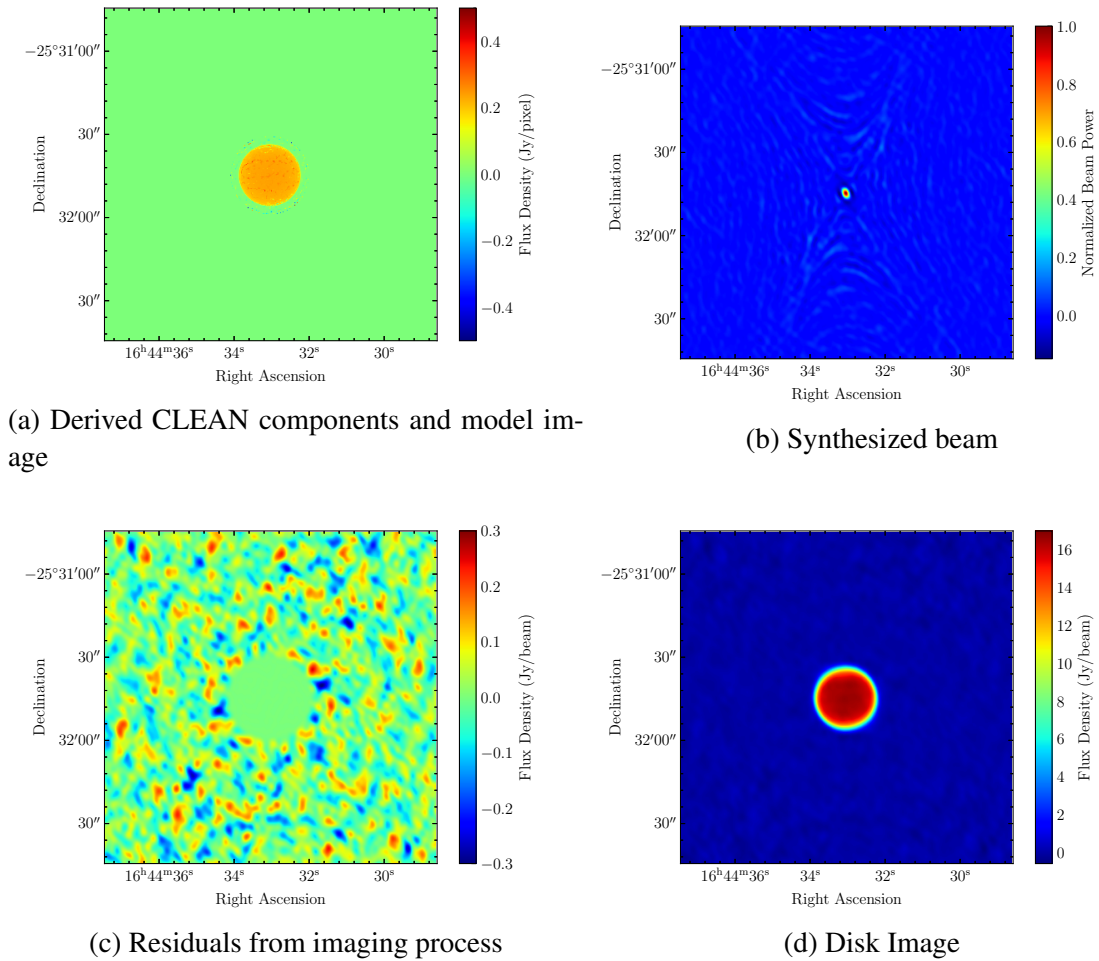
Figure 5.13: Illustration of the CLEAN deconvolution process using the CARMA Oct. 19, 2013 observation

For the initial images of Venus (prior to self calibration), the threshold for termination of the CLEAN process is set to 800 mJy, as a lower threshold would result in introduction of artifacts into the self-calibration model. The phase self-calibration procedure is then performed iteratively with successively lower CLEAN thresholds, as illustrated in Figure

5.14
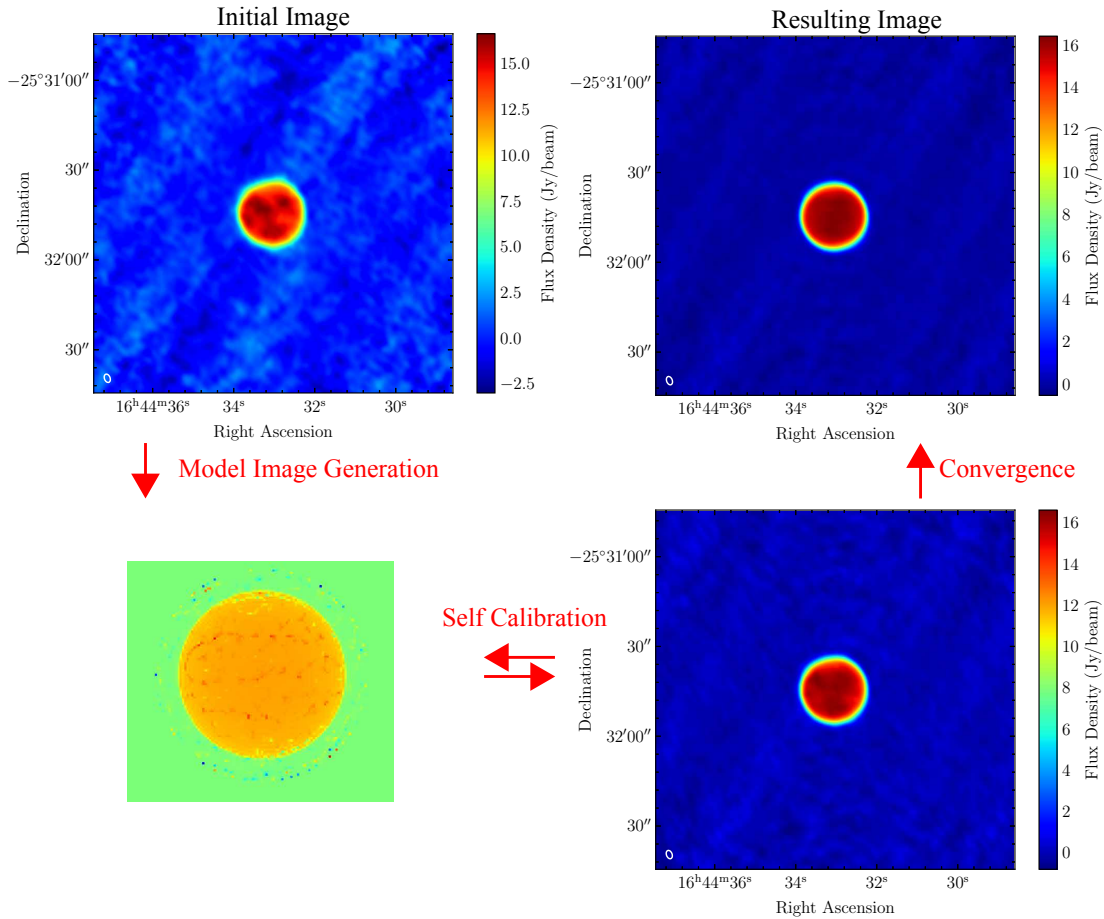
Figure 5.14: Steps in a self-calibration procedure.

For the final images, the CLEAN threshold is lowered to 2-20 mJy depending on the data quality and a single amplitude and phase self-calibration step is applied. This process is used to generate two types of images for analysis. The first category is a "coarse" image that is made for each averaged spectral window with a pixel length of roughly 5 pixels across the smallest dimension of the synthesized beam that is used to investigate the variation in flux with wavelength across the 3 millimeter band. The second category is a "fine" image made using multi-frequency synthesis for each sideband with a smaller pixel length of 0.02-0.05". The fine image, which integrates over the lower and upper sidebands,

125

is used to further reduce the image noise.

The noise within the image is estimated by taking the rms value of emission outside of the CLEAN finite support region for the phase self-calibrated images. The results are shown in Table 5.4.

Table 5.4: RMS noise for source-free regions in CARMA and ALMA images

Array	Date	Center Frequency	Source-free Noise
CARMA	Oct. 19, 2013	100.5 GHz	3.6 K
		113.5 GHz	2.2 K
	Oct. 31, 2013	100.5 GHz	4.3 K
		113.5 GHz	3.6 K
	Nov. 12, 2013	100.5 GHz	4.1 K
		113.5 GHz	3.9 K
ALMA	Dec. 6, 2014	90.3 GHz	0.48 K
		102.3 GHz	0.67 K
	Mar. 3, 2016	131 GHz	2.4 K
		145 GHz	4.0 K
	Mar. 13, 2016	85 GHz	0.40 K
		99 GHz	0.68 K
		131 GHz	2.0 K
		145 GHz	2.8 K

For the 3 millimeter-wavelength observations, the source-free noise in the ALMA images is an order of magnitude lower than the CARMA images. The 2 millimeter band is less atmospherically transparent, and the noise performance is comparable to the 3 millimeter CARMA observations

5.5 Images of Venus

Figure 5.15 shows the brightness temperature image of Venus derived from the imaging process for a selection of the CARMA and ALMA observations.
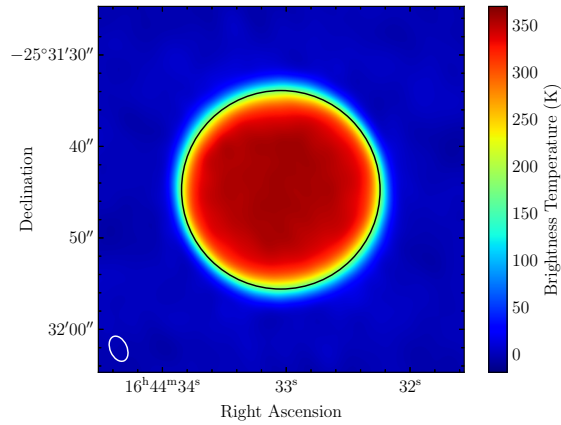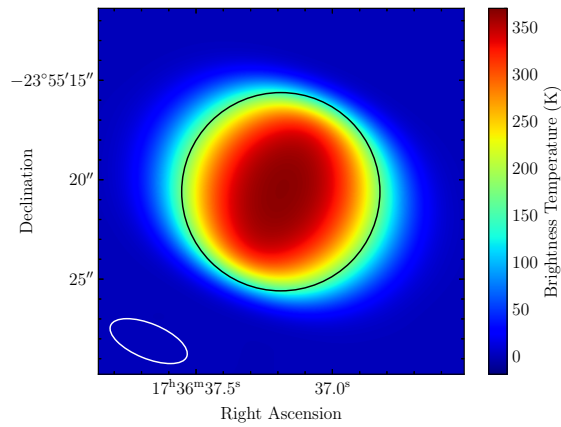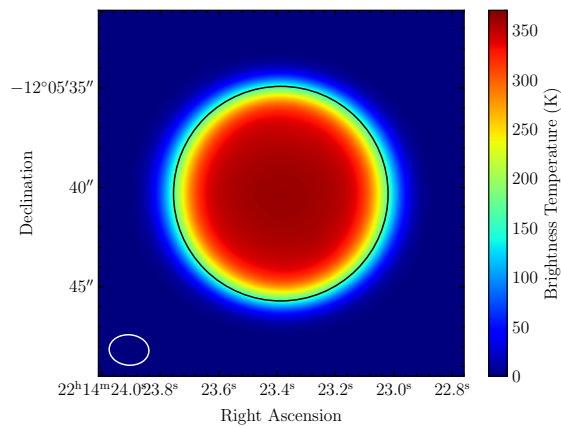
Figure 5.15: Brightness temperature images of Venus from (a) CARMA Oct. 19, 2013 at 100.5 GHz, (b) ALMA Dec. 6, 2014 at 90.3 GHz, (c) ALMA Mar. 13, 2013 at 99 GHz

The spatial variations in brightness temperature across the Venus disk can be more easily observed by subtracting the starting limb darkened disk model from the images. These residuals are shown for the CARMA and ALMA observations in Figures 5.16-5.18. In these figures, the primary beam (or the effective point spread function) is shown in the bottom left hand corner.

The CARMA images in Figure 5.16 all show longitudinal spatial variations in emission temperature, including bright regions on both the day and nightside of the planet. However, there are significant regions of emission appearing beyond the edge of the Venus disk, indicating that these spatial variations are likely the result of non-stochastic noise in the observation. The October 19th, 2013 observations, which were observed under the best conditions, shows clear evidence of polar darkening in agreement with prior VLA observations [23]. With the exception of the March 3, 2016 observations, the ALMA images in Figures 5.17 and 5.18 show little emission beyond the Venus disk. Polar darkening is also observed in these images, and although longitudinal variations can be observed, they appear to be largely dependent on emission angle. This is likely the result of the assumption of uniform limb darkening for the subtracted model.

The ALMA images in Figures 5.17 and 5.18 suggest that 2-3 millimeter continuum emission from the dayside of Venus can be well-modeled with a radiative transfer model assuming only latitudinal variations in composition and thermal structure. While the CARMA images appear to be noise-limited, an upper bound for day-night variations in emission temperature can be determined by taking the difference of the maximum and minimum observed emission temperature as a function of latitude. This is shown in Figure 5.19 for the three observing days.
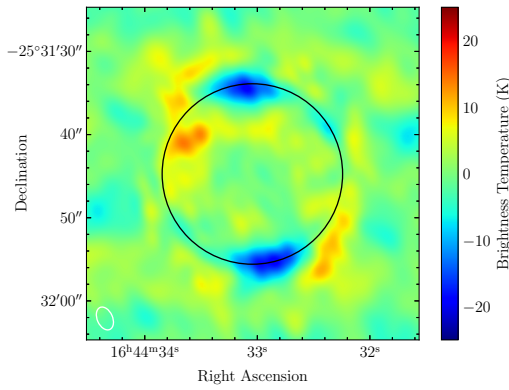
(a) Oct. 19th, 2013 at 100.5 GHz
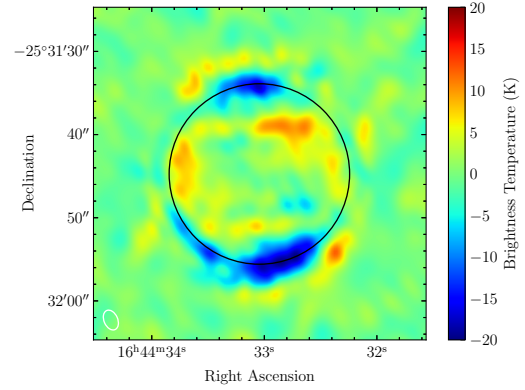
(b) Oct. 19th, 2013 at 113.5 GHz
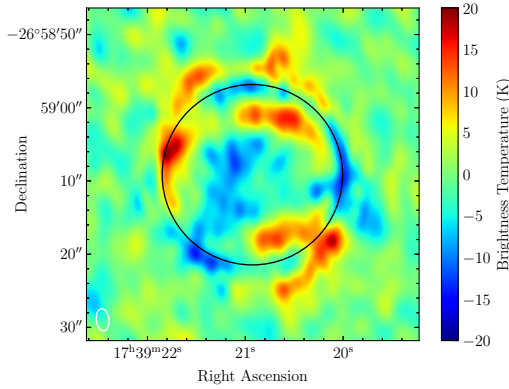
(c) Oct. 31st, 2013 at 100.5 GHz
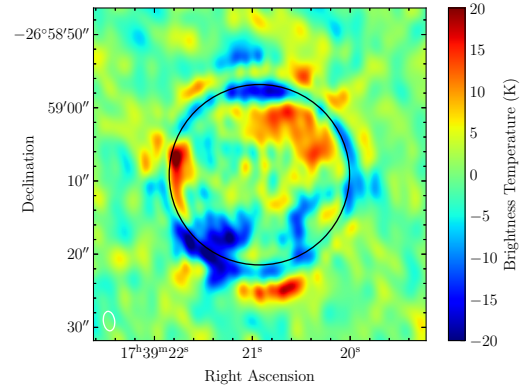
(d) Oct. 31st, 2013 at 113.5 GHz
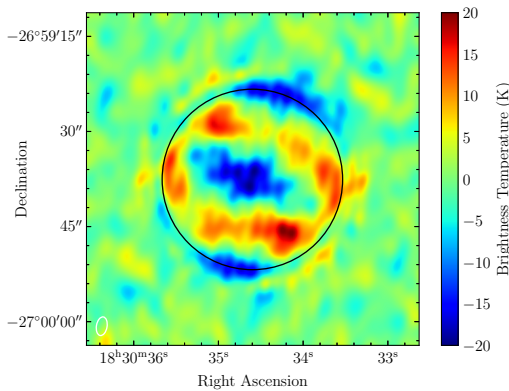
(e) Nov 12th, 2013 at 100.5 GHz
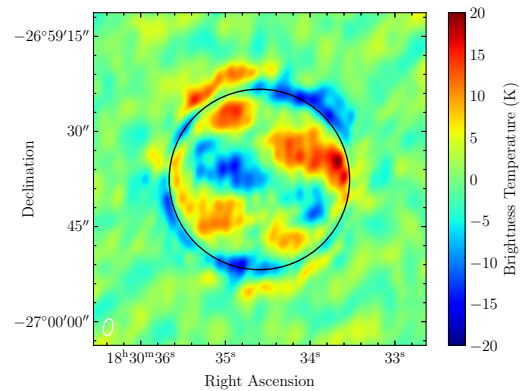
(f) Nov 12th, 2013 at 113.5 GHz

Figure 5.16: Residual brightness temperature maps for the CARMA observations
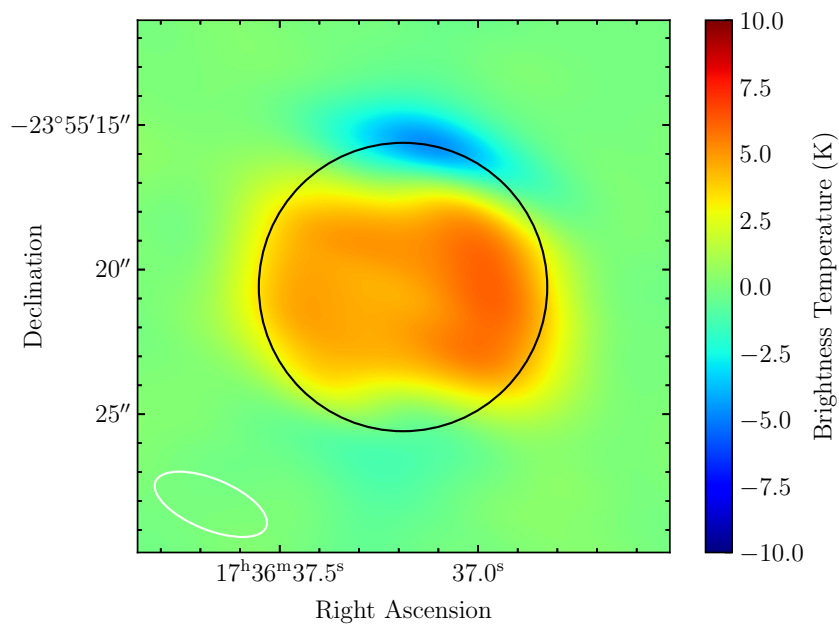
(a) Dec. 6th, 2014 at 90.3 GHz
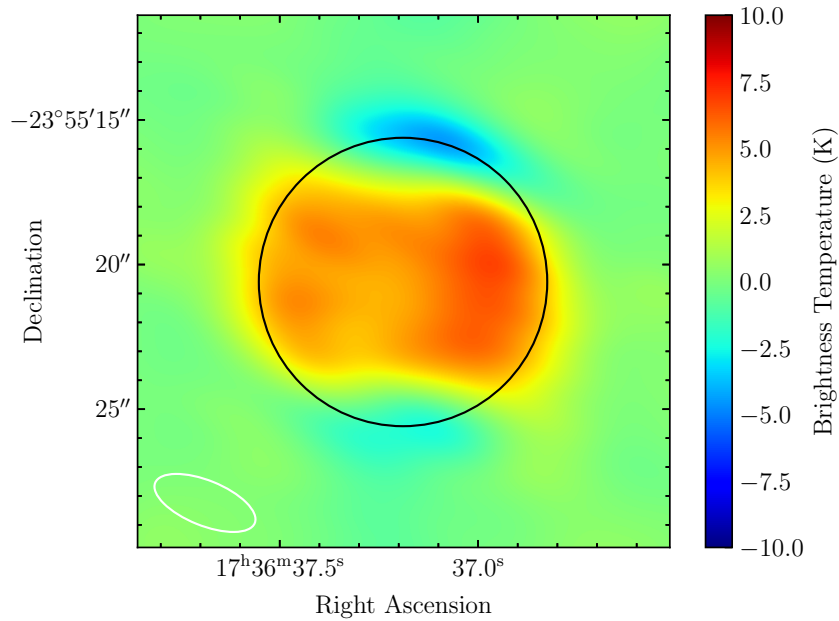
(b) Dec. 6th, 2014 at 102.3 GHz

Figure 5.17: Residual brightness temperature maps for the ALMA observations of Venus as a flux calibrator
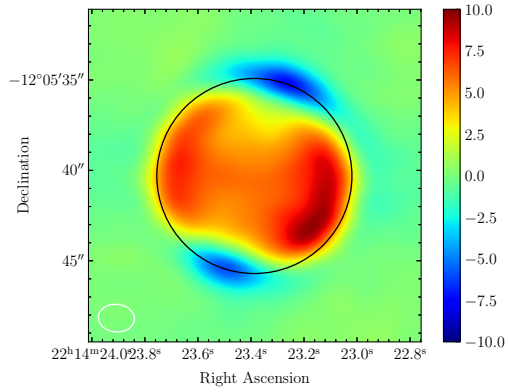
(a) Mar. 13th, 2016 at 85 GHz
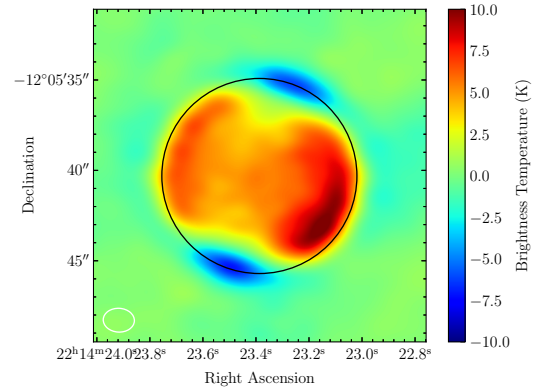
(b) Mar. 13th, 2016 at 99 GHz
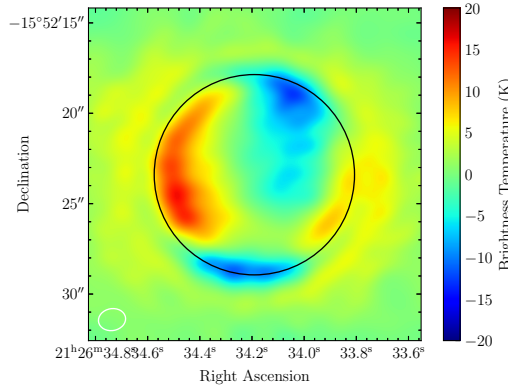
(c) Mar. 3rd, 2016 at 131 GHz
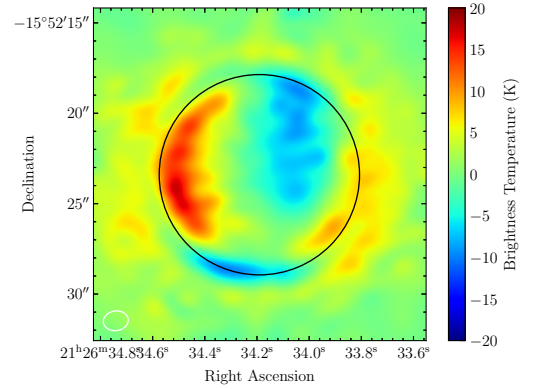
(d) Mar. 3rd, 2016 at 145 GHz
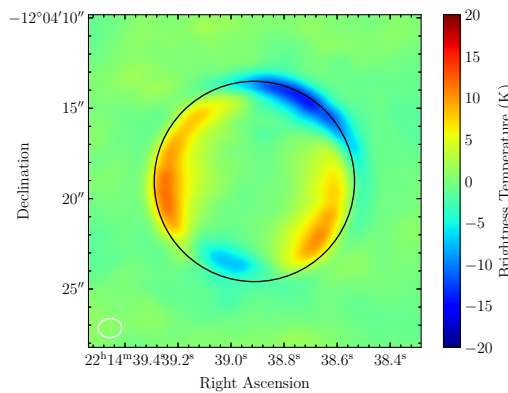
(e) Mar. 13th, 2016 at 131 GHz
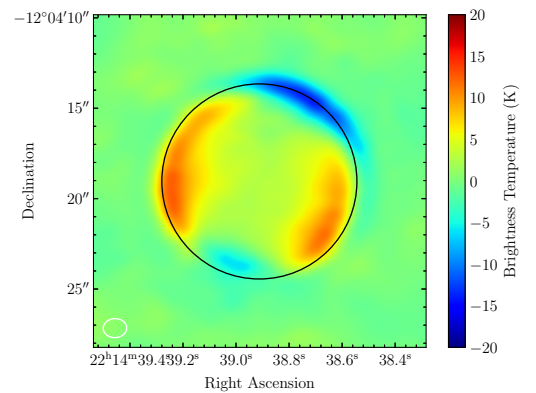
(f) Mar. 13th, 2016 at 145 GHz

Figure 5.18: Residual brightness temperature maps for the dedicated ALMA observations
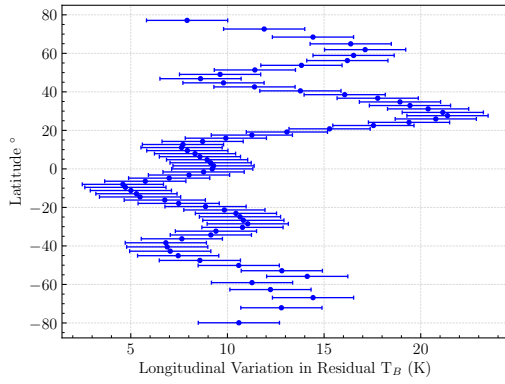
(a) Oct. 19th, 2013 at 100.5 GHz
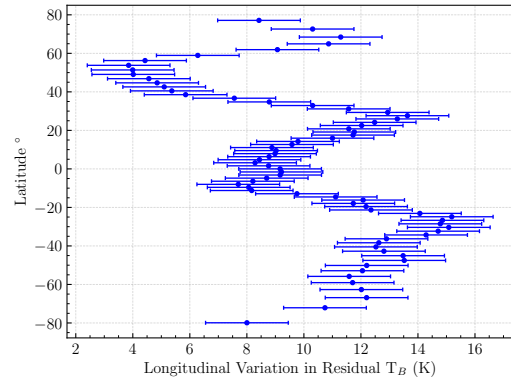
(b) Oct. 19th, 2013 at 113.5 GHz
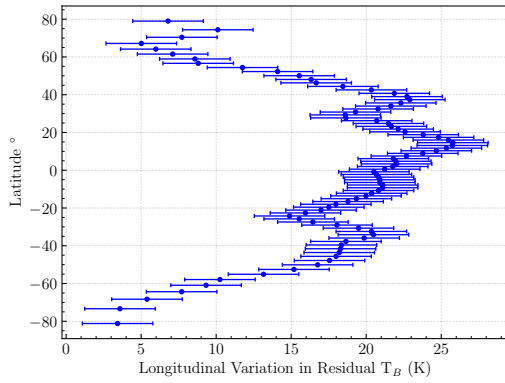
(c) Oct. 31st, 2013 100.5 GHz
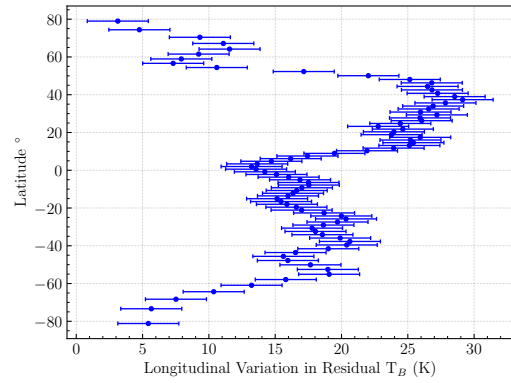
(d) Oct. 31st, 2013 113.5 GHz
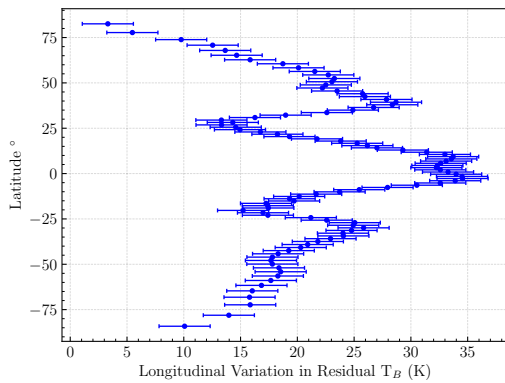
(e) Nov 12th, 2013 100.5 GHz
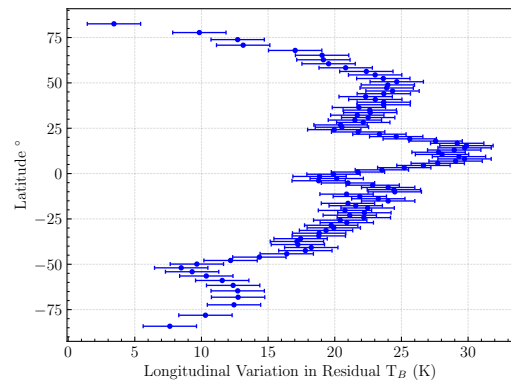
(f) Nov 12th, 2013 113.5 GHz

Figure 5.19: Longitudinal variations in brightness derived from the CARMA images.

For the October 19, 2013 CARMA observations, an average longitudinal variation of only 10-15 K is obtained, which is lower than the observations of de Pater by a factor of 2 and lower than the observations of Sagawa by a factor of 5 [26, 27]. Longitudinal variations on this order of magnitude are easily explained by more subtle variations in atmospheric composition and thermal structure. Given the higher sensitivity of ALMA as evidenced from the dayside images, spatially resolved observations of the Venus nightside would likely be capable of revealing the true millimeter-wavelength brightness structure of the planet.

5.6 Disk-averaged Emission Spectrum

Following the method of Butler et al. [22], the primary beam-corrected disk-averaged brightness temperature for the CARMA observations is determined from the derived V_o parameter from Equation 5.10 of the best-fit limb darkened disk model for the visibilities. The ALMA data is not investigated due to the inability to determine an accurate flux reference. The results for the CARMA data are shown in Figure 5.20 with the disk-averaged emission spectrum predicted by the radiative transfer model. The model assumes a uniform SO_2 abundance of 50 ppm below the cloud deck and the H_2SO_4 abundance profile derived from the Magellan orbit 3212 radio occultation experiment. The effect of varying the SO_2 abundance results in a near vertical translation of the brightness temperature as a function of frequency. The observed disk-averaged brightness temperature agrees well with the model predictions, with the exception of the higher channels of the upper sideband. This can be attributed to contamination by the J $1 \rightarrow 0$ CO line.
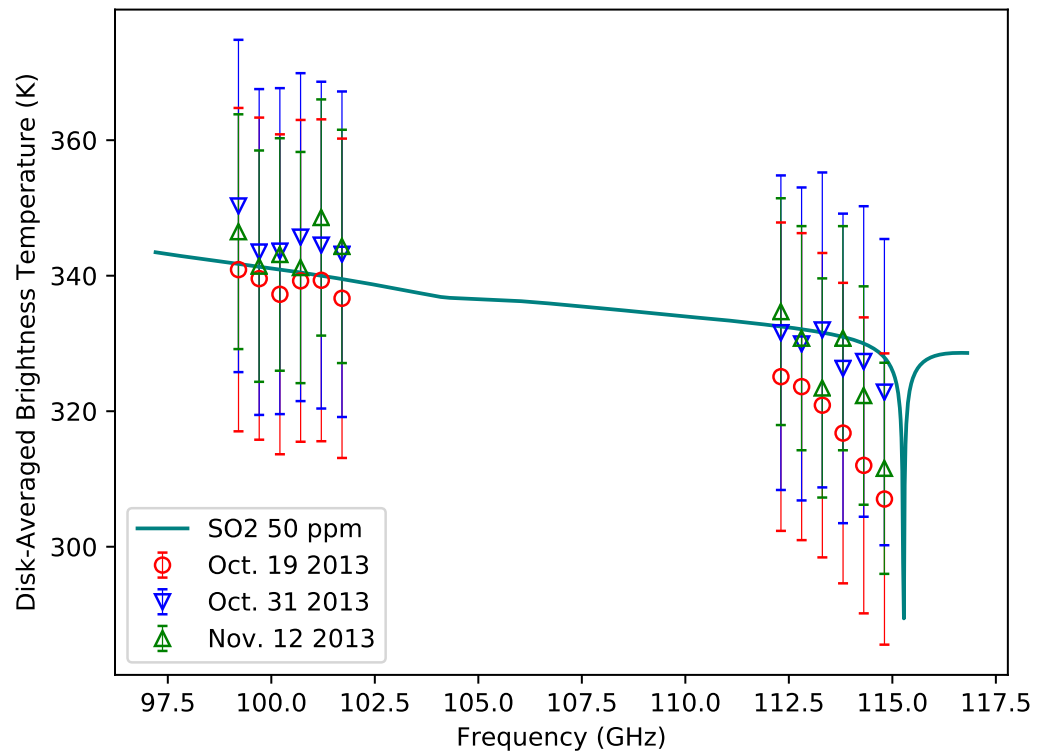
Figure 5.20: Disk-averaged brightness temperatures for the CARMA observations compared to radiative transfer model predictions.

CHAPTER 6

CONCLUSIONS

The objective of this research has been to further the understanding of the millimeter-wavelength spectrum of the Venus atmosphere. To this end, laboratory measurements of the CO_2-broadened opacity of H_2SO_4 vapor under simulated Venus conditions were conducted for uncharacterized portions of the H_2SO_4 spectrum. Semi-confocal open resonators were designed, fabricated, assembled, and operated within a pressure vessel and temperature chamber to conduct experiments with H_2SO_4 vapor broadened by up to 3 bars of CO_2 at temperatures from 540-575 Kelvins. The results of these laboratory experiments and previous microwave experiments made under similar conditions have been used to generate a model of H_2SO_4 vapor opacity valid from 1-150 GHz. This model has been incorporated into a microwave radiative transfer model which draws from laboratory measurements of other gases in the Venus atmosphere and prior knowledge from in situ and remote sensing of the Venus atmosphere and surface. This model has been used to predict the sensitivity of millimeter-wavelength emission from Venus to variations in the composition of the atmosphere. The radiative transfer model has also been used to predict the depth of penetration of a 32 GHz radio occultation signal and model the multi-wavelength emission of the Venus atmosphere. Finally, spatially resolved brightness temperature maps were developed from recent CARMA and ALMA observations. These results were compared to the radiative transfer model outputs and used to determine new upper bounds for the magnitude longitudinal brightness temperature variations across the Venus disk.

6.1 Contributions

In the process of conducting this dissertation research, several contributions were made to the field of microwave spectroscopy and planetary science.

6.1.1 Laboratory Measurements of H_2SO_4 Vapor

Semi-confocal microwave open resonators were designed to conduct measurements of H_2SO_4 vapor opacity at Venus conditions. The design of this resonator system, specifically the choice of corrosion-resistant materials (gold, stainless steel, and PTFE) and weldless design, was specific to the requirements imposed by the presence of hot H_2SO_4 vapor. While measurements of H_2SO_4 vapor absorption under similar conditions have been made at microwave frequencies, the measurements presented in this dissertation are the first broadband millimeter-wavelength laboratory measurements of H_2SO_4 vapor absorption covering the 2-4 millimeter and 7-10 millimeter bands. The results of these measurements revealed that prior models of H_2SO_4 vapor microwave opacity are not valid when extrapolated to higher frequencies. A novel method for calculating the relative partial pressures of H_2SO_4 evaporates within a pressure vessel following evaporation from a liquid solution with a known concentration was also developed.

6.1.2 Model for H_2SO_4 Vapor

To predict the opacity of H_2SO_4 vapor in the Venus atmosphere over the entire microwave spectrum, a model was developed utilizing all existing laboratory data of H_2SO_4 vapor opacity. This model is based on the JPL Spectral Line Catalog with the assumption of a Van Vleck-Weisskopf lineshape. Pressure-broadening linewidth parameters and temperature dependences were determined for all molecular components of the gas mixture (H_2SO_4 vapor, H_2O vapor, SO_3, and CO_2). To account for the significant opacity of H_2SO_4 vapor observed at frequencies lower than 40 GHz, the intensities of spectral lines associated with elastic collisions between H_2SO_4 molecules were scaled. The uncertainties in this model were quantified through assessment of thousands of free parameter combinations which achieved a fit to the data within 10% of the best fit value. Single frequency models of H_2SO_4 vapor opacity have also developed which are relevant for future Venus radio occultation experiments as proposed for several missions under active consideration.

6.1.3 Radiative Transfer Model and Venus Observations

Using the new model for millimeter-wavelength opacity of H_2SO_4 vapor, a radiative transfer model of the Venus atmosphere was developed capable of ray-tracing through the refractive CO_2 atmosphere. This model includes a more complete atmospheric inventory and more accurate opacity models than prior models used for continuum microwave studies of the Venus atmosphere, including both continuum absorbers (CO_2, SO_2, H_2SO_4), absorbers with narrow spectral features (H_2O, OCS, CO), and a full surface model. This model has been used to determine an estimated penetration depth near 47 kilometers above the mean surface for a radio occultation signal at 32 GHz transmitted from a Magellan-like spacecraft to the DSN antennas on Earth. Observations of Venus at 2-3 millimeters using the CARMA and ALMA radio telescopes were used to develop images of Venus with 0.3 - 3K noise levels, lower than any prior continuum observations made in this wavelength regime. These images were used to determine that prior observations of significant spatial brightness temperature variations across the Venus disk are likely the result of observing noise, and that the true variation is less than or equal to 10 - 15 Kelvins. This variation is within the predicted variations of Venus tropospheric thermal structure at the cloud base.

6.2 Future Work

6.2.1 Study of the H_2SO_4 Spectrum

The laboratory results presented in this dissertation raise a number of questions regarding the H_2SO_4 vapor rotational spectrum. From comparison of prior microwave studies and the new K_a band laboratory measurements with the unrevised JPL spectral line catalog, it is clear that ab initio calculations of the elastic collisional spectra of H_2SO_4 are unable to accurately predict the microwave opacity. The same has been found for the microwave spectrum of PH_3 [77]. Further attention should be dedicated to this discrepancy from a theoretical perspective. Additional laboratory measurements of the 20-30 GHz portion of the

H_2SO_4 pressure-broadened spectrum would also be useful to improve the accuracy of the broadband model. Also worthy of attention is the significant self-broadening of the H_2SO_4 system. While the relative concentrations of the evaporates (H_2SO_4, SO_3, H_2O) were calculated from theory, measurements of the true gas composition within the pressure vessel via mass spectrometry or complementary infrared spectroscopy would significantly improve the accuracy of the determined pressure-broadening coefficients. The laboratory measurements described in this dissertation were performed near 550 K, and future measurements of H_2SO_4 vapor opacity at lower temperatures using ultra-sensitive measurement systems would better constrain the temperature dependence of the opacity. Future measurements of H_2SO_4 vapor microwave and millimeter-wavelength opacity would ideally be performed using a glass or stainless steel pressure chamber with a large volume and a liquid H_2SO_4 reservoir with a large surface area. Such a configuration would enable significant amounts of H_2SO_4 vapor to boil into the chamber, and a lower surface area to volume ratio within the pressure would mitigate the impact any possible corrosion during an experiment.

6.2.2   Microwave Remote Sensing of Venus

As the results of this dissertation demonstrate, the ALMA radio telescope is sufficiently sensitive to measure the true emission structure of the Venus atmosphere at millimeter-wavelengths. Future observations of the Venus nightside and terminator with ALMA can be used to determine the true diurnal variation in brightness temperature at the lower cloud level. Coordinated observations with the VLA and ALMA, as well as any on orbit microwave/millimeter-wave radiometer, would be able to probe the atmosphere of Venus from the surface to clouds, enabling accurate retrieval of atmospheric structure and composition. The observational wavelengths can be selected to discriminate between atmospheric species, monitoring regions of enhanced and reduced opacity due to H_2SO_4 vapor and SO_2 to reduce the degeneracy of the inverse problem. Further interpretation of ALMA data will also require the correction of the current flux calibration issues experienced by the

observatory for solar system observations.

6.3   List of Publications

Journal Articles

- **Alex B. Akins** and Paul G. Steffes (2020), "Measurements of the K_a Band Opacity of Sulfuric Acid Vapor with Application towards Radio Occultations of Venus," *Icarus*, in preparation.

- **Alex B. Akins**, Paul G. Steffes (2019), "The Millimeter-Wavelength Absorption of Sulfuric Acid Vapor Measured Under Simulated Venus Conditions," *Icarus* 326, pp. 18-28

- Joshua Mendez-Harper, Paul Steffes, Joseph Dufek, **Alex Akins** (2019), "The Effect of Electrostatic Charge on the Propagation of GPS (L-Band) Signals Through Volcanic Plumes," *Journal of Geophysical Research: Atmospheres* 124, no. 4, pp. 1-16

Conference Proceedings

- Paul G. Steffes, **Alex B. Akins**, "The Potential for K_a Band Radio Occultation Measurements in the Study of the Venus Atmosphere," Abstract P34A-03, presented at the AGU Fall Meeting 2019, December 11, 2019, San Francisco, CA

- **Alex B. Akins** and Paul G. Steffes, "Progress on Laboratory Studies of Sulfuric Acid Vapor Opacity withApplication to K_a Band Radio Occultations of Venus," Lunar and Planetary Institute Contributions No. 2193, presented at the 17th VEXAG Meeting, November 6, 2019, Boulder, CO.

- **Alex Akins**, Kiruthika Devaraj, Statia Luszcz-Cook, Imke de Pater, Paul Steffes, "CARMA Observations of Venus: 3-millimeter Images of Lower Cloud Continuum

Emission," *EPSC Abstracts* 13, EPSC-DPS2019-95-1, 2019, presented at the EPSC-DPS Joint Meeting, September 19, 2019, Geneva, Switzerland.

- **Alex B. Akins** and Paul G. Steffes, "K_a Band Opacity of Sulfuric Acid Vapor at Venus: Initial Results," Abstract P49, presented at the International Venus Conference, June 1, 2019, Niseko, Hokkaido, Japan.

- **Alex B. Akins** and Paul G. Steffes, "Millimeter-Wavelength Remote Sensing of the Tropospheric Structure of Venus: Exploratory Simulations," Lunar and Planetary Institute *Contributions* No. 2137, presented at VEXAG 2018, November 7, 2018, Laurel, MD.

- **Alex B. Akins** and Paul G. Steffes, "Reconciling Models for the Centimeter-Wavelength and Millimeter-Wavelength Sulfuric Acid Vapor Absorption for Future Radio Sounding at Venus," *Bulletin of the American Astronomical Society* 50, no. 5, 2018. presented at the 50th Annual Meeting of the Division for Planetary Sciences of the American Astronomical Society, Knoxville, TN, October 22, 2018.

- **Alex Akins** and Paul Steffes, "Sulfuric Acid Vapor Absorption at Millimeter Wavelengths: Implications for Venus Observations," *42nd COSPAR Scientific Assembly Abstracts*, C3.1-0029-18 (FS-202), p. 906, presented at the 42nd Assembly of the Committee on Space Research (COSPAR) July 20, 2018, Pasadena, CA.

- **Alex B. Akins** and Paul G. Steffes, "Millimeter Wavelength Opacity of H_2SO_4 Vapor at Venus: Initial Results," *Lunar and Planetary Institute Contributions*, No. 2083, p. 2306, presented at the 49th Annual Meeting of the Lunar and Planetary Science Conference, The Woodlands, TX, March 21, 2018.

- **Alex B. Akins** and Paul G. Steffes, "Laboratory Measurements of Sulfuric Acid Vapor at Millimeter-Wavelengths under Venus Conditions," *Bulletin of the American Astronomical Society* 49, no. 5, 2017, p. 139, presented at the 49th Annual Meeting

of the Division for Planetary Sciences of the American Astronomical Society, Provo, UT, October 19, 2017.

- **Alex B. Akins**, Amadeo Bellotti, and Paul G. Steffes. "Simulation of the Atmospheric Microwave and Millimeter Wave Emission from Venus Using a Radiative Transfer Model Based on Laboratory Measurements", *Lunar and Planetary Institute Contributions*, No. 2022, 2017, presented at the Venus Modeling Workshop, Cleveland, OH, May 11, 2017.

Appendices

APPENDIX A

DETERMINING EXPERIMENTAL SULFURIC ACID PARTIAL PRESSURE

AND REFRACTIVITY

A.1   Partial Pressure of Sulfuric Acid Vapor

The biggest challenge associated with measuring the H_2SO_4 vapor absorption spectrum is the estimation of the amount of H_2SO_4 vapor in the measurement chamber. Kolodner developed an expression for the vapor pressure of H_2SO_4 vapor based on vapor pressure measurements from 338 to 623 Kelvins, which is given in Equation A.1 [112]. T is the temperature of interest, R is the ideal gas constant, T_o is the reference temperature of 375 K, T_c is the critical temperature of 910.5 K for H_2SO_4, and ΔF is the difference in chemical potential energies between pure H_2SO_4 and a given solution concentration.

$$ln(p)\text{(atm)} = 10156 \left[-\frac{1}{T} + \frac{0.38}{T_c - T_o} \left(1 + ln\left(\frac{T_o}{T}\right) - \frac{T_o}{T} \right) \right] - \frac{\Delta F}{RT} + 16.259 \quad \text{(A.1)}$$

During the absorption measurements, however, the vapor pressure of H_2SO_4 does not reach this theoretical value due to the surface tension of the liquid solution. As the surface area of the liquid-vapor interface increases, the amount of vaporized H_2SO_4 will approach this theoretical vapor pressure. This leaves two options for estimating the amount of H_2SO_4 vapor present in the pressure vessel. The first option is direct pressure measurement using a buffer gas to prevent gauge exposure to H_2SO_4 and prevent condensation. The second, and the one employed in this work, is the measurement of the change in volume of H_2SO_4 solution within the flask after an absorption measurement to estimate the vapor pressure of H_2SO_4. This method relies on the assumption that no H_2SO_4 exits vapor phase once the flask has been exposed to the pressure vessel and sulfuric acid has boiled off. While near-

adiabatic addition of carbon dioxide gas and care when handling valves and the oven door can minimize this risk, the chance remains that some sulfuric acid may either condense as a result of temperature fluctuations or exit vapor phase through reaction with trace materials within the pressure vessel. Despite these uncertanties, measurement of the solution volume before and after measurement remains the best way to estimate the vapor pressure of H_2SO_4 during the experiment. This was the method used by Kolodner and Steffes previously for their centimeter wavelength measurements [41].

During an experiment, a reservoir of liquid H_2SO_4 with a concentration of 98.07 % by weight is connected via piping and a cutoff valve to the pressure vessel. This reservoir flask is brought to temperature isolated from the pressure vessel, and the valve is then opened, allowing the solution to boil into the vessel. Water preferentially boils off to bring the solution to the azeotropic concentration of 98.87%, and the azeotropic solution continues to boil until the force of the solution surface tension balances the force associated with the pressure gradient. Furthermore, the vaporized sulfuric acid partially dissociates into water and sulfur trioxide. Kolodner estimated the mixing ratios of sulfuric acid, sulfur trioxide, and water using the following equations [112]. All n terms represent the number of moles of the subscripted components, n_{vap} is the number of moles of solution vaporized (determined through measurement of the initial and final solution volumes), and D is the dissociation constant, which is derived from reference tables of mixture component vapor pressures for the relevant initial solution concentration, temperature, pressure conditions [123].

$$n_{H_2SO_4} = n_{vap}(1 - D) \tag{A.2}$$

$$n_{SO_3} = (n_{vap} - n_{H_2SO_4}) = n_{vap}D \tag{A.3}$$

$$n_{H_2O} = n_{SO_3} + n_{freeH_2O} \tag{A.4}$$

$$D = \frac{p_{SO_3}}{P_{H_2SO_4} + P_{SO_3}} \tag{A.5}$$

However, the dissociation constant calculated from the vapor pressure data assumes constant solution concentrations. This is not necessarily the case for the sulfuric acid experiments, as water vapor selectively boils off until the solution reaches the azeotropic concentration. Therefore, a different set of governing expressions must be used to derive the constituent mixing ratios within the pressure vessel during the experiment.

In addition to the dissociation constant D defined in Equation A.5, the dissociation of sulfuric acid vapor can also be described through an equilibrium coefficient of dissociation K_p.

$$K_p = \frac{p_{SO_3}p_{H_2O}}{p_{H_2SO_4}} \tag{A.6}$$

Gmitro and Vermeulen give a best fit expression for K_p as a state function of temperature based on high temperature laboratory data, and they used this value to calculate the partial pressure of SO$_3$ along with theoretical partial pressures of H$_2$SO$_4$ and H$_2$O. [124]. However, the vapor liquid equilibrium calculations presented in this work were subsequently challenged, leading Vermeulen to revise and republish partial pressure estimates [123]. Que et al. correlated available thermodynamic data on the sulfuric acid vapor system concluded that this revised dataset was the most consistent with other measurements of H$_2$SO$_4$ thermodynamic properties, including measurement of the azeotrope concentration [125]. The expression for K_p given by Gmitro and Vermeulen was slightly modified for the results published by Vermeulen et al. The revised expression, which gives K_p in units of atmospheres, is calculated by fitting the coefficients in the original Gmitro and Vermeulen expression do the vapor pressure data of Vermeulen et al., and the correct expression is

given below.

$$ln\left(K_p\right) = Jln\left(\frac{298}{T}\right) + \frac{K}{T^2} + \frac{L}{T} + M + NT + QT^2 \tag{A.7}$$

Table A.1: Coefficients for Equation A.7

Coefficient	Value
J	-6.81115
K	-8.13684×10^{-4}
L	-9328.93
M	14.81661
N	-9.6802×10^{-3}
Q	2.23122×10^{-6}

The partial pressure of water can be written as the sum of the partial pressure of sulfur trioxide plus the partial pressure of free water that vaporizes both to form the azeotrope and as a component of the solution.

$$p_{H_2O} = p_{H_2O}^d + p_{H_2O}^{free} \tag{A.8}$$

$$p_{H_2O}^d = p_{SO3} \tag{A.9}$$

The measured volume of the vaporized solution can be converted to a mass and equated to the partial pressure of the evaporates. A is the azeotrope percentage, M_{total} is the mass of the vaporized azeotropic solution, V is the pressure vessel volume of 3.098 L, R is the ideal gas constant, and the subscripted m and p give the molar mass and partial pressure of the components.

$$AM_{total} = \frac{V}{RT}\left(m_{H_2SO_4}p_{H_2SO_4} + m_{SO_3}p_{SO_3} + m_{H_2O}p_{H_2O}^d\right) \tag{A.10}$$

Combining Equations A.7 and A.10 with the water and sulfur trioxide partial pressure

expressions, an equivalency can be stated based on the partial pressure of sulfuric acid.

$$p_{H_2SO_4} = \frac{1}{m_{H_2SO_4}} \left(\frac{RTAM_{total}}{V} - p_{SO_3} \left(m_{SO_3} + m_{H_2O} \right) \right) = \frac{p_{SO_3}^2 + p_{H_2O}^{free} p_{SO_3}}{K_p} \quad \text{(A.11)}$$

Equation A.11 can be re-arranged as a quadratic expression for the partial pressure of sulfur trioxide. The non-negative solution to this equation is taken as the sulfur trioxide partial pressure, and this value can be used with Equation A.7 to determine the partial pressures of sulfuric acid and water in the pressure vessel.

A.2   Refractivity of Sulfuric Acid Vapor

The refractivity of the sulfuric acid evaporates present in the pressure vessel can be determined from the shift in center frequency of the resonances after exposure to the vapor. To isolate the effects of sulfuric acid vapor, the effects of the other evaporates must be removed. The normalized microwave refractivity of sulfur trioxide was measured at room temperature by Steffes [126]. Significant variations between results were reported, and the maximum value of normalized refractivity was found to be $N'_{SO_3} = 1.156 \times 10^{-17} \frac{cm^3}{molec}$. This value is used for calculation of the millimeter-wavelength refractivity of sulfuric acid vapor for the sake of consistency with the microwave refractivity measurements made by Kolodner [112]. Since sulfur trioxide is a non-polar gas, it is reasonable to assume that it is sufficiently non-dispersive. This assumption is not necessarily true for water vapor. Rüeger gives an empirical expression for the microwave refractivity of Earth's atmosphere based on the contributions of dry air, carbon dioxide, and water vapor partial pressures. [127]. This expression represents a correction of data obtained from multiple GPS occultations. Equation **??** gives this refractivity including only terms that are associated with the partial pressure of water vapor in millibar. The coefficients of this equation are $K_2 = 71.97 \pm 10.5 \frac{K}{mbar}$

and $K_3 = 375406 \pm 3000 \frac{K^2}{mbar}$.

$$N_{H_2O} = K_2 \frac{p_{H_2O}}{T} + K_3 \frac{p_{H_2O}}{T^2} \tag{A.12}$$

This can also be expressed as a normalized refractivity where N_A is Avogadro's number and R is the ideal gas constant with units of $\frac{cm^3 mbar}{Kmol}$.

$$N'_{H_2O} = \frac{R}{N_A} \left(K_2 + \frac{K_3}{T} \right) \quad \frac{cm^3}{molec} \tag{A.13}$$

Although the coefficients in Equation A.12 rely on extrapolation of infrared spectral line measurements, the validity of this equation for millimeter wavelengths is uncertain. To confirm this, the millimeter-wavelength refractivity of water vapor was measured. This measurement was similar to the measurements of sulfuric acid vapor absorption outlined in Section 2.6 with notable exceptions. A small flask of sulfuric acid solution was connected via piping to the pressure vessel containing the semi-confocal open resonator, a vacuum was drawn, and the system was brought to a temperature of 185 ^{o}C. This temperature is high enough to allow excess water to boil off the sulfuric acid solution, but not high enough to vaporize a significant volume of the solution itself. The surface tension of the solution acts to limit the amount of water vapor that can escape, thereby avoiding the need for high pressure measurement equipment. Prior to exposure, the center frequency of three resonances was measured with the system under vacuum. The valve connecting the sulfuric acid solution to the pressure vessel was then opened, allowing water vapor to boil into the vessel. Since the water vapor is not corrosive, the pressure gauge system can be used to determine a water vapor pressure of 25.8 millibar. The decrease in resonance center frequency due to water vapor was then measured, and the experiment was terminated. The results of the experiment are summarized in Table A.2 and compared with the results predicted by Equation A.12

Based on the results of these measurements, equation A.12 can be assumed to be valid

Table A.2: Results of H$_2$O vapor millimeter-wavelength refractivity measurements

f_{vacuum} (GHz)	Measured Shift (MHz)	Predicted Shift (MHz)
79.3188	3.20	3.96
90.6196	3.84	4.52
109.8306	6.00	5.49

for the purpose of calculating the sulfuric acid vapor refractivity.

With this information and estimates of the partial pressure of the solution evaporates, the refractivity of sulfuric acid vapor can be calculated by rearranging Equation A.14.

$$N_{measured} = \frac{N_A}{RT} \left(N'_{H_2SO_4} p_{H_2SO_4} + N'_{SO_3} p_{SO_3} + N'_{H_2O} p_{H_2O} \right) \tag{A.14}$$

REFERENCES

[1] D. M. Hunten, L. Colin, T. M. Donahue, and V. I. Moroz, Eds., *Venus*. Tuscon, AZ: The University of Arizona Press, 1983.

[2] G. H. Pettengill, P. G. Ford, and R. A. Simpson, "Electrical Properties of the Venus Surface from Bistatic Radar Observations," *Science*, vol. 272, pp. 1628–1631, 1996.

[3] H. Svedhem, D. V. Titov, D. McCoy, J. P. Lebreton, S. Barabash, J. L. Bertaux, P. Drossart, V. Formisano, B. Häusler, O. Korablev, W. J. Markiewicz, D. Nevejans, M. Pätzold, G. Piccioni, T. L. Zhang, F. W. Taylor, E. Lellouch, D. Koschny, O. Witasse, H. Eggel, M. Warhaut, A. Accomazzo, J. Rodriguez-Canabal, J. Fabrega, T. Schirmann, A. Clochet, and M. Coradini, "Venus Express-The first European mission to Venus," *Planetary and Space Science*, vol. 55, no. 12, pp. 1636–1652, 2007.

[4] M. Nakamura, T. Imamura, M. Ueno, N. Iwagami, T. Satoh, S. Watanabe, M. Taguchi, Y. Takahashi, M. Suzuki, T. Abe, G. L. Hashimoto, T. Sakanoi, S. Okano, Y. Kasaba, J. Yoshida, M. Yamada, N. Ishii, T. Yamada, K. Uemizu, T. Fukuhara, and K. ichiro Oyama, "Planet-C: Venus Climate Orbiter mission of Japan," *Planetary and Space Science*, vol. 55, no. 12, pp. 1831–1842, 2007.

[5] "Visions and Voyages for Planetary Science in the Decade 2013-2022," Tech. Rep., 2011.

[6] Venus Exploration and Analysis Group (VEXAG), "Goals, Objectives, and Investigations for Venus Exploration," Tech. Rep. August, 2016, p. 15.

[7] V. A. Krasnopolsky, "Chemical kinetic model for the lower atmosphere of Venus," *Icarus*, vol. 191, no. 1, pp. 25–37, 2007.

[8] ——, "A photochemical model for the Venus atmosphere at 47-112km," *Icarus*, vol. 218, pp. 230–246, 2012.

[9] X. Zhang, M. C. Liang, F. P. Mills, D. A. Belyaev, and Y. L. Yung, "Sulfur chemistry in the middle atmosphere of Venus," *Icarus*, vol. 217, no. 2, pp. 714–739, 2012.

[10] C. J. Bierson and X Zhang, "Chemical cycling in the Venusian atmosphere : A full photochemical model from the surface to 110 km," *Journal of Geophysical Research: Planets*, 2020.

[11] R. D. Lorenz, D. Crisp, and L. Huber, "Venus atmospheric structure and dynamics from the VEGA lander and balloons: New results and PDS archive," *Icarus*, vol. 305, pp. 277–283, 2018.

[12] A. H. Barrett and D. H. Staelin, "Radio Observations of Venus and the Interpretations," *Space Science Reviews*, vol. 3, pp. 109–135, 1964.

[13] J. B. Pollack and C. Sagan, "An Analysis of the Mariner 2 Microwave Observations of Venus," *The Astrophysical Journal*, vol. 150, no. October, 1967.

[14] P. G. Steffes, J. M. Jenkins, R. S. Austin, S. W. Asmar, D. T. Lyons, E. H. Seale, and G. L. Tyler, "Radio Occultation Studies of the Venus Atmosphere with the Magellan Spacecraft 1. Experimental Description and Performance," *Icarus*, vol. 110, no. 1, pp. 71–78, 1994.

[15] P. G. Steffes and V. R. Eshleman, "Sulfuric acid vapor and other cloud-related gases in the Venus atmosphere: Abundances inferred from observed radio opacity," *Icarus*, vol. 51, no. 2, pp. 322–333, 1982.

[16] ——, "Sulfur dioxide and other cloud-related gases as the source of the microwave opacity of the middle atmosphere of Venus," *Icarus*, vol. 46, no. 1, pp. 127–131, 1981.

[17] P. G. Steffes, "Laboratory Measurements of the Microwave Opacity and Vapor Pressure of Sulfuric Acid Vapor under Simulated Conditions for the Middle Atmosphere of Venus," *Icarus*, vol. 64, pp. 576–585, 1985.

[18] J. M. Jenkins, P. G. Steffes, D. P. Hinson, J. D. Twicken, and G. L. Tyler, *Radio Occultation Studies of the Venus Atmosphere with the Magellan Spacecraft 2. Results from the October 1991 Experiments*, 1994.

[19] J. Oschlisniok, B. Häusler, S. Tellmann, and M. Bird, "Sulfuric acid vapor in the atmosphere of Venus as observed by the Venus Express Radio Science Experiment VERA," in *EPSC-DPS Joint Meeting 2019*, 2019.

[20] T. Imamura, M. Miyamoto, H. Ando, B. Häusler, M. Pätzold, S. Tellmann, T. Tsuda, Y. Aoyama, Y. Murata, H. Takeuchi, A. Yamazaki, T. Toda, and A. Tomiki, "Fine Vertical Structures at the Cloud Heights of Venus Revealed by Radio Holographic Analysis of Venus Express and Akatsuki Radio Occultation Data," *Journal of Geophysical Research: Planets*, vol. 123, no. 8, pp. 2151–2161, 2018.

[21] I. de Pater, "Radio Images of the Planets," *Annual Review of Astronomy and Astrophysics*, vol. 28, 1990.

[22] B. J. Butler, P. G. Steffes, S. H. Suleiman, M. A. Kolodner, and J. M. Jenkins, "Accurate and Consistent Microwave Observations of Venus and Their Implications," *Icarus*, vol. 154, pp. 226–238, 2001.

[23] J. M. Jenkins, M. A. Kolodner, B. J. Butler, S. H. Suleiman, and P. G. Steffes, "Microwave Remote Sensing of the Temperature and Distribution of Sulfur Compounds in the Lower Atmosphere of Venus," *Icarus*, vol. 158, no. 2, pp. 312–328, 2002.

[24] N. Mohan, S. Roy, G. Swarup, D. Oberoi, N. M. Ramanujam, S. R. C., and A. Bhardwaj, "Radio observation of Venus at meter wavelengths using the GMRT," *Icarus*, vol. 297, pp. 119–125, 2017. arXiv: 1709.09390.

[25] N. Mohan, S. R. Chellappan Pillai, G. Swarup, and D. Oberoi, "Polarization and brightness temperature observations of Venus with the GMRT," *Monthly Notices of the Royal Astronomical Society*, vol. 487, no. 4, pp. 4819–4826, 2019. arXiv: 1906.03243.

[26] I. de Pater, F. P. Schloerb, and A. Rudolph, "Venus Imaged with the Hat Creek Interferometer in the J = 1-0 CO Line," *Icarus*, vol. 90, pp. 282–298, 1991.

[27] H. Sagawa, "Terahertz remote-sensing of the Venusian atmosphere: Observations using the Nobeyama Millimeter Array," *Journal of the National Institute of Information and Communications Technology*, vol. 55, no. 1, pp. 149–157, 2008.

[28] K. P. Shah, D. O. Muhleman, and G. L. Berge, "Measurement of Winds in Venus ' Upper Mesosphere Based on Doppler Shifts of the 2.6-mm 12CO Line," *Icarus*, vol. 93, pp. 96–121, 1991.

[29] T. Encrenaz, E. Lellouch, G. Paubert, and S. Gulkis, "First detection of HDO in the atmosphere of Venus at radio wavelengths: an estimate of the H20 vertical distribution," *Astronomy & Astrophysics*, vol. 246, pp. 63–66, 1991.

[30] B. J. Sandor and R. T. Clancy, "Water vapor variations in the Venus mesosphere from microwave spectra," *Icarus*, vol. 177, pp. 129–143, 2005.

[31] B. J. Sandor, R. T. Clancy, and G. Moriarty-Schieven, "Upper limits for H2SO4 in the mesosphere of Venus," *Icarus*, vol. 217, no. 2, pp. 839–844, 2012.

[32] A. Moullet, E. Lellouch, R. Moreno, M. Gurwell, and H. Sagawa, "Wind mapping in Venus' upper mesosphere with the IRAM-Plateau de Bure interferometer," *Astronomy & Astrophysics*, vol. 546, A102, 2012. arXiv: 1202.5279.

[33] R. T. Clancy, B. J. Sandor, and G. Moriarty-Schieven, "Circulation of the Venus upper mesosphere/lower thermosphere: Doppler wind measurements from 2001-

2009 inferior conjunction, sub-millimeter CO absorption line observations," *Icarus*, vol. 217, no. 2, pp. 794–812, 2012.

[34] T. Encrenaz, R. Moreno, A. Moullet, E. Lellouch, and T. Fouchet, "Submillimeter mapping of mesospheric minor species on Venus with ALMA," *Planetary and Space Science*, vol. 113-114, pp. 275–291, 2015.

[35] A. Piccialli, R Moreno, T Encrenaz, T Fouchet, E Lellouch, and T Widemann, "Mapping the thermal structure and minor species of Venus mesosphere with ALMA submillimeter observations," *Astronomy & Astrophysics*, vol. 53, 2017.

[36] W Ho, I. A. Kaufman, and P Thaddeus, "Laboratory measurement of microwave absorption in models of the atmosphere of Venus," *Journal of Geophysical Research*, vol. 71, no. 21, pp. 5091–5108, 1966.

[37] P. G. Steffes, P. Shahan, G. C. Barisich, and A. Bellotti, "Laboratory measurements of the 3.7-20cm wavelength opacity of sulfur dioxide and carbon dioxide under simulated conditions for the deep atmosphere of Venus," *Icarus*, vol. 245, pp. 153–161, 2015.

[38] P. G. Steffes and V. R. Eshleman, "Laboratory Measurements of the Microwave Opacity of Sulfur Dioxide and Other Cloud-Related Gases under Simulated Conditions for the Middle Atmosphere of Venus," *Icarus*, vol. 187, pp. 180–187, 1981.

[39] A. K. Fahd and P. G. Steffes, "Laboratory measurements of the microwave and millimeter-wave opacity of gaseous sulfur dioxide (SO2) under simulated conditions for the Venus atmosphere," *Icarus*, vol. 97, no. 2, pp. 200–210, 1992.

[40] S. H. Suleiman, M. A. Kolodner, and P. G. Steffes, "Laboratory measurement of the temperature dependence of the gaseous sulfur dioxide microwave absorption with application to the Venus Atmosphere," *Journal of Geophysical Research: Planets*, vol. 101, pp. 4623–4635, 1996.

[41] M. A. Kolodner and P. G. Steffes, "The Microwave Absorption and Abundance of Sulfuric Acid Vapor in the Venus Atmosphere Based on New Laboratory Measurements," *Icarus*, vol. 132, no. 1, pp. 151–169, 1998.

[42] A. K. Fahd and P. G. Steffes, "Laboratory Measurement of the Millimeter Wave Properties of Liquid Sulfuric Acid," *Journal of Geophysical Research: Planets*, vol. 96, no. E2, pp. 17 471–17 476, 1991.

[43] A. Bellotti and P. G. Steffes, "The millimeter-wavelength sulfur dioxide absorption spectra measured under simulated Venus conditions," *Icarus*, vol. 254, pp. 24–33, 2015.

[44] T. R. Hanley and P. G. Steffes, "Laboratory measurements of the microwave opacity of hydrochloric acid vapor in a carbon dioxide atmosphere," *Icarus*, vol. 177, no. 1, pp. 286–290, 2005.

[45] F. Ulaby, *Fundamentals of Applied Electromagnetics*, 1999th ed. Upper Saddle River: Prentice Hall, 1999.

[46] S. Ramo, J. R. Whinnery, and T. Van Duzer, *Fields and Waves in Communications Electronics*, Third. New York: John Wiley and Sons, 1994.

[47] G. L. Matthaei, L. Young, and E. Jones, *Microwave Filters, Impedance Matching Networks and Coupling Structures*. McGraw-Hill, 1980.

[48] E. P Valkenburg and V. E. Derr, "A High-Q Fabry-Perot Interferometer for Water Vapor Absorption Measurements in the 100 Gc/s to 300 Gc/s Frequency Range," *Proceedings of the*, vol. 5, no. 4, 1966.

[49] T. R. Spilker, "Laboratory Measurements of Microwave Absorptivity and Refractivity Spectra of Gas Mixtures Applicable to Giant Planet Atmospheres," PhD thesis, Stanford University, 1990, ISBN: 0612699625.

[50] W. Culshaw, "The Fabry-Perot Interferometer at Millimetre Wavelengths," *Proc. Phys. Soc. B*, vol. 66, 1953.

[51] A. G. Fox and T. Li, "Resonant Modes in a Maser Interferometer," *Bell System Technical Journal*, vol. 40, no. 2, pp. 453–488, 1961.

[52] R. N. Clarke and C. B. Rosenberg, "Fabry-Perot and open resonators at microwave and millimetre wave frequencies, 2-300 GHz," *Journal of Physics E: Scientific Instruments*, vol. 15, no. 1, pp. 9–24, 1982.

[53] K. Devaraj, "The Centimeter- and Millimeter-Wavelength Ammonia Absorption Spectra Under Jovian Conditions," PhD thesis, Georgia Institute of Technology, 2011.

[54] U. Mingelgrin, R. G. Gordon, L. Frenkel, and T. E. Sullivan, "Microwave Spectrum of Compressed O2-Foreign Gas Mixtures in the 48 81 GHz Region," *The Journal of Chemical Physics*, vol. 57, no. 7, p. 2923, 1972.

[55] J. Joiner, "Millimeter-wave Spectra of the Jovian Planets," PhD thesis, Georgia Institute of Technology, 1991.

[56] P. Mohammed, "Laboratory Measurements of the Millimeter Wavelength Opacity of Phosphine and Ammonia under Simulated Conditions for the Cassini-Saturn

Encounter," PhD thesis, Georgia Institute of Technology, 2005, pp. 1–34, ISBN: 0471981230.

[57] T. R. Hanley, "The Microwave Opacity of Ammonia and Water Vapor: Application to Remote Sensing of the Atmosphere of Jupiter," PhD thesis, Georgia Institute of Technology, 2008, pp. 1–4.

[58] G. D. Boyd and J. P. Gordon, "Confocal Multimode Resonator for Millimeter Through Optical Wavelength Masers," *The Bell Systehm Technical Journal*, pp. 489–508, 1961.

[59] J. Moran, "Coupling of power from a circular confocal laser with an output aperture," *IEEE Journal of Quantum Electronics*, vol. 6, no. 2, pp. 93–96, 1970.

[60] M. van Blaricum, "The Coupling of a Single-Ridge Waveguide to a Fabry-Perot Resonator," *IEEE Transactions on Microwave Theory and Techniques*, vol. 31, no. 10, pp. 1898–1905, 1975.

[61] S. J. Orfanidis, *Electromagnetic Waves and Antennas*. New Brunswick, NJ: Rutgers University.

[62] J. Hust and A. Lankford, *Update of thermal conductivity and electrical resistivity of electrolytic iron, tungsten and stainless steel*, September. 1984, p. 61.

[63] J. D. Gallego, I Malo, I López, and C. D. González, "Thermal Conductivity and Electrical Loss of Thin Wall Millimeter Wave Stainless Steel Waveguides," IT-CDT, Guadalajara, Tech. Rep., 2015.

[64] R. A. Matula, "Electrical Resistivity of Copper, Gold, Palladium, and Silver," *Journal of Physical and Chemical Reference Data*, vol. 8, no. 4, pp. 1147–1298, 1979.

[65] A. Yakubu, Z. Abbas, and M. Hashim, "Effect of material thickness on attenuation (dB) of PTFE using finite element method at X-band frequency," *Advances in Materials Science and Engineering*, vol. 2014, no. 2, pp. 10–15, 2014.

[66] P. W. Rosenkranz, "Water vapor microwave continuum absorption: A comparison of measurements and models," *Radio Science*, vol. 33, no. 4, pp. 919–928, 1998.

[67] H. Pickett, R. Poynter, E. A. Cohen, M. Delitsky, J. Pearson, and H. Müller, "Submillimeter, Millimeter, and microwave Spectral Line Catalog," *Journal of Quantitative Spectroscopy and Radiative Transfer*, vol. 60, no. 5, pp. 883–890, 1998.

[68] A Bauer, M Godon, M Kheddar, L. D. S. Hertzienne, J. M. Hartmann, and G. Vole, "Temperature and perturber dependences of water vapor line-broadening experi-

ments at 183 GHz; calculations below 1000 GHz," *Journal of Quantitative Spectroscopy and Radiative Transfer*, vol. 41, no. 1, pp. 49–54, 1989.

[69] A Bauer, M Godon, and J Carlier, "Absorption of a H2O-CO2 Mixture in the Atmospheric Window at 239 GHz; H2O-CO2 Linewidths and Continuum," *Journal of Molecular Spectroscopy*, vol. 176, pp. 45–57, 1996.

[70] D. R. DeBoer and P. G. Steffes, "Laboratory Measurements of the Microwave Properties of H2S under Simulated Jovian Conditions with an Application to Neptune," *Icarus*, vol. 109, pp. 352–366, 1994.

[71] C. H Townes and A. L. Schawlow, *Microwave Spectroscopy*. New York: McGraw-Hill, 1955.

[72] E. A. Cohen and B. J. Drouin, "Submillimeter wave spectrum of sulfuric acid, H2SO4," *Journal of Molecular Spectroscopy*, vol. 288, pp. 67–69, 2013.

[73] R. L. Kuczkowski, R. D. Suenram, and F. J. Lovas, "Microwave Spectrum, Structure, and Dipole Moment of Sulfuric Acid," *Journal of the American Chemical Society*, vol. 103, no. 10, pp. 2561–2566, 1981.

[74] G. Sedo, J. Schultz, and K. R. Leopold, "Electric dipole moment of sulfuric acid from Fourier transform microwave spectroscopy," *Journal of Molecular Spectroscopy*, vol. 251, no. 1-2, pp. 4–8, 2008.

[75] R. Byrd, P. Lu, J. Nocedal, and C. Zhu, "A Limited Memore Algorith for Bound Constrained Optimization," *SIAM Journal of Scientific Computing*, vol. 16, no. 5, pp. 1190–1208, 1995.

[76] S. A. Clough, Y. Beers, G. P. Klein, and L. S. Rothman, "Dipole moment of water from Stark measurements of H2O, HDO, and D2O," *The Journal of Chemical Physics*, vol. 2254, no. 1973, pp. 2254–2259, 1973.

[77] J. P. Hoffman, P. G. Steffes, and D. R. DeBoer, "Laboratory Measurements of the Microwave Opacity of Phosphine: Opacity Formalism and Application to the Atmospheres of the Outer Planets," *Icarus*, vol. 152, no. 1, pp. 172–184, 2001.

[78] R. Storn and K. Price, "Differential Evolution - A Simple and Efficient Heuristic for Global Optimization over Continuous Spaces," *Journal of Global Optimization*, vol. 11, pp. 341–359, 1997.

[79] R. A. Perley and B. J. Butler, "An accurate flux density scale from 1 to 50 GHz," *Astrophysical Journal, Supplement Series*, vol. 204, no. 2, pp. 1–56, 2013. arXiv: 1211.1300.

[80] B. L. Ulich, J. H. Davis, P. J. Rhodes, and J. M. Hollis, "Absolute brightness temperature measurements at 3.5-mm wavelength," *IEEE Transactions on Antennas and Propagation*, vol. 28, no. 3, pp. 367–377, 1980.

[81] G. L. Stephens, *Remote Sensing of the Lower Atmosphere: An Introduction*. Oxford, UK: Oxford University Press, 1994.

[82] J. P. Hoffman, "Microwave Opacity of Phosphine: Application to Remote Sensing of the Atmospheres of the Outer Planets," PhD thesis, Georgia Institute of Technology, 2001.

[83] D. Koks, *Explorations in Mathematical Physics*. 2006, ISBN: 9780387309439.

[84] A. Bellotti, "The Millimeter-Wavelength Sulfur Dioxide Absorption Spectra Measured Under Venus Conditions," PhD thesis, Georgia Institute of Technology, 2014, pp. 1–18.

[85] D. A. Thompson, T. J. Pepin, and F. W. Simon, "Ray Tracing in Refracting Spherically Symmetric Atmosphere.," *Journal of the Optical Society of America*, vol. 72, no. 11, pp. 1498–1501, 1982.

[86] A. Seiff, J. T. Schofield, J. Kliore, Arvydas, F. W. Taylor, and S. S. Limaye, "Models of the structure of the atmosphere of Venus from the surface to 100 kilometers altitude," *Advances in Space Research*, vol. 5, no. 11, pp. 3–58, 1985.

[87] R. G. Knollenberg and D. M. Hunten, "The microphysics of the clouds of Venus: Results of the Pioneer Venus Particle Size Spectrometer Experiment," *Journal of Geophysical Research*, vol. 85, no. A13, pp. 8039–8058, 1980.

[88] E. P. James, O. B. Toon, and G. Schubert, "A numerical microphysical model of the condensational Venus cloud," *Icarus*, vol. 129, no. 1, pp. 147–171, 1997.

[89] F. Ulaby and D. Long, *Microwave Radar and Radiometric Remote Sensing*, 1st ed. Ann Arbor, MI: The University of Michigan Press, 2014.

[90] E. Marcq, F. P. Mills, C. D. Parkinson, and A. C. Vandaele, "Composition and Chemistry of the Neutral Atmosphere of Venus," *Space Science Reviews*, vol. 214, no. 1, p. 10, 2018.

[91] J.-L. Bertaux, T Widemann, A Hauchecorne, V. I. Moroz, and A. P. Ekonomov, "VEGA 1 and VEGA 2 entry probes: An investigation of local UV absorption (220-400 nm) in the atmosphere of Venus (SO2, aerosols, cloud structure)," *Journal of Geophysical Research-Planets*, vol. 101, no. E5, pp. 12 709–12 745, 1996.

[92] S. Lebonnois and G. Schubert, "The deep atmosphere of Venus and the possible role of density-driven separation of CO2 and N2," *Nature Geoscience*, vol. 10, no. 7, pp. 473–477, 2017.

[93] P. Varanasi and G. Tejwani, "Half-width calculations for CO lines broadened by CO2," *Journal of Quantitative Spectroscopy and Radiative Transfer*, vol. 11, no. 3, pp. 255–261, 1971.

[94] N. Semmoud-Monnanteuil and J. M. Colmont, "Pressure broadening of millimeter lines of carbon monoxide," *Journal of Molecular Spectroscopy*, vol. 126, no. 1, pp. 210–219, 1987.

[95] J. M. Hartmann, L. Rosenmann, M. Y. Perrin, and J. Taine, "Accurate calculated tabulations of CO line broadening by H2O, N2, O2, and CO2 in the 2003000K temperature range," *Applied Optics*, vol. 27, no. 15, p. 3063, 1988.

[96] H. Feeny, H. Lackner, P. Moser, and W. V. Smith, "Pressure Broadening of Linear Molecules. I," *The Journal of Chemical Physics*, vol. 22, no. 1, pp. 79–83, 1954.

[97] L Essen and K. D. Froome, "The Refractive Indices and Dielectric Constants of Air and its Principal Constituents at 24,000 Mc/s," *Proceedings of the Physical Society. Section B*, vol. 64, no. 10, p. 862, 1951.

[98] B. J. Butler, P. G. Steffes, S. H. Suleiman, M. A. Kolodner, and J. M. Jenkins, "Accurate and Consistent Microwave Observations of Venus and Their Implications," *Icarus*, vol. 154, no. 2, pp. 226–238, 2001.

[99] G. H. Pettengill, P. G. Ford, W. T. K. Johnson, R. K. Raney, and L. A. Soderblom, "Magellan : Radar Performance and Data Products," *Science*, vol. 252, no. 5003, pp. 260–265, 1991.

[100] G. H. Pettengill, P. G. Ford, and R. J. Wilt, "Venus surface radiothermal emission as observed by Magellan," *Journal of Geophysical Research*, vol. 97, no. 1, p. 13 091, 1992.

[101] J. M. Jenkins and P. G. Steffes, "Results from for 13-cm Absorptivity and H2SO4 Abundance Profiles the Season 10 (1986) Pioneer Venus Orbiter Radio Occultation Experiment," *Icarus*, vol. 90, pp. 129–138, 1991.

[102] J. Oschlisniok, B. Häusler, M. Pätzold, G. L. Tyler, M. K. Bird, S. Tellmann, S. Remus, and T. Andert, "Microwave absorptivity by sulfuric acid in the Venus atmosphere: First results from the Venus Express Radio Science experiment VeRa," *Icarus*, vol. 221, no. 2, pp. 940–948, 2012.

[103] J. M. Jenkins, "Variations on the 13 cm Opacity below the Main Cloud Layer in the Atmosphere of Venus Inferred from Pioneer-Venus Radio Occultation Studies 1978-1987," PhD thesis, Georgia Institute of Technology, 1992.

[104] J. Oschlisniok, S. Tellmann, and M. Pätzold, "H2SO4(g) and SO2 in the atmosphere of Venus as observed by the Venus Epxress radio science experiment VeRa," *Icarus*,

[105] R. S. Saunders, G. H. Pettengill, R. E. Arvidson, W. L. Sjogren, W. T. Johnson, and L. Pieri, "The Magellan Venus Radar Mapping Mission," *Journal of Geophysical Research*, vol. 95, no. B6, pp. 8339–8355, 1990.

[106] C. Chang, "DSN Telecommunications Link Design Handbook," Tech. Rep., 2017.

[107] G. B. Taylor, C. L. Carilli, and R. A. Perley, *Synthesis Imaging in Radio Astronomy II*. Socorro, NM, 1999, vol. 180, p. 1, ISBN: 1-58381-005-6.

[108] E. Fomalont and R. A. Perley, "Calibration and Editing," in *Synthesis Imaging in Radio Astronomy II*, G. B. Taylor, C. L. Carilli, and R. A. Perley, Eds., Socorro, NM, 1999, ch. 5.

[109] T. Imamura, T. Higuchi, Y. Maejima, M. Takagi, N. Sugimoto, K. Ikeda, and H. Ando, "Inverse insolation dependence of Venus' cloud-level convection," *Icarus*, vol. 228, pp. 181–188, 2014.

[110] S. S. Limaye, S. Watanabe, A. Yamazaki, M. Yamada, T. Satoh, T. M. Sato, M. Nakamura, M. Taguchi, T. Fukuhara, T. Imamura, T. Kouyama, Y. J. Lee, T. Horinouchi, J. Peralta, N. Iwagami, G. L. Hashimoto, S. Takagi, S. Ohtsuki, S. ya Murakami, Y. Yamamoto, K. Ogohara, H. Ando, K.-i. Sugiyama, N. Ishii, T. Abe, C. Hirose, M. Suzuki, N. Hirata, E. F. Young, and A. C. Ocampo, "Venus looks different from day to night across wavelengths: morphology from Akatsuki multispectral images," *Earth, Planets and Space*, vol. 70, no. 1, 2018.

[111] S. S. Limaye, D. Grassi, A. Mahieux, A. Migliorini, S. Tellmann, and D. Titov, "Venus Atmospheric Thermal Structure and Radiative Balance," *Space Science Reviews*, vol. 214, no. 5, p. 102, 2018.

[112] M. A. Kolodner, "Microwave Remote Sensing of Sulfuric Acid Vapor in the Venus Atmopshere," PhD thesis, Georgia Institute of Technology, 1997.

[113] D. P. Woody, A. J. Beasley, A. D. Bolatto, J. E. Carlstrom, A. Harris, D. W. Hawkins, J. Lamb, L. Looney, G Lee, R. L. Plambeck, S. Scott, and M Wright, "CARMA: A New Heterogeneous Millimeter-wave Interferometer," *Proceedings of SPIE*, vol. 5498, 2004.

[114] R. L. Brown, W. Wild, and C. Cunningham, "ALMA - The Atacama large millimeter array," *Advances in Space Research*, vol. 34, no. 3, pp. 555–559, 2004.

[115] C. L. Carilli, J. E. Carlstrom, and M. A. Holdaway, "Millimeter Interferometry," in *Synthesis Imaging in Radio Astronomy II*, 1999, ch. 28.

[116] A. G. Ginsburg, J. Bally, A. Barnes, N. Bastian, C. Battersby, H. Beuther, C. Brogan, Y. Contreras, J. Corby, J. Darling, C. De-Pree, R. Galván-Madrid, G. Garay, J. Henshaw, T. Hunter, J. M. D. Kruijssen, S. Longmore, F. Meng, E. A. C. Mills, J. Ott, J. E. Pineda, Á. Sánchez-Monge, P. Schilke, A. Schmiedeke, D. Walker, and D. Wilner, "Distributed star formation throughout the Galactic Center cloud Sgr B2," *The Astrophysical Journal*, vol. 853, no. 2, p. 171, 2018. arXiv: 1801.04941.

[117] J. P. McMullin, B Waters, D Schiebel, W Young, and K Golap, "CASA Architecture and Applications," in *Astronomical Data Analysis Software and Systems XVI*, vol. 376, 2007, pp. 127–130.

[118] B. J. Butler, "Flux Density Models for Solar System Bodies in CASA," NRAO, Tech. Rep., 2012.

[119] E. Fomalont, R. Hills, and R. Lucas, "The Calibration of ALMA using Radio Sources," *The Messenger*, vol. 155, no. March, pp. 19–22, 2014.

[120] B. J. Butler and T. S. Bastian, "Solar System Objects," in *Synthesis Imaging in Radio Astronomy II*, 1999, ch. 31, pp. 625–656.

[121] D. S. Briggs, F. R. Schwab, and R. A. Sramek, "Imaging," in *Synthesis Imaging in Radio Astronomy II*, 1999, ch. 7.

[122] B. G. Clark, "An Efficient Implementation of the Algorithm "CLEAN"," *Astronomy & Astrophysics*, vol. 89, pp. 377–378, 1980.

[123] T. Vermeulen, "Tables from the 1982 Amer. Inst. of Chem. Eng. meeting in Anaheim, CA," in *Perry's Chemical Engineering Handbook*, R. H. Perry and D. W. Green, Eds., 6th ed., New York: McGraw-Hill, 1984, pp. 65–69.

[124] J. I. Gmitro and T. Vermeulen, "VaporLiquid Equilibria for Aqueous Sulfuric Acid," *AIChE Journal*, vol. 10, no. 5, pp. 740–746, 1964.

[125] H. Que, Y. Song, and C. C. Chen, "Thermodynamic modeling of the sulfuric acid-water-sulfur trioxide system with the symmetric electrolyte NRTL model," *Journal of Chemical and Engineering Data*, vol. 56, no. 4, pp. 963–977, 2011.

[126] P. G. Steffes, "Abundances of Cloud-Related Gases in the Venus Atmosphere as Inferred from Radio Opacity," PhD thesis, Stanford University, 1982.

[127] J. Rüeger, "Refractive index formulae for radio waves," *FIG XXII International Congress*, pp. 1–13, 2002.

VITA

Alex Akins was born in Atlanta, Georgia in 1994, and received his Bachelors, Masters, and Ph.D. degrees in Electrical and Computer Engineering from the Georgia Institute of Technology. In high school, he worked with Dr. Barbara Boyan's Bone and Cartilage Laboratory at Georgia Tech to study the conditioning of adipose stem cells with Vitamin D metabolites. As an undergraduate, Alex worked with teams in the Butera Lab to design compact devices for electrophysiology and gait monitoring, and he also worked as the telecommunications subsystem lead for the RECONSO CubeSat project in the Georgia Tech Aerospace Systems Design Laboratory. During his undergraduate study, he worked with the Intelligence and Space Research group at Los Alamos National Laboratory on inter-subsystem communications protocols for the Prometheus CubeSat constellation. He also worked with medical device startup NFANT Labs in researching methods for accelerometer signal feature detection for the NFANT Feeding Solution product.

As a Ph.D. student in the Planetary Atmospheres Group at Georgia Tech, he has primarily studied microwave propagation in the atmosphere of Venus. His dissertation work focuses on laboratory characterization of the opacity of sulfuric acid vapor at millimeter-wavelengths and on interpretation of millimeter-wavelength observations of Venus made using ground-based radio telescopes. Following the completion of his doctorate, he will join the Microwave Instrument Science Group at NASA Jet Propulsion Laboratory in California.